Dipl. Ing. Daniel Bauernfeind, BSc

Fork Tensor Product States: Efficient Multi-Orbital Impurity Solver for Dynamical Mean Field Theory

DOCTORAL THESIS

to achieve the university degree of

Doktorin der technischen Wissenschaften

submitted to

Graz University of Technology

Supervisor

Ao.Univ.-Prof. Dipl.-Phys. Dr.rer.nat. Hans Gerd Evertz

Institute of Theoretical and Computational Physics

Graz, February 2018

AFFIDAVIT

I declare that I have authored this thesis independently, that I have not used other than the declared sources/resources, and that I have explicitly indicated all material which has been quoted either literally or by content from the sources used. The text document uploaded to TUGRAZonline is identical to the present doctoral thesis.

Date

Signature

Abstract

In the present thesis we introduce a new approach to solve impurity models for Dynamical Mean Field Theory (DMFT) working directly on the real frequency axis - Fork Tensor Product States (FTPS). FTPS is a tensor network with a fork-like graph, that is especially suited for multi-orbital Anderson Impurity Models (AIM). The main idea of this approach, the decoupling of the bath degrees of freedom, that allows to employ a large number of bath sites and therefore to describe the bath hybridization with high precision. This enables us to resolve high energy features in the impurity spectral function that often turn out to be atomic multiplets. We not only show that within DMFT such multiplets exist, but also demonstrate why the state of the art method, Continuous Time Quantum Monte Carlo (CTQMC), fails to resolve them. To obtain real-frequency spectra, CTQMC relies on an ill-posed analytic continuation. Such methods are not able to reproduce high-energy multiplets, if the imaginary time Green's function is subject to statistical noise.

After a general introduction of AIMs, we show how to use them to represent the bath of free fermions obtained from the DMFT. We also mention the most important aspects of how to combine Density Functional Theory (DFT) with DMFT, among others, the choice of correlated subspace and the number of correlated orbitals.

The FTPS solver is based on the Density Matrix Renormalization Group (DMRG) with Matrix Product States (MPS). Therefore, we introduce MPS in some detail and discuss how to use MPS for the calculation of Green's functions. Since unitary transformations acting non-trivially only on the bath degrees of freedom do not change any observable of the impurity, several equivalent representations of the bath exist. In the present thesis we focus on the so called star geometry of the bath and show how to efficiently use it in MPS calculations, despite the long-range hopping terms of the star geometry.

One of the crucial properties of the FTPS tensor network is that its graph is loop-free. This allows us to find the Schmidt decomposition for each bond, which in turn means we can safely truncate the tensor network. We show

how to formulate DMRG (ground state search), as well as how to perform the time evolution with FTPS - the two necessary ingredients to calculate Green's functions.

Finally, we use FTPS as a DMFT impurity solver on the real frequency axis for two real-materials. First, for the benchmark compound $SrVO_3$, where we use a three-band model for the description of the correlated subspace of the t_{2g} bands. We find a distinct three-peak structure in the impurity spectral function and show that it is a direct result of the atomic multiplets of the interaction Hamiltonian employed. To validate our approach, we compare to CTQMC on the real-, as well as on the imaginary frequency axis. For the latter, we find very good agreement, while the differences on the real frequency axis can be attributed to the already mentioned analytic continuation.

The second compound is the strongly correlated insulator $SrMnO_3$. There, we focus on the influence of the choice of correlated subspace and number of orbitals on the impurity spectral function. In the simplest case, using a small energy window and only three correlated orbitals for the t_{2g} bands, we find a typical Mott insulator with a lower and an upper Hubbard band. But since the lower Hubbard band is close (in energy) to hybridizations of the oxygen p-bands with the t_{2g} -bands, the small energy window calculation is not fully justified. Including these hybridizations in a so called dp-model, we find that the lower Hubbard band splits into several peaks due to the additional hybridizations. In this model, the distinction between Mott- and charge transfer insulator is not clear anymore. Our results shed some light on this intermediate regime. At the same time, one can argue that also the e_g -bands are important for $SrMnO_3$, since they are located directly above the Fermi energy. In including them, we perform a DMFT calculation for the full Mn-3d shell, i.e. for a five orbital model, including hybridizations. The resulting spectral function of this calculation is in good agreement with Photo Emission Spectroscopy (PES) and X-ray Absorption Spectroscopy (XAS) experiments. Most importantly, the XAS measurement shows a three-peak structure of alternating e_g -t_{2g} -e_g character, a feature that our calculation shows as well. This emphasizes the importance of real-frequency solvers, since they allow us to resolve these kind of multiplets.

Kurzfassung

In dieser Arbeit wird ein neuer *Impurity Solver* [1] für *Dynamical Mean Field Theory* (DMFT), genannt *Fork Tensor Product States* (FTPS), vorgestellt. Mit diesem *Impurity Solver* ist es möglich die Spektralfunktion direkt auf der reellen Frequenzachse zu brechnen. Er eignet sich besonders für Mehr-Orbital Modelle, da der Graph dieses Tensor Netzwerk eine gabelartige Struktur aufweist. Die grundlegende Idee hinter FTPS ist es die Freiheitsgrade der Bäder verschiedener Orbitale zu trennen. Dies erlaubt es die Bad-Hybridisierung präzise darzustellen, da eine große Anzahl an Badplätzen benutzt werden kann. Damit können hochenergie Anregungen in der Spektralfunktion aufgelöst werden, bei denen es sich oftmals um atomare Multiplets handelt. Es wird nicht nur gezeigt, dass FTPS erlaubt solche atomaren Anregungen aufzulösen, sondern auch warum *Continuous Time Quantum Monte Carlo* (CTQMC) - der bisherige Stand der Technik - dazu nicht in der Lage ist. CTQMC benötigt nämlich eine analytische Fortsetzung, um die Spektralfunktion auf der reelen Frequenzachse zu berechnen. Da die analytische Fortsetzung ein sehr schlecht konditioniertes Problem darstellt, ist sie nicht in der Lage Multiplets aufzulösen, vor allem wenn die Greensche Funktion auf der imaginären Zeitachse verrauscht ist.

Nach einer kurzen Einführung in *Anderson Impurity* Modelle (AIM), wird gezeigt wie man sie in DMFT einsetzt um das Bad freier Fermionen zu beschreiben. Außerdem werden die wichtigsten Aspekte, wie man DMFT mit Dichtefunktionalstheorie (DFT) kombiniert, erwähnt. Darunter fallen unter anderem die Wahl des korrelierten Unterraumes, sowie die Anzahl der korrelierten Orbitale.

Da FTPS auf der Methode der *Density Matrix Renormalization Group* (DMRG) mit *Matrix Product States* (MPS) basiert, werden diese Konzepte im Detail diskutiert. Außerdem wird eine der Möglichkeiten vorgestellt mit der Greensche Funktionen mit MPS berechnet werden können. Dies er-

---

[1] Die Umgangssprache in der Physik ist Englisch. Deshalb hab Ich mich dazu entschlossen Eigennamen, deren Gebrauch in der deutschen Sprache unüblich sind auf Englisch zu schreiben und, um sie zu markieren, Kursiv zu stellen. Das selbe gilt für Eigennamen deren deutsche Form nicht mit der dafür benutzten Abkürzung übereinstimmt.

möglicht es *Impurity* Modelle zu lösen, worunter im Allgemeinen die Berechnung der Greenschen Funktion der *Impurity* gemeint ist. Da diese Größe (sowie jede andere Observable der *Impurity*) durch unitäre Transformation die nur auf das Bad wirken nicht verändert wird, gibt es eine Vielzahl von Möglichkeiten das Bad darzustellen. Diese Arbeit legt den Schwerpunkt auf die sogenannte Stern-Geometrie. Es wird gezeigt, dass, obwohl in Stern-Geometrie die Kopplungen langreichweitig sind, man sie effizient für MPS einsetzen kann.

Da der Graph eines FTPS Netzwerks schleifenfrei ist, kann für jeden Index des Tensornetzwerkes die Schmidt Zerlegung des quantenmechanischen Zustands gefunden werden. Dies erlaubt eine sichere Trunkierung des FTPS Tensor Netzwerks, sowie DMRG und Zeiteintwicklungsalgorithmen zu formulieren um Greensche Funktionen zu berechnen.

Im Folgenden wird FTPS als *Impurity Solver* für DMFT bei zwei verschieden Materialien eingesetzt. Zuerst für das Benchmark-Material $\mathrm{SrVO_3}$, indem die t_{2g} Bänder in einem drei-Orbital Modell behandelt werden. In diesem Modell weist das obere Hubbard Band drei markante Spitzen auf, bei denen es sich um atomare Anregungen des Wechselwirkungsoperators handelt. Ein Vergleich von FTPS mit CTQMC zeigt, dass beide Methoden zwar auf der imaginären Frequenzachse übereinstimmen, es jedoch für reele Frequenzen Unterschiede gibt. In der Spektralfunktion von CTQMC (nach analytischer Fortsetzung) sind solche Spitzen nicht auffindbar, was auf die analytische Fortsetzung zurückzuführen ist.

Danach wird FTPS für den stark korrelierten Isolator $\mathrm{SrMnO_3}$ eingesetzt. Dabei wird die Frage beantwortet, wie sich die Wahl des korrelierten Unterraums, sowie die Anzahl der korrelierten Orbitale auf das Spektrum auswirken. Zuerst wird der einfachste Fall betrachtet: ein kleines Energiefenster nur für die t_{2g} Bänder. Die daraus resultierende Spektralfunktion zeigt einen typischen Mott Isolator mit oberem und unterem Hubbard Band. Es stellt sich jedoch heraus, dass das untere Hubbard Band energetisch sehr nahe bei Hybridisierungen von Sauerstoff p-Bändern mit den t_{2g} Bändern liegt. Dies bedeutet, dass das kleine Energiefenster eigentlich nicht gerechtfertigt war, da es diese Hybridisierungen vernachlässigt. Eine Rechnung für ein größeres Energiefenster, ein sogenanntes *dp*-Modell zeigt, dass sich das untere Hubbard Band durch die Hybridisierungen aufspaltet und es daher keine klare Trennung zwischen Mott- und *charge transfer* Isolator mehr gibt. Diese Arbeit liefert wichtige Erkenntnisse über dieses Zwischenregime. Neben den Hybridisierungen, sind auch die e_g Bänder von Bedeutung, da sie direkt über der *Fermi*-Energie liegen und deshalb eine Rechnung für die gesamte Mn $3d$-Schale durchgeführt werden müsste. Die daraus resultierende Spektralfunktion stimmt gut mit Photo-Emissionsspektroskopie (PES) und Röntgen-Absorptionssepktroskopie (XAS) Experimenten überein. Vor allem das XAS Experiment zeigt drei Spitzen die abwechselnd von e_g , t_{2g} und e_g Orbitalen stammen. Eine solche Struktur ist auch in den FTPS Rechnungen vorhanden. Dies zeigt, dass *Impurity Solver*, die direkt reele Größen berechnen können, einen wichtigen Beitrag für das Verständnis von stark korrelierten Materialien liefern.

List of Publications

A list of publications of the author is given below. Publications relevant for the present thesis are marked with by an asterisk (*).

1. D. Bauernfeind, M. Zingl, R. Triebl, M. Aichhorn, and H. G. Evertz. Fork Tensor-Product States: Efficient Multiorbital Real-Time DMFT Solver. *Phys. Rev. X* 7, 031013 (2017) (*)

2. V. Eisler and D. Bauernfeind. Front dynamics and entanglement in the XXZ chain with a gradient. *Phys. Rev. B* 96, 174301 (2017)

3. M. Zingl, M. Nuss, D. Bauernfeind, and M. Aichhorn. A real-frequency solver for the Anderson impurity model based on bath optimization and cluster perturbation theory. *Physica B: Condensed Matter.* (2017) (*)

4. D. Bauernfeind, R. Triebl, M. Zingl, M. Aichhorn, and H. G. Evertz. Dynamical Mean-Field Theory on the Real-Frequency Axis: p-d Hybridizations and Atomic Physics in $SrMnO_3$. *ArXiv e-prints.* Submitted to PRB. arXiv:1712.08055 (2017) (*)

Acknowledgment

First, and foremost I would like to thank my supervisor Hans Gerd, who gave me the opportunity to work on this exciting topic for the last three years. I would like to thank you for your kind and continuous support which not only kept me on my path, but also gave me enough freedom to take some detours. I am especially grateful for your diligent support with the present thesis. Without your help with all the difficulties this thesis would not have been possible.

Kann I mal mit dir was philosophieren? was the start of more than a few discussions that most of the time ended definitely not where they started. For this amazing time I want to thank my two bureau colleges Florian and Matthias. It was great fun and I am grateful that we were able to explore together the mysteries that physics presented us on a daily basis.

One of the things I loved most about my time here, is the freedom to collaborate and work on new projects. So it came that suddenly I visited Manuel, Robert, Gernot nearly every day to talk about some problem with DMFT or other purely work related stuff (of course). This collaboration was imperative for *our* success - Thank You!

The collaboration would not have bee possible without Markus Aichhorn and I am very grateful for this. I would also like to thank you for patiently answering any question I had about DFT+DMFT.

I also want to thank all colleges from the institute (in alphabetical order): Enrico Arrigoni, Lilia Boeri, Gerhard Dorn, Viktor Eisler, Delia Fugger, Andreas Hirczy, Winfried Kernbichler, Wolfgang von der Linden, Michael Rumetshofer, Andriy Smolyanyuk, Max Sorantin and Irakli Titvinitze.

I would like to express my gratitude to Brigitte Schwarz, who patently reminded me of all the forms I filled out way too late and to Andreas Hirczy,

who diligently keep all our computers running.

My last, but most important thanks go to my family and especially to you Claudia. Your kindness and love is what gives meaning to these last three years.

Contents

1 Introduction

According to the Cambridge dictionary [5], interaction is defined as: “an occasion when two or more people or things communicate with or react to each other”. When such a reaction occurs, objects stop being independent of each other and their future becomes intertwined, leading to a plethora of exciting phenomena. As a physicist I would call this something along the lines of *a failure of the single-particle description.* Here and now, the objects/particles we consider are electrons, described within the framework of quantum mechanics and they interact with each other through the well known Coulomb repulsion.

In physics, the most interesting cases of interactions can be found when the energy due to the interactions, let us parametrize it with a single parameter U, is of a similar magnitude than the kinetic energy, parametrized by t. In these cases neither of them dominates and therefore perturbation theory fails. For example, in order to describe magnetic impurities in a metallic host, Anderson proposed his nowadays famous Anderson Impurity Model (AIM). The interactions in this model lead to an emergence of a new energy scale $\sim \frac{t^2}{U}$ [6, 7], describing spin-spin interactions and ultimately leading to the Kondo-effect [8]. For the present thesis, the importance of AIMs comes from its close connection to Dynamical Mean-Field Theory (DMFT). Originally developed for models with infinite connectivity [9, 10], DMFT can be considered an approximation for finite-dimensional systems, neglecting spatial correlations. In DMFT we focus on a single site of the model Hamiltonian, and map its original environment onto an effective model - usually an AIM. The most challenging part of a DMFT calculation is then the solution of the AIM thus obtained. DMFT is not only applicable to model Hamiltonians. On the contrary, the combination of DMFT with Density-Functional Theory (DFT) [11–13] soon became one of the most important methods for the *ab initio* description of strongly-correlated materials.

Therefore, an impurity solver (a method that calculates the impurity Green’s function of an AIM), is at the heart of our understanding of strongly-correlated materials with DMFT. For realistic scenarios, the state of the art impurity solvers are variants of Continuous Time Quantum Monte Carlo (CTQMC) [14, 15] (see Sec. 2.2 for methods other than CTQMC). CTQMC, while statistically exact on the imaginary frequency axis, relies on an ill-posed analytic continuation to obtain real-frequency properties. Furthermore, it is in some cases plagued by a Fermionic sign problem, disallowing CTQMC to reach low temperatures. Therefore, an impurity solver working directly on the real-frequency axis and, at the same time, being able to perform calculations for multiple orbitals (needed for the description of real-materials) is highly desirable.

The present thesis aims to close this gap. Based on the immense success of the Density Matrix Renormalization Group (DMRG) with Matrix Product States (MPS) [16, 17], we propose a tensor network especially suited for multi-orbital AIMs. The graph of this tensor network is a fork-like structure giving our approach its name: Fork Tensor Product States (FTPS). We show that it is a viable impurity solver for at least five orbitals on the real frequency axis. This allows us to obtain high-resolution results for the real-frequency spectrum and to resolve atomic multiplets within DMFT, also found in experiments.

This thesis is structured as follows. In Sec. 2, we introduce the Anderson Impurity Model (AIM). We start with a single orbital and then discuss the multi-orbital case. There, we especially focus on the Kanamori interaction that we use as interaction Hamiltonian throughout this thesis. Then, we briefly discuss existing impurity solvers, as well as their strengths and weaknesses. Sec. 3 is devoted to the Dynamical Mean-Field Theory (DMFT) and how to combine it with Density-Functional Theory (DFT) for an *ab initio* description of strongly-correlated materials. In Sec. 4, we introduce Matrix Product States (MPS) as well as the Density Matrix Renormalization Group (DMRG) and time evolution algorithms working with MPS. The application of MPS to the single-orbital AIM is discussed in Sec. 5, with a special focus on the star geometry representation of the bath. Then, we give a possible explanation why MPS perform poorly for multi-orbital models. To solve this issue, we introduce the FTPS tensor network in Sec. 6, where we show how to obtain Schmidt decompositions. This allows us to efficiently search for ground states with DMRG and perform the time evolution. In Sec. 7, we use the FTPS solver for DMFT calculations for the benchmark compound $SrVO_3$. The main text of this section was published in Ref. [1]. Finally, in Sec. 8 we present the paper published recently in Ref. [4], where we performed DMFT calculations for the strongly-correlated insulator $SrMnO_3$.

2 Anderson Impurity Models

In 1961 Anderson introduced the Anderson Impurity Model (AIM) [18] to describe magnetic impurities in a metallic host. In its simplest form, for a single orbital, the Hamiltonian in second quantization is given by:

$$H = \underbrace{\sum_{k\sigma} \epsilon_k n_{k\sigma}}_{H_{\text{bath}}} + \underbrace{\sum_{k\sigma} V_k \left(c^\dagger_{0\sigma} c_{k\sigma} + \text{h.c.} \right)}_{H_{\text{hyb}}} + \underbrace{\sum_{\sigma} \epsilon_0 n_{0\sigma} + U n_{0\uparrow} n_{0\downarrow}}_{H_{\text{loc}}} \tag{2.1}$$

$c^\dagger_{k\sigma}$ ($c_{k\sigma}$) creates (annihilates) an electron in a Bloch state labeled by momentum k and spin σ, while $n_{k\sigma} = c^\dagger_{k\sigma} c_{k\sigma}$ is the usual number operator. The impurity degrees of freedom are labeled by an index $k = 0$ for convenience. The first term, H_{bath} is the bath of free electrons of the metallic host, while H_{loc} describes the local degrees of freedom of the interacting impurity. The hybridization term H_{hyb} couples the metallic host to the impurity via a *hopping* from the impurity to one of the bath states with strength V_k. Although impurity models are of great importance in their own right, in the present thesis we will use them exclusively within the framework of Dynamical Mean-Field Theory (DMFT), introduced in the next section. In this section we discuss a few general properties of impurity models, as well as introduce the basic notation that will accompany us throughout this thesis.

Although the impurity in Eq. 2.1 consists only of a single orbital, this model can be used to understand the appearance or absence of a magnetic moment from d- or f-shell electrons of the impurity. In what is called the local moment regime, the ground state of H_{loc} is the doubly degenerate single-occupation. Employing a Schrieffer-Wolff transformation [6, 7] one can integrate out the charge fluctuations of the doubly occupied and empty impurity. In that case, that the low-energy description of the AIM in Eq. 2.1 is given by the Kondo or s-d model [7, 8], responsible for the low-energy Kondo-peak in the impurity spectral function. On the other hand, the high energy charge fluctuations of the AIM with an energy scale proportional to U are responsible for the Hubbard bands. Being able to describe these two energy scales, AIMs are an important tool in our understanding correlated materials.

In the following, we will mostly be interested in the retarded real-time Green's function of the impurity:

$$G(t) = -i\Theta(t)\langle\{c_{0\sigma}(t), c_{0\sigma}^{\dagger}\}\rangle \tag{2.2}$$

and its energy (frequency) representation,

$$G(\omega) = \int G(t)e^{i\omega t}dt. \tag{2.3}$$

In the following we will discuss the spin symmetric case, so we drop the spin index σ in the above definitions of the Green's functions. Solving an AIM means to calculate one of these Green's function, which is a highly non-trivial task in general. In the non-interacting limit ($U = 0$) the solution can be found analytically and the Green's function can be written as [7]:

$$G_0(\omega) = \frac{1}{\omega - \epsilon_0 - \Delta(\omega) + i0^+}, \tag{2.4}$$

where the bath hybridization function $\Delta(\omega)$ describes the influence of the bath on the impurity and is given by:

$$\Delta(\omega) = \sum_k \frac{|V_k|^2}{\omega - \epsilon_k + i0^+}. \tag{2.5}$$

Since $\Delta(\omega)$ is a weighted sum of bare propagators $(\omega - \epsilon_k + i0^+)^{-1}$, it obeys Kramers-Kronig relations and is therefore completely defined by the spectral function $-\frac{1}{\pi}\Im\Delta(\omega) = \sum_k |V_k|^2\delta(\omega - \epsilon_k)$.

Unitary transformations that act non-trivially only on the bath degrees of freedom do not change any measurable quantity on the impurity. This is reflected in Eq. 2.4 by the fact that the impurity Green's function depends on a single function $\Delta(\omega)$, not on the precise Hamiltonian of the bath. Such unitary transformations relate different representations of the bath to each

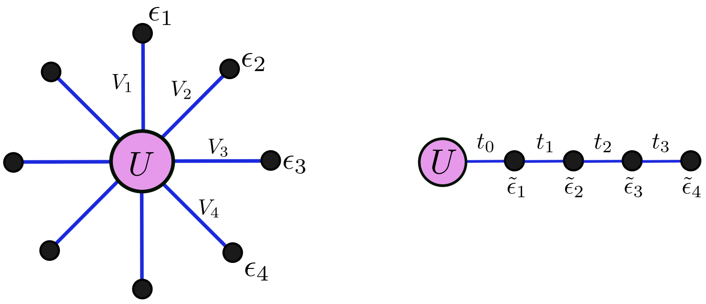

Figure 1: Depiction of an AIM in star geometry (left) and in Wilson chain geometry (right). In star geometry the Hamiltonian supports hopping terms from the impurity to *all* bath sites, but not between bath sites. In the Wilson chain the impurity couples only to the first bath site while the Hamiltonian of the bath is essentially a tight binding model with site-dependent on-site energies $\tilde{\epsilon}_n$ and hopping amplitudes t_n.

other. In Eq. 2.1 the bath is in the so called star geometry. A different representation is the Wilson chain [19] with Hamiltonian:

$$H = H_{\mathrm{loc}} + t_0 \left(c^\dagger_{0\sigma} c_{1\sigma} + h.c. \right) + \sum_{n\sigma} \tilde{\epsilon}_n n_{n\sigma} + t_n \left(c^\dagger_{n\sigma} c_{n+1\sigma} + h.c. \right). \tag{2.6}$$

It can be obtained from the star geometry using a Lanczos-like tridiagonalization [20]. The conceptual differences between star-geometry and the Wilson chain are depicted in Fig. 1. The Wilson chain is essentially a one-dimensional nearest-neighbor tight binding model with an interacting impurity. In star geometry on the other hand, hoppings from the impurity to every bath site exist, but no hoppings between bath sites. Imagining the star geometry on a one-dimensional chain, the hopping terms would be long-range.

Usually the bath of an AIM is considered to represent a continuum of states described by the bath spectral function. Solving an AIM with wave function based numerical methods, restricts the maximal number of bath sites to some value N_b. Therefore, we can only find an approximation to the true, continuous bath hybridization:

$$-\frac{1}{\pi}\Im\Delta_{N_b}(\omega)=\sum_{k=1}^{N_b}|V_k|^2\delta(\omega-\epsilon_k)\approx\sum_{k=1}^{N_b}|V_k|^2\frac{\eta}{\pi\left((\omega-\epsilon_k)^2+\eta^2\right)},\tag{2.7}$$

where we used the representation of the δ-distribution as a Lorentz function and introduced a finite broadening η to get rid of the non-analyticities. For an approximate description of the continuum model, one needs to make sure that in the limit of infinite number of bath sites the two spectral functions must be identical, i.e.:

$$\lim_{N_b\to\infty}\int|\Im\Delta(\omega)-\Im\Delta_{N_b}(\omega)|^2d\omega=0.\tag{2.8}$$

Finding bath parameters ϵ_k and V_k for given bath spectral function is called discretization of the bath. The choice of discretization scheme defines the obtainable resolution in energy. For example, the great success of the Numerical Renormalization Group (NRG) [19, 20] is based on a logarithmic discretization in energy. It uses only a few bath sites for high energies, but places more and more sites the closer one gets to the Fermi energy. Intuitively, it is clear that this method excels at describing the low-energy physics, but has a harder time giving correct descriptions of the high-energy charge fluctuations. By a subsequent transformation to Wilson chain geometry, Wilson was able to implement a renormalization group approach adding one bath site at a time and solving the long standing Kondo-problem [7, 8, 19]. Sacrificing resolution at very low energies allows us to use more equally spaced discretization schemes. One of the the easiest discretizations is to split the ω-axis into N_b equidistant intervals I_l of size $\Delta\epsilon$ for $l\in\{1\cdots N_b\}$ and calculate the bath parameters from [20]:

$$\begin{aligned}|V_k|^2&=\int_{I_l}-\frac{1}{\pi}\Im\Delta(\omega)\\ \epsilon_k&=\min I_l+\frac{\Delta\epsilon}{2}.\end{aligned}\tag{2.9}$$

We note that the accuracy of the bath representation, given by $\Delta\epsilon$, defines a time scale after Fourier transform. Therefore, from $\Delta\epsilon$ we can estimate the time scale where time evolution will not show finite size effects (for example during the calculation of the Green's function). Apart from this way of discretization, we also employ a different scheme, where we choose the bath energy ϵ_k such that all hybridizations V_k are equal (see Sec. 6).

2.1 Multi-Orbital Models

In order to describe the physical situation of an open f- or d-shell, the simple single-orbital model in Eq. 2.1 needs to be extended. Since in the multi-orbital case the impurity also has orbital degrees of freedom, the hybridization function, as well as all other Green's functions become a matrix with orbital indices[2] $\Delta_{m,m'}(\omega)$ (m and m' label the different orbitals). In the most general case, one has to deal with non-diagonal entries that cannot be diagonalized for all energies ω. In the present thesis we will not focus on non-diagonal hybridizations, but treat only hybridization functions $\Delta_{m,m'}(\omega) = \Delta_m(\omega)\delta_{m,m'}$. In this case the bath spectral function can be represented by a separate bath for each impurity orbital and the different orbitals couple only via the interaction part of the local Hamiltonian H_{loc}. This construction keeps the overall form of the AIM in Eq. 2.1 intact. Thus, the Hamiltonian of a multi-orbital [3] AIM is given by:

$$\begin{aligned} H &= H_{\text{loc}} + \sum_{mk\sigma} \epsilon_{mk} n_{mk\sigma} + V_{mk}\left(c^{\dagger}_{m0\sigma} c_{mk\sigma} + \text{h.c.}\right) \\ H_{\text{loc}} &= \sum_{m\sigma} \epsilon_{m0} n_{m0\sigma} + H_{\text{int}}. \end{aligned} \tag{2.10}$$

H_{int} contains the interactions that act only on the impurity degrees of freedom. Importantly, the Hamiltonian in Eq. 2.10 does not include hopping terms between bath sites of different orbitals. Contrary to the single-orbital model, where $U n_{\uparrow} n_{\downarrow}$ is the only possible interaction, the choice of interaction Hamiltonian is much more involved in the multi-orbital case. Depending on

---

[2] Note that already in the single level case $\Delta(\omega)$ is formally a diagonal matrix with spin indices σ and σ'

[3] Such a model is also called multi-channel AIM.

the symmetry of the impurity states different interaction Hamiltonians are possible. Especially important for the present work is the so called Kanamori Hamiltonian [21] discussed in the following.

Kanamori Hamiltonian and Atomic Multiplets

Since the impurity is supposed to describe localized d (or f) states, it is only natural to respect their symmetry properties in the interaction Hamiltonian as a first approximation. For a full d-shell this would correspond to the Slater Hamiltonian [22]. The symmetry of the host material often breaks the full rotational atomic symmetry, leading to different interaction Hamiltonians. For example, the crystal field of the octahedral oxygen environment in cubic transition metal oxides splits the otherwise 5-fold degenerate transition metal d-orbitals into two high energy e_g orbitals and three t_{2g} orbitals at lower energy. For the t_{2g} subspace, the most general interaction respecting the rotational symmetry is the so called Kanamori Hamiltonian [21, 23]:

$$\begin{aligned} H_{\text{int}} = {} & \underbrace{U \sum_{m} n_{m0\uparrow} n_{m0\downarrow} + U' \sum_{m'>m,\sigma} n_{m0\sigma} n_{m'0\bar{\sigma}} + (U'-J) \sum_{m'>m,\sigma} n_{m0\sigma} n_{m'0\sigma}}_{H_{DD}} \\ & + \sum_{m'>m} \underbrace{\left(J \left(c^{\dagger}_{m0\uparrow} c_{m0\downarrow} c_{m'0\uparrow} c^{\dagger}_{m'0\downarrow} + \text{h.c.} \right) - J \left(c^{\dagger}_{m0\uparrow} c^{\dagger}_{m0\downarrow} c_{m'0\uparrow} c_{m'0\downarrow} + \text{h.c.} \right) \right)}_{H^{\text{SF-PH}}_{m,m'}} . \end{aligned} \tag{2.11}$$

The parameters U, U' and J are Coulomb integrals of the screened interaction [23]. Throughout this thesis we use $U' = U - 2J$, needed for rotational symmetry. The first term in Eq. 2.11 is the energy cost of having two electrons in the same orbital with opposite spin, i.e.: a double occupation. Compared to the other density-density terms it has the highest magnitude. The second term (intermediate magnitude) is the interaction between two electrons in different orbitals with opposite spin. The third term (lowest magnitude) gives the cost of having electrons in different orbitals with the same spin. When filling the orbitals it is hence energetically favorable to first add the electrons in different orbitals with the same spin, reflecting Hund's

Table 1: Eigenenergies (atomic multiplet structure) and degeneracy of the first three sectors of particle number N of the Kanamori Hamiltonian Eq. 2.11.

Particle Number N	Eigenenergies	Degeneracy
0	0	1
1	0	6
2	$U-3J$	9
2	$U-J$	5
2	$U+2J$	1
3	$3U-9J$	4
3	$3U-6J$	10
3	$3U+4J$	6

rule. The terms in the second line of Eq. 2.11 are the so called spin-flip and pair-hopping terms. The former exchanges two particles in different orbitals if their spins are anti-parallel, while the latter can be interpreted as a hopping of a double occupation from one orbital to another.

The spectrum of the Kanamori Hamiltonian for the first three sectors of total particle number N is shown in Tab. 1. We find that most particle sectors have more than one non-degenerate eigenenergy. Single particle excitations add a particle to the ground state which is located in one sector of particle number. The ground state determines which of the atomic excitations are reproduce by these single-particle excitations. For example, consider the ground state to be the paramagnetic combination of all 6 degenerate states in the $N=1$ particle sector:

$$|GS\rangle = \frac{1}{\sqrt{6}}\left(|\uparrow,0,0\rangle + |\downarrow,0,0\rangle + |0,\uparrow,0\rangle + \cdots\right). \tag{2.12}$$

Then we expect the single-particle excitation (of this atomic problem) to show all 3 multiplets of the $N=2$ particle sector:

$$c^{\dagger}_{1\uparrow}|GS\rangle = \frac{1}{\sqrt{6}}\left(|\uparrow\downarrow,0,0\rangle + |\uparrow,\uparrow,0\rangle + |\uparrow,\downarrow,0\rangle\cdots\right). \tag{2.13}$$

For the Kanamori Hamiltonian, the first two states above already give all three possible excitations. The double occupation is part of two states with different excitation energies and the second state in 2.13 is part of the remaining one.

If, on the other hand, the ground state is in the $N = 3$ particle sector it is given by (Hund's rule):

$$|GS\rangle = \frac{1}{\sqrt{2}} \left(|\uparrow, \uparrow, \uparrow\rangle + |\downarrow, \downarrow, \downarrow\rangle \right). \tag{2.14}$$

Removing a particle[4] leads to:

$$c_{1,\uparrow} |GS\rangle = \frac{1}{\sqrt{2}} |0, \uparrow, \uparrow\rangle , \tag{2.15}$$

which is an eigenstate of the Kanamori Hamiltonian. Both, the pair-hopping (no double occupations) and the spin-flip term, trivially annihilate this state. Therefore, in this case, we expect only a single excitation energy.

Hence, depending on the GS, multiplet structures can be present in single-particle excitations. From a theoretical viewpoint, these considerations are reflected in the spectral function of the single-particle Green's function (Eq. 2.3):

$$A(\omega) = -\frac{1}{\pi} \Im G(\omega). \tag{2.16}$$

It shows a delta-peak at each reachable excitation energy relative to the ground state. When using the Kanamori Hamiltonian as interaction term of a multi-orbital AIM, it would be very surprising if none of these atomic charge fluctuations survives the coupling to the bath. In other words, we expect that the impurity Green's function of a multi-orbital AIM should show signs of the atomic excitations, similar to the one band case, where the atomic excitations are the lower- and upper Hubbard band [24]. Yet, so far, none of the existing impurity solvers has been capable of resolving such multiplet structures.

---

[4] Adding one would be equivalent regarding the number of excitations.

2.2 Impurity Solvers

The importance of impurity models, especially for DMFT (see next section) led to the development or adaptation of many numerical methods to solve impurity problems. A non-exhaustive introduction to the most important methods is given below.

Exact Diagonalization (ED) [25–27] is a zero-temperature method and provides the Green's function directly on the real frequency axis. Its major weakness is the limited system size (number of bath sites) it can deal with, due to the exponential growth of the Hilbert space. This disadvantage is especially severe for multi-orbital models, since only a very small number of bath sites per orbital can be employed. Even for a single orbital, ED shows finite size effects in the impurity spectral function (see Sec. 5).

Also ideas originating from quantum chemistry are used to solve impurity models. Configuration Interaction (CI) based methods use an expansion of the ground state in excitations around one or more reference determinants [28–30]. Although using ED techniques, CI solvers focus only on a restricted part of the full Hilbert space. Excitations from one (or more) reference determinants build up this restricted subspace. CI-methods provide real frequency spectra and can be employed for a large number of orbitals (so far up to eight using 2 bath sites per orbital in Ref. [31]). For a single orbital, a large number of bath sites ($\mathcal{O}(100)$) can be employed [28]. Still, for multi-orbital calculations, the number of bath sites has so far been limited ($\mathcal{O}(20)$).

The already mentioned Numerical Renormalization Group (NRG) [19, 20] does not suffer from a limited number of bath sites. On the contrary, it is built around adding bath sites with ever decreasing energy scale. NRG allows to obtain the impurity spectrum on the real frequency axis with exceptional resolution around the Fermi energy due to the logarithmic discretization of the bath. That way the low-energy spin-fluctuations are included with high accuracy. At the same time, this is also a weakness of NRG, as the logarithmic discretization only allows for poor resolution of the high-energy charge fluctuations. NRG can be applied to multi-orbital problems, see Refs. [32–34] for three band calculations and Ref. [35] for a five-band calculation by exploiting non-abelian symmetries. Finally let us note, that NRG can be formulated with Matrix Product States [36].

Quantum Monte Carlo (QMC) [37], and especially the Continuous Time (CTQMC) variants [14, 15] are nowadays considered to be the state of the art methods for solving multi-orbital impurity problems. CTQMC relies on a sampling from the path-integral formulation of the partition function and is therefore a finite temperature method. It usually calculates the Greens function on the imaginary frequency axis, where the method is statistically exact. However, to obtain real-frequency spectra, one is forced to perform an ill-posed analytic continuation. In Sec. 7 we show that such an analytic continuation is not able to resolve high energy features in the impurity spectrum (see Fig. 28), when the Greens function is subject to statistical noise. For more complicated Hamiltonians (spin-orbit coupling, more complicated interactions, non-diagonal hybridizations), CTQMC suffers from a fermionic sign problem disallowing access to arbitrary low temperatures. With respect to the number of orbitals, CTQMC has been successfully used for a full f-shell [38, 39], i.e.: a seven-orbital calculation. Although real-frequency approaches for CTQMC exist [40], they have so far only been employed for a single-orbital model. Nevertheless, real-time CTQMC is promising new development.

The solution of impurity models with MPS-based algorithms has a long history [24, 41–61] and a large number of methods capable of calculating the spectral function exist. For selected publications that demonstrate the capabilities of MPS based methods see [24, 46, 48, 49]. While finite temperature formulations of DMRG [5] exist [17], MPS-based methods usually calculate

---

[5] Here we use DMRG in a much broader context meaning all sorts of algorithms that use MPS.

the impurity Green's function at zero temperature. Compared to CTQMC, the biggest advantages of DMRG is that it does not suffer from a fermionic sign problem and the impurity spectrum can be calculated directly at the real-frequency axis. Another major advantage of DMRG is that it allows to use a large number of bath sites ($\mathcal{O}(100)$), as well as to employ any discretization of the bath. The latter is the most important difference to NRG, in that MPS allows to resolve charge fluctuations in the spectrum with much higher precision. For example, sharp high-energy excitations in the Hubbard band were found [24] and later interpreted as originating from effective low-energy doublon-holon interactions [62]. The biggest challenge for MPS based algorithms is the small number of orbitals it can deal with. To describe the low-lying t_{2g} bands of transition metal oxides in cubic symmetry, a three orbital solver would be needed. Using real-time evolution, the solution of an AIM within DMFT was achieved for a two orbital model [24]. Unfortunately, three orbital models proved to be very difficult using this method, because the matrix dimension needed grows very fast with the number of orbitals. Although by mixing real- and imaginary time evolution it was possible to effectively solve a six-orbital model, this came at the cost of a rather small bath [47]. Overall, MPS based algorithms show great potential also for multi-orbital calculations. Therefore we decided to base our approach on MPS.

Before we introduce MPS, we stay a little longer with impurity models and show how they are used in the context of DMFT in the next section.

3 Dynamical Mean Field Theory

Metzner and Vollhardt demonstrated that fermions in the limit of infinite-dimensional systems possess non-trivial correlations and that diagrammatic calculations actually become easier than in the finite dimensional case [9]. Based on this publication, it was shown that in the same limit, lattice models with on-site interactions can be mapped exactly onto AIMs [10] (Eq. 2.1). Since this mapping is far from trivial, the solution has to be found self consistently. Finding such a self consistent mapping between a lattice model and an AIM is essentially Dynamical Mean Field Theory (DMFT) [11, 63]. For the derivation of the DMFT self-consistency equations and for details about DMFT itself, we refer to one of the several extensive reviews on this topic [11, 13, 63].

In the present thesis we will explain the steps necessary to perform a DMFT calculation for the single-orbital Hubbard model:

$$H = -t \sum_{<ij>\sigma} (c^\dagger_{i\sigma} c_{j\sigma} + h.c.) + U \sum_{i} n_{i\uparrow} n_{i\downarrow} + \epsilon_0 \sum_{i\sigma} n_{i\sigma}. \tag{3.1}$$

The first term in Eq. 3.1 is the kinetic energy, described by a nearest-neighbor hopping process with strength t. The second term, an on-site interaction penalizing double occupations. The third term, is just a chemical potential determining the total occupation number. In passing we note that for $\epsilon_0 = -\frac{U}{2}$ the Hubbard model is particle-hole symmetric (only for nearest-neighbor hoppings). To *derive* the DMFT self-consistency equations, we start with the statement that in finite dimensional systems DMFT is an approximation on the level of the self energy:

$$\Sigma(\boldsymbol{k}, \omega) = G_0(\boldsymbol{k}, \omega)^{-1} - G(\boldsymbol{k}, \omega)^{-1}, \tag{3.2}$$

with $G_0(\boldsymbol{k}, \omega) = \frac{1}{\omega - (\epsilon_{\boldsymbol{k}} - \epsilon_0) + i0^+}$. The dispersion $\epsilon_{\boldsymbol{k}}$ is obtained from diagonalization of the kinetic energy of the lattice Hamiltonian (Eq. 3.1) by a Fourier transform. As stated in Eq. 3.2, the self energy is a function of momentum $\boldsymbol{k}$ (spatial correlations) and energy ω (temporal correlations). The DMFT approximation now is to neglect spatial correlations, i.e.: the $\boldsymbol{k}$-dependence of the self energy:

$$\Sigma(\boldsymbol{k},\omega) \approx \Sigma(\omega). \tag{3.3}$$

Using the $\boldsymbol{k}$-independent self energy, we can calculate the local Green's function $G_{\mathrm{loc}}(\omega) = G_{ii}$ (inverting the Fourier transform from real-space to $\boldsymbol{k}$-space):

$$G_{\mathrm{loc}}(\omega) = \sum_{\boldsymbol{k}} G(\boldsymbol{k},\omega) = \sum_{\boldsymbol{k}} \frac{1}{\omega - (\epsilon_{\boldsymbol{k}} - \epsilon_0) - \Sigma(\omega) + i0^+}. \tag{3.4}$$

Since the self energy is $\boldsymbol{k}$-independent, it is local in real-space and we obtain a local Green's function with removed local interactions by:

$$\mathcal{G}_0(\omega)^{-1} = G_{\mathrm{loc}}(\omega)^{-1} + \Sigma(\omega). \tag{3.5}$$

In literature, $\mathcal{G}_0(\omega)$ is called quantum Weiss effective field, which is the dynamical analog of the Weiss field in standard mean-field theory [11]. It is important not to confuse $\mathcal{G}_0(\omega)$ with the local non-interacting lattice Green's function. On the contrary, $\mathcal{G}_0(\omega)$ is the combined effect of the environment of site i, obtained from the *interacting* lattice model by only taking local correlations into account, i.e.:, from the frequency-dependent self energy $\Sigma(\omega)$ (Eq. 3.5). In other words, the influence of all other sites onto site i is encoded in the Weiss field, a single frequency-dependent function. Hence, for site i the precise form of the Hamiltonian describing all other sites becomes unimportant, as long as its effect on site i is given by $\mathcal{G}_0(\omega)$. Therefore, we can choose an effective model that couples to site i, as long as it gives the correct Weiss field $\mathcal{G}_0(\omega)$. An AIM (Eq. 2.1) is especially suited for this task, since we can use the bath parameters ϵ_l and V_l to represent the Weiss field [6].

We identify the Green's function of a non-interacting impurity model (Eq. 2.4) with the Weiss field, and calculate the bath spectral function $\Delta(\omega)$:

$$\Delta(\omega) = \omega - \epsilon_0 - \mathcal{G}_0(\omega)^{-1}. \tag{3.6}$$

---

[6] In this section, we label the bath indices with l instead of k to avoid confusion with the lattice momentum $\boldsymbol{k}$

This then defines the bath parameters (Eq. 2.9) and with it the impurity model.

The major difficulty in this mapping is that in order to calculate the Weiss field $\mathcal{G}_0(\omega)$, we would need to know the self energy. Since this is of course not the case, one uses a self-consistent approach in practice:

1. Start with a self energy $\Sigma^{\text{latt}}(\omega) = 0$ or any other valid guess.
2. For given $\Sigma^{\text{latt}}(\omega)$, determine the chemical potential of the lattice model ϵ_0 to obtain the correct filling (for example from $G_{\text{loc}}(\omega)$ in Eq. 3.4) [7].
3. Calculate $G_{\text{loc}}(\omega)$ using Eq. 3.4 and obtain the bath spectral function $\Delta(\omega)$ from Eqs. 3.5 and 3.6.
4. Obtain bath parameters, for example from Eq. 2.9 (only necessary for Hamiltonian based solvers).
5. Calculate the impurity self energy $\Sigma^{\text{imp}}(\omega)$ with an impurity solver: $\Sigma^{\text{imp}}(\omega) = \left(G_0^{\text{imp}}(\omega)\right)^{-1} - \left(G^{\text{imp}}(\omega)\right)^{-1}$ with $G_0^{\text{imp}}(\omega)$ and $G_0^{\text{imp}}(\omega)$ defined in Eq. 2.4 and Eq. 2.3 respectively.
6. $\Sigma^{\text{imp}}(\omega)$ is a new guess for the lattice self energy $\Sigma^{\text{latt}}(\omega) = \Sigma^{\text{imp}}(\omega)$. Iterate this procedure by going back to step (2) until convergence.

Finally, we note that DMFT is not only exact in infinite-dimensional systems, but has two more exact limits. *First:* DMFT is trivially exact in the non-interacting limit ($U = 0$), as the self energy is zero and therefore definitely $\boldsymbol{k}$-independent. *Second:* DMFT becomes exact for $t = 0$. In this case, all sites are independent. Therefore, the self energy is local in real-space and again $\boldsymbol{k}$-independent after Fourier transform.

---

[7] For a one-orbital model there is no distinction between chemical potential and on-site energy. For multi-orbital models one needs to keep them separated by replacing $\epsilon_0 \rightarrow \epsilon_0 - \mu$, since the on-site energies can be orbital-dependent, but the chemical potential cannot.

3.1 Density-Functional Theory + DMFT

Density-Functional Theory (DFT) gives excellent descriptions of the electronic structure of many classes of real materials [64–66]. It describes the spectrum of the Hamiltonian with bands, labeled by the single-particle Bloch-momentum. However, for strongly-correlated materials, DFT can fail drastically, e.g., by wrongly predicting a material to be metallic, while in fact it is insulating. DMFT on the other hand is capable of treating such strongly-correlated systems with local interactions in a non-perturbative way.

The combination of these methods is therefore one of the most successfully employed schemes to describe strongly-correlated materials [11–13]. In the present thesis we will not discuss the details on how to combine DFT with DMFT, but only mention the most important aspects.

The idea of DFT+DMFT is to use the low-energy bands (close to the Fermi energy) of the DFT calculation to construct the kinetic-energy part of a Hubbard model. Depending on the number of bands studied, this will be single- or a multi-orbital (multi-channel) Hubbard model. In the present thesis we employ projective Wannier functions [67, 68] to construct such localized orbitals.

The interaction parameters of this Hubbard model (U and J in our case, see Eq. 2.11) can be estimated, with the constrained Random-Phase Approximation (cRPA) [69–72] or the constrained Local-Density Approximation (cLDA) [73]. Here, we do not use these methods, but either estimate values for the interaction parameters by comparing calculated and experimentally measured spectra, or use values from the literature.

DFT already incorporates some of the electronic correlations, including the Hartree and exchange correlations. Since DMFT would account for them a second time, a so called Double-Counting (DC) correction Σ^{DC} is necessary. It acts as a static shift of the self energy, by replacing $\Sigma(\omega) \to \Sigma(\omega) - \Sigma^{\mathrm{DC}}$ in the DMFT self-consistency equations. Exact expressions for the DC are not known, but several approximations exist [74–78]. In the present thesis we use the so called Fully-Localized-Limit (FLL) DC (Eq. (45) in Ref. [78]) and adjust it if it gives physically incorrect spectra.

4 Matrix Product States and Density Matrix Renormalization Group

The Density Matrix Renormalization Group (DMRG) [16], originally introduced as a variant of the NRG, quickly became one of the most powerful methods to treat one dimensional quantum systems. Soon, the connection of DMRG to MPS was realized [79, 80], i.e.: that DMRG can be interpreted as a variational method on the space of MPS. Nowadays, this connection is so strong that it seems difficult to think of DMRG without MPS. For this reason, we will not introduce DMRG as done by White [16], but start with MPS and use the variational principle to search for ground states. This approach to some extent limits the understanding of the basic ideas behind DMRG for which we refer to the standard literature [16, 17, 81]. This section largely follows the thorough review by Schollwöck [17].

4.1 Singular Value Decomposition

In the following sections we will make extensive use of Singular Value Decompositions (SVD). For any matrix M with dimension $(N_A \times N_B)$ there exists a decomposition as:

$$M = USV^\dagger, \tag{4.1}$$

with the following properties:

- U has dimensions $(N_A \times N)$, with $N = \min(N_A, N_B)$ and is what we call left-normalized i.e.: $U^\dagger U = \mathbb{1}$
- $V^\dagger$ has dimensions $(N \times N_B)$ and is right-normalized i.e.: $V^\dagger V = (V^\dagger)(V^\dagger)^\dagger = \mathbb{1}$
- S is a diagonal matrix of dimension $(N \times N)$ with non-negative entries $S_1, S_2 \cdots S_N$ called singular values.

We choose the singular values in descending order $S_1 \geq S_2 \geq S_3 \cdots \geq S_N$. The number of non-zero singular values is called the *rank* of matrix M.

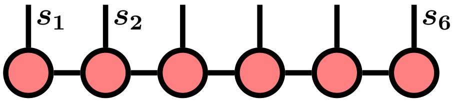

Figure 2: Graphical representation of an MPS. Every circle corresponds to a tensor A^{s_i} and each line to an index of this tensor. In this picture, the physical indices are the vertical lines, while the horizontal lines correspond to the bond indices. Connected lines mean that the corresponding index is summed over. Fixing all the physical indices s_i for each site results in a tensor of rank zero with the value of the coefficient $c_{s_1,\cdots,s_N}$.

For our purpose, one of the most important properties of the SVD is that it allows to approximate a matrix M of rank m with a different matrix $\tilde{M}$ of smaller rank $\tilde{m} < m$. With the Frobenius norm $\left(||M||_F = \sum_{ij} |M_{ij}|^2\right)$ as a measure of distance, one finds that the optimal solution to this problem is given by:

$$\tilde{M} = U\tilde{S}V^\dagger \text{ , with } \tilde{S} = \text{diag}(S_1, S_2, \cdots, S_{\tilde{m}}, 0, \cdots, 0). \tag{4.2}$$

I.e.: the best low-rank approximation can be found by taking only the $\tilde{m}$ largest singular values, but keeping U and $V^\dagger$ unchanged [82].

The computational complexity of a SVD scales as $\mathcal{O}(N_A^2 N_B)$ for $N_A < N_B$. For a square matrix, this gives a $\mathcal{O}(N^3)$ scaling that will be the bottleneck of the algorithms presented below.

4.2 MPS Construction

Consider a (one dimensional) lattice consisting of N sites with local state space $|s_i\rangle$ of dimension d_i at site i. To keep the notation simple, we often omit subscripts in site indices and use $d_i = d$, but keep in mind that the local state space can be site-dependent. Any quantum state $|\psi\rangle$ can of course be expanded in this local basis:

$$|\psi\rangle = \sum_{\{s_i\}} c_{(s_1\cdots s_N)} |s_1 \cdots s_N\rangle . \tag{4.3}$$

In basic quantum mechanics one is taught to view the coefficient $c_{(s_1 \cdots s_N)}$ as an entry in a vector (rank one tensor). Hence, we put brackets around the indices, indicating that they are actually grouped into a single vector-index. A much more natural perspective is to think of it as a rank N tensor with d entries for each tensor index. We denote this by omitting the brackets: $c_{s_1 \cdots s_N}$. By regrouping indices, we can arrive at different representations of this tensor. For example, interpreting s_1 as the first group of indices and $s_2 \cdots s_N$ as the second, we can rewrite it as a highly asymmetric matrix $c_{(s_1),(s_2 \cdots s_N)}$. A SVD of this matrix gives:

$$c_{(s_1),(s_2 \cdots s_N)} = \sum_{a_1} U_{s_1,a_1} \underbrace{S_{a_1,a_1} (V^\dagger)_{a_1,s_2 \cdots s_N}}_{c_{a_1,s_2 \cdots s_N}} = \sum_{a_1} U_{s_1,a_1} c_{a_1,s_2 \cdots s_N} . \tag{4.4}$$

U_{s_1,a_1}, is a rank two tensor (matrix) where the first index s_1 labels the actual basis state, while the second index a_1 is an artificial index resulting from the SVD. In MPS-notation we treat them differently and write $A^{s_1}_{a_1} = U_{s_1,a_1}$, with an upper index s_1. In a second step we repeat the above procedure, but now for the tensor $c_{a_1,s_2 \cdots s_N}$. We write it as a matrix $c_{(a_1,s_2),(s_3 \cdots s_N)}$, perform a SVD $c_{(a_1,s_2),(s_3 \cdots s_N)} = \sum_{a_2} U_{(a_1,s_2),a_2} S_{a_2,a_2} (V^\dagger)_{a_2,s_3 \cdots s_N}$ and define $U_{(a_1,s_2),a_2} = A^{s_2}_{a_1,a_2}$, yielding:

$$c_{s_1,s_2 \cdots ,s_N} = \sum_{a_1,a_2} A^{s_1}_{a_1} A^{s_2}_{a_1,a_2} c_{a_2,s_3 \cdots s_N} . \tag{4.5}$$

We continue to perform these steps until:

$$\begin{aligned} c_{s_1,s_2 \cdots s_N} &= \sum_{\{a_i\}} A^{s_1}_{a_1} A^{s_2}_{a_1,a_2} \cdots A^{s_{N-1}}_{a_{N-2},a_{N-1}} A^{s_N}_{a_{N-1}} \text{ , and hence} \\ |\psi\rangle &= \sum_{\{s_i\},\{a_i\}} A^{s_1}_{a_1} A^{s_2}_{a_1,a_2} \cdots A^{s_{N-1}}_{a_{N-2},a_{N-1}} A^{s_N}_{a_{N-1}} |s_1, \cdots , s_N\rangle . \end{aligned} \tag{4.6}$$

This factorization of the rank N tensor $c_{s_1,s_2 \cdots s_N}$ into N tensors of rank three [8] is what we call an MPS. For fixed physical index s_i the rank three tensor

---

[8] Except the first and N-th tensor which are of rank two.

$A^{s_i}_{a_{i-1},a_i}$ becomes a matrix, hence the name *Matrix* Product State. We could obtain the coefficient of the expansion in Eq. 4.3 from multiplication (contraction) of the matrices [9]:

$$c_{s_1,s_2\cdots s_N} = A^{s_1}A^{s_2}\cdots A^{s_N}, \tag{4.7}$$

with the first (last) matrix being actually a column (row) vector. We call the basis-state index s_i physical index and the *matrix*-index a_i bond index. This construction demonstrates that any quantum mechanical state can be represented as an MPS. For the present manuscript it is often more useful to think about the *matrices* A^{s_i} as being rank three tensors with indices A_{s_i,a_{i-1},a_i}. This allows to understand generalizations of MPS (tensor networks) much easier. Hence, throughout this work we will mostly use the term tensor to denote for A^{s_i}.

Being confronted with expressions like in Eq. 4.6 for the first time can be a bit overwhelming, because of the large number of indices to keep track of. Therefore, the so called graphical representation, shown in Fig. 2, is usually used to represent tensor networks. It allows to quickly understand the underlying tensor structure. Every circle (or other shape) in the graphical representation corresponds to one of the tensors A^{s_i} and each line to an index of this tensor. Connected lines denote a summation of the corresponding index. For example, the horizontal connected lines in Fig. 2 give rise to the *matrix products* of the MPS.

4.3 Canonical Forms

It turns out that an MPS-representation of a quantum state $|\psi\rangle$ is not unique. The transformation [83] $A^{s_i}_{a_{i-1},a_i} \to \sum_m A^{s_i}_{a_{i-1},m} G_{m,a_i}$ and $A^{s_{i+1}}_{a_i,a_{i+1}} \to \sum_l (G^{-1})_{a_i,l} A^{s_{i+1}}_{l,a_{i+1}}$ leaves the state invariant for any invertible matrix G. Such a transformation is shown in Fig. 3. This gauge degree of freedom enables us to find different MPS representations for the same state $|\psi\rangle$, with useful properties. In the last section, during the construction of the MPS, we already

---

[9] In practice the coefficient is *never* evaluated. Calculations are performed exclusively in MPS-form.

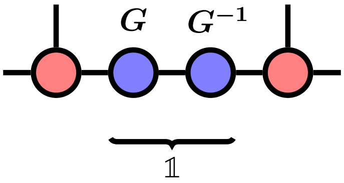

Figure 3: The representation of a quantum mechanical state as MPS is not unique. For any invertible matrix G we can multiply G to the right of A^{s_i} and G^{-1} to the left of $A^{s_{i+1}}$ on any bond i, leaving the state $|\psi\rangle$ invariant.

encountered one of these representations. The A-tensors of the MPS are nothing but reshaped U-matrices from a SVD, with the property $U^\dagger U = \mathbb{1}$. For the MPS-tensors this means:

$$\sum_{a_{i-1},s_i} (A^{s_i\dagger})_{a_i,a_{i-1}} A^{s_i}_{a_{i-1},a'_i} = \delta_{a_i a'_i}. \tag{4.8}$$

This property is called left normalization, shown in Fig. 4 (a). If an MPS consists exclusively of left-normalized tensors we call it left-canonical.

In the above construction of the MPS we started at the first site and moved from the left to the right to obtain the A-tensors. Of course, we could also have started at the last site and move to the left. In this case we use the $V^\dagger$-matrices of the SVD as MPS tensors and denote them B^{s_i} to discriminate them from the left-normalized A-tensors:

$$|\psi\rangle = \sum_{\{s_i\},\{a_i\}} B^{s_1}_{a_1} B^{s_2}_{a_1,a_2} \cdots B^{s_{N-1}}_{a_{N-2},a_{N-1}} B^{s_N}_{a_{N-1}} |s_1, \cdots, s_N\rangle \,. \tag{4.9}$$

We call the normalization property of the B-tensors right-normalized meaning that:

$$\sum_{a_i,s_i} B^{s_i}_{a'_{i-1},a_i} (B^{s_i\dagger})_{a_i,a_{i-1}} = \delta_{a_{i-1}a'_{i-1}}. \tag{4.10}$$

This property is shown in Fig. 4 (b). If every tensor in an MPS is right-normalized we call it right-canonical MPS.

We can use SVDs not only to construct MPS, but also to change for example from right to left normalization. Assume we have a right-normalized

Figure 4: a.) $\sum_s (A^s)^\dagger A^s$ of a left-normalized tensors A yields the identity matrix which we depict as an arc. b.) Similarly $BB^\dagger$ gives the identity matrix if B is right-normalized. It is convention to represent *daggered* tensors like $A^\dagger$ with the physical index pointing downwards.

MPS consisting only of B-tensors as in Eq. 4.9. To obtain an A-tensor we take the first B-tensor and perform a SVD:

$$B^{s_1}_{a_1} \equiv B_{(s_1),(a_1)} = \sum_{\tilde{a}_1} U_{s_1,\tilde{a}_1} S_{\tilde{a}_1,\tilde{a}_1} (V^\dagger)_{\tilde{a}_1,a_1}. \tag{4.11}$$

Then we multiply $SV^\dagger$ onto B^{s_2}, removing the index a_1 (since it is summed over) and rename $\tilde{a}_1 \to a_1$ giving the following tensors:

$$\begin{aligned} B^{s_1}_{a_1} B^{s_2}_{a_1,a_2} &= A^{s_1}_{\tilde{a}_1} M^{s_2}_{\tilde{a}_1,a_2} \text{ , with} \\ M^{s_2}_{\tilde{a}_1,a_2} &= \sum_{a_1} S_{\tilde{a}_1,\tilde{a}_1} (V^\dagger)_{\tilde{a}_1,a_1} B^{s_2}_{a_1,a_2} \to M^{s_2}_{a_1,a_2} \\ A^{s_1}_{\tilde{a}_1} &= U_{s_1,\tilde{a}_1} \to A^{s_1}_{a_1}. \end{aligned} \tag{4.12}$$

Above, we introduced M-tensors to signal that they have no normalization property, since the multiplication of $SV^\dagger$ onto B^{s_2} destroys its right normalization. After this, we obtain another MPS, still describing the exact same quantum mechanical state but neither in right nor left-canonical form:

$$|\psi\rangle = \sum_{\{s_i\},\{a_i\}} A^{s_1}_{a_1} M^{s_2}_{a_1,a_2} B^{s_3}_{a_2,a_3} \cdots B^{s_N}_{a_{N-1}} |s_1, \cdots, s_N\rangle \, . \tag{4.13}$$

If we continue with these steps for all sites, we end up with a left-normalized MPS consisting only of A-tensors.

For algorithms, left and right-canonical MPS are of minor importance. What makes DMRG and all other methods so powerful is the intermediate form given by Eq. 4.13. Assume we performed the steps to go from right to left-canonical form for all sites $k < i$. The MPS then is given by:

$$|\psi\rangle = \sum_{\{s_i\}} A^{s_1} \cdots A^{s_{i-1}} M^{s_i} B^{s_{i+1}} \cdots B^{s_N} |s_1, \cdots, s_N\rangle \,. \tag{4.14}$$

This is called the mixed-canonical form with orthogonality center i, where all tensors of sites $k < i$ are A-tensors and all sites $k > i$ are B-tensors. From now on, we will often suppress bond indices to make the notation more readable and only use them when needed. From the mixed-canonical form, we can go one step further and use a SVD on the matrix $M_{(s_i, a_{i-1}),(a_i)}$

$$\begin{aligned} M^{s_i} B^{s_{i+1}} &= U S V^\dagger B^{s_{i+1}} = A^{s_i} S \underbrace{V^\dagger B^{s_{i+1}}}_{\tilde{B}^{s_{i+1}}} \\ |\psi\rangle &= \sum_{\{s_i\}} A^{s_1} \cdots A^{s_{i-1}} A^{s_i} S \tilde{B}^{s_{i+1}} \cdots B^{s_N} |s_1, \cdots, s_N\rangle \,. \end{aligned} \tag{4.15}$$

It can be checked easily that $\tilde{B}^{s_{i+1}}$ is again a right-normalized tensor. The importance of this representation is that Eq. 4.15 is actually the Schmidt decomposition of $|\psi\rangle$ with respect to the two subsystems $\mathcal{A}$ consisting of all sites $k \leq i$ and $\mathcal{B}$ consisting of all other sites. To prove this statement, we define the following states:

$$\begin{aligned} |a_i\rangle_{\mathcal{A}} &= \sum_{s_1 \cdots s_i} (A^{s_1} A^{s_2} \cdots A^{s_i})_{1,a_i} |s_1 \cdots s_i\rangle \\ |a_i\rangle_{\mathcal{B}} &= \sum_{s_{i+1} \cdots s_N} (B^{s_{i+1}} B^{s_{i+2}} \cdots B^{s_N})_{a_i,1} |s_{i+1} \cdots s_N\rangle \,. \end{aligned} \tag{4.16}$$

With the normalization properties of the A- and B-tensors it is easy to show [17] that $|a_i\rangle_{\mathcal{A}}$ is a set of normalized, orthogonal vectors, i.e.: a basis if it is complete[10]. The same is true for $|a_i\rangle_{\mathcal{B}}$. Hence, we can directly write

---

[10] In all, but the simplest calculations the bond dimension is restricted, meaning that $\{|a_i\rangle_{\mathcal{A}}\}$ is not complete. Still, it is often referred to as a basis.

down the Schmidt composition from Eq. 4.15:

$$|\psi\rangle = \sum_i S_i \, |a_i\rangle_{\mathcal{A}} \, |a_i\rangle_{\mathcal{B}} \,. \tag{4.17}$$

This means that, the singular values S_i of the center tensor M are the Schmidt values of $|\psi\rangle$ in the bi-partition $\mathcal{A}$ - $\mathcal{B}$.

4.4 Entanglement and MPS-Approximation

All of the above does not yet explain the success of MPS-based algorithms. To represent a general state of the Hilbert space as MPS, we would need an exponentially growing bond dimension. The largest tensor is then situated in the middle of the chain and would have $\left(d^{\frac{L}{2}} \times d^{\frac{L}{2}}\right) = d^L$ entries, as large as the whole Hilbert space. Hence, the two previous sections would be not more than a nice linear algebra exercise if it were not for the so called area law of the von Neumann entanglement entropy (also entanglement entropy) [84]. The entanglement entropy is defined as the Shannon entropy of the reduced density matrix

$$\rho_{\mathcal{A}} = tr_{\mathcal{B}} \rho = tr_{\mathcal{B}} \, |\psi\rangle \, \langle\psi| = \sum_i S_i^2 \, |a_i\rangle \, \langle a_i| \,. \tag{4.18}$$

$tr_{\mathcal{B}}$ means the partial trace over subsystem $\mathcal{B}$, i.e.: summation over a complete set of eigenvectors of system $\mathcal{B}$. Hence, we find for the entanglement entropy S_A:

$$S_{\mathcal{A}} := -tr \left(\rho_{\mathcal{A}} \log \rho_{\mathcal{A}}\right) = -\sum_i S_i^2 \log S_i^2. \tag{4.19}$$

If we assume all Schmidt coefficients equal $S_i = S = m^{-1}$ (m is the number of Schmidt values), we find for the entropy $S_{\mathcal{A}} = \log m$. As it turns out, this is the maximal value obtainable from m Schmidt values. Hence, to describe states with a high von Neumann entropy, one needs at least $m \sim e^{S_{\mathcal{A}}}$ Schmidt values. Since the number of Schmidt values is the bond dimension, MPS are a very efficient representation of states with low entanglement even when using only manageable tensor dimensions.

Fortunately, the area law of entanglement states that the entropy of ground states of gapped, quantum systems with short range interactions is not extensive (proportional to the volume), but proportional to the surface of the bipartition. For one-dimensional systems, this surface consists of a single point, and the entropy is thus constant $S_{\mathcal{A}} \sim$ const. This means, that ground states in 1d occupy only a tiny fraction of the full Hilbert space, namely those states with non-extensive entanglement entropy. This is the same subset that MPS are able to describe well, explaining the huge success of MPS-based methods. In practice this means, that we approximate the exact wave function $|\psi\rangle$ by an MPS with restricted bond dimension (typically $\mathcal{O}(100)$ to $\mathcal{O}(1000)$). To obtain tensors of manageable size, we need to *truncate* the MPS matrices. Truncation is defined as keeping only the m largest eigenvalues of $\rho_{\mathcal{A}}$. The error of this approximation is called truncated weight:

$$t_w = 1 - \sum_{i>m} S_i^2. \tag{4.20}$$

To avoid loss of normalization, the density matrix has to be re-normalized after truncation, i.e.: $\rho_{\mathcal{A}} \rightarrow \frac{1}{1-t_w}\rho_{\mathcal{A}}$.

To summarize, the area-law of entanglement allows us to represent ground states of one-dimensional systems using MPS with a limited, i.e.: numerically manageable bond dimension. The normalization of the reduced density matrix guarantees $\sum_i S_i^2 = 1$, enabling us to discern which Schmidt coefficients are large and which are not and hence can be discarded (truncation). It is important to note that if the MPS is not in mixed-canonical form (no orthogonal vectors) truncation is NOT safe and can be numerically unstable.

This argument does not only hold for MPS. For general tensor networks, safe truncation is possible as long as for each bond, some part of the system can be defined as being strictly to the left and the other part strictly to its right. This allows to calculate the Schmidt decomposition and to truncate the tensor network safely. This insight strongly influences the tensor network

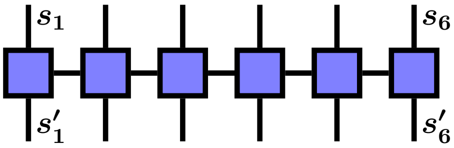

Figure 5: We can represent operators as MPOs the same way we represent states as MPS. The difference is that MPOs have two physical indices instead of one, since operators always consist of bra and ket vectors.

that we propose in Sec. 6 to solve AIMs.

4.5 Matrix Product Operators (MPO)

In complete analogy to the construction of MPS we can start with the expansion of an operator in the same basis $|s_1 \cdots s_N\rangle$ and write it as a Matrix Product Operator (MPO):

$$\begin{aligned} H &= \sum_{\{s_i\},\{s'_i\}} c_{(s_1 \cdots s_N),(s'_1 \cdots s'_N)} |s_1 \cdots s_N\rangle \langle s'_1 \cdots s'_N| \\ &= \sum_{\{s_i\},\{s'_i\}} W^{s_1,s'_1} W^{s_2,s'_2} \ldots W^{s_N,s'_N} |s_1 \cdots s_N\rangle \langle s'_1 \cdots s'_N| \,. \end{aligned} \tag{4.21}$$

Contrary to MPS, the W-tensors of MPOs are in general rank four tensors, with rank three tensors at the first and last site as shown in Fig. 5. We see that the difference to an MPS is that an MPO has two physical indices corresponding to the bra and ket vectors of the operator. For Hamiltonians with short range interactions it is not hard to find MPO representations with small bond dimensions [17, 85]. Even for certain classes of long range interactions this is possible, see for example [86] and Sec. 5.1 of the present thesis.

MPOs allow us to treat states and operators on the same footing i.e.: as a product of tensors. For example, the expectation value of the energy (Eq. 4.22) can be depicted as in Fig. 6 [11]. Similarly, overlaps $\langle\phi|\psi\rangle = \langle\phi|\mathbb{1}|\psi\rangle$

---

[11] Without the $\langle\psi|\psi\rangle$ normalization in the denominator

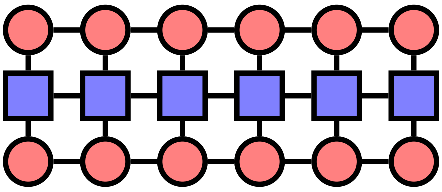

Figure 6: The true power of the graphical representation shows itself when calculating expectation values like $\langle\psi| H |\psi\rangle$. At a glance we see which indices we have to sum over (contract) and we also see whether the result is a scalar (as in this case) or a different tensor (if it has open lines sticking out).

can be calculated as shown in Fig. 6 by imagining the operator to be the identity or, easier, just omitting it. The concept of MPOs will simplify the search for ground states which we discuss in the next section.

4.6 Density Matrix Renormalization Group (DMRG)

Thinking of MPS as a clever *parametrization* of one-dimensional ground states, the basic idea behind DMRG seems almost natural. If we view the tensor elements of the MPS as variational parameters we can minimize the expectation value of the energy:

$$E = \min_{\{A^{s_i}\}} \frac{\langle\psi| H |\psi\rangle}{\langle\psi|\psi\rangle}. \tag{4.22}$$

Since the optimization of every tensor at once is a much too high-dimensional problem, DMRG uses a different approach. In a single step of DMRG, all but one tensors stay fixed. After the minimum with respect to this tensor is found, we move to one of the neighboring tensors resulting in a right-left-right sweep (assuming we start on the left). The tensor on site i minimizing the energy can be found, from the extrema of a Lagrange function $\mathcal{L}$ with Lagrange multiplier λ, ensuring normalization:

$$\begin{aligned} \mathcal{L} &= \langle\psi| H |\psi\rangle - \lambda\langle\psi|\psi\rangle \\ \frac{d\mathcal{L}}{dA^{s_i}_{a_{i-1},a_i}} &\overset{!}{=} 0. \end{aligned} \tag{4.23}$$

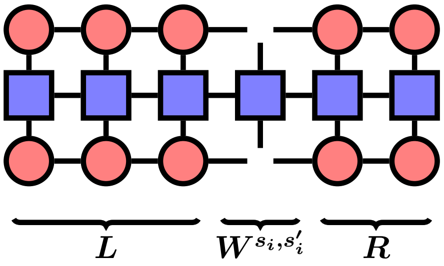

Figure 7: Graphical representation of the effective Hamiltonian H^{eff} in Eq. 4.24. It is a matrix given as a tensor product of 3 tensors L, R and W^{s_i,s'_i}. Therefore, we can efficiently find the lowest eigenvector and eigenvalue using an iterative eigenvalue solver.

If we use the mixed-canonical form of the MPS with orthogonality center at site i, this results in a standard eigenvalue problem [17]:

$$\sum_{s'_i,a'_{i-1},a'_i} H^{\mathrm{eff}}_{(s_i,a_{i-1},a_i),(s'_i,a'_{i-1},a'_i)} A_{(s'_i,a'_{i-1},a'_i)} = \lambda A_{(s_i,a_{i-1},a_i)}. \tag{4.24}$$

Instead of writing detailed formulas for the effective Hamiltonian, we only show its graphical representation in Fig. 7. It is a matrix with dimension $(dm^2 \times dm^2)$ assuming left and right bond indices of the MPS both have dimension m. Because H^{eff} is a tensor product of three tensors L, R and W, the full matrix never needs to be built. This allows for a solution with an iterative eigenvalue solver that finds the lowest energy eigenstate (e.g.: Lanczos). When the tensor A^{s_i} minimizing the energy is found, we move to the next site $i+1$ or $i-1$ depending on whether we perform a sweep to the right or to the left. There, we again set the orthogonality center to this site, calculate the effective Hamiltonian and obtain the eigenvector minimizing the energy. Of course there are many more details on how one can do this very efficiently that can be found in [17]. Nevertheless, for the purpose of the present thesis, this very crude description of DMRG suffices.

We note that it is often better to optimize two neighboring tensors at site i and $i+1$ in a single step. This approach, called 2-site DMRG, allows to dynamically optimize the bond dimension and usually does not get stuck in

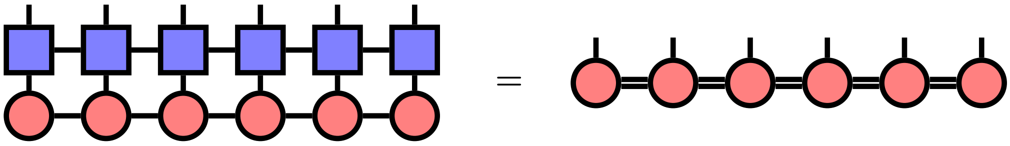

Figure 8: The application of an MPO with bond dimension w to an MPS with bond dimension m results in an MPS with bond dimension mw. In order to avoid unbounded growth of bond dimension the MPS has to be truncated.

local minima as often. Finally, we want to stress that as in the last section, DMRG works as long as we can define some part of the tensor network being strictly to the *left* and the rest being to the *right* of the site currently optimized.

4.7 Time Evolution

MPS not only allow us to search for ground states, but there also exist powerful algorithms to perform time evolution in real- or imaginary time. Since time evolved states are no ground states anymore, there is no guarantee that we can represent them well using MPS. In practice this shows itself in that we can time evolve only up to some maximal time, at which the bond dimension needed grows too large to continue. In the worst case scenario for closed quantum systems, the entropy grows linearly in time, producing an exponential growth of the bond dimension. Nevertheless, time evolution based on MPS can be a powerful tool, as long as one is not interested in the very long time behavior, or if the entanglement saturates or grows very slowly in time. In open quantum systems, MPS based time evolution can even access the steady state [87, 88]. In the present thesis, we use a mix of two algorithms: the first we call MPO-based and the second is the so called time-dependent DMRG (tDMRG) [17, 89].

MPO-based time evolution

Assume that we found an MPO (see Fig. 5) representation of the time evolution operator $e^{-iH\Delta t}$ for some small time step Δt. Then we can simply apply the operator to the MPS over and over again.

$$|\psi(N\Delta t)\rangle = (e^{-iH\Delta t})^N |\psi(0)\rangle \tag{4.25}$$

The application of an MPO with bond dimension w to an MPS with bond dimension m yields another MPS with bond dimension mw i.e.: the bond dimensions multiply. This would lead to an unbounded growth of tensor dimensions (see Fig. 8). The simplest possibility to prevent this is to truncate the MPS using SVDs in a two sweep process. The MPO destroys any normalization property of the MPS, which needs to be restored, before we are allowed to truncate. Therefore, we first have to bring it into e.g.: right-canonical form. This is done by starting at the last site and performing SVDs for each tensor *without truncation*. In doing this we obtain an orthonormal basis and are allowed to truncate in a left-to-right sweep.

In the present thesis we use a shortcut proposed in Ref. [90]. A good approximation to an orthonormal basis can be found by also bringing the MPO into right-canonical form. Then one can apply the MPO and truncate in the same step. It should be mentioned that there are more elaborate methods of applying MPOs. For our purpose this simple method suffices though, since the MPOs we will be interested in do not act on the whole lattice, but only on a few sites.

Time-Dependent DMRG

tDMRG is based on a Suzuki-Trotter [91] decomposition of the time evolution operator $e^{-iH\Delta t}$. Often the Hamiltonian consists of nearest-neighbor terms $H = \sum_i h_{i,i+1}$. Then we can write it as $H = \sum_{\text{i:even}} h_{i,i+1} + \sum_{\text{i:odd}} h_{i,i+1} = h_{\text{even}} + h_{\text{odd}}$, decomposing it into a sum of operators starting at even and odd bonds. All terms of each individual sum commute, but the sums itself do not. Still, we can approximate the time evolution operator using a second

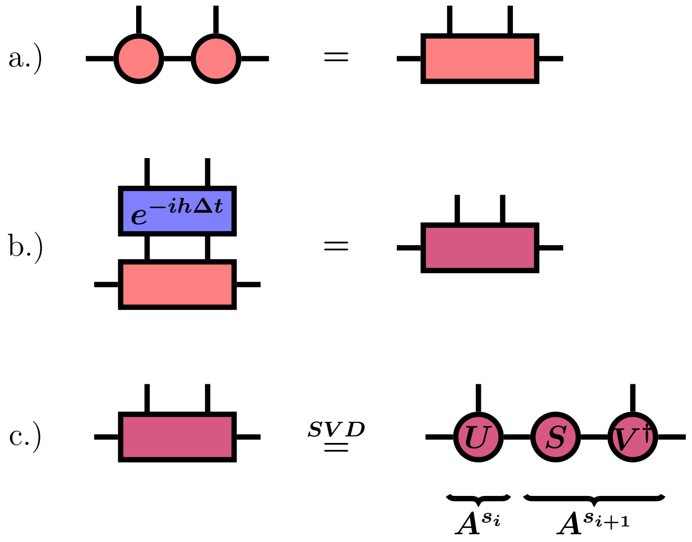

Figure 9: Application of a two-site gate acting on sites i and $i+1$ of an MPS.
a.) First the two tensors A^{s_i} and $A^{s_{i+1}}$ are combined into a 4-legged tensor by summation over its common bond index.
b.) Apply the gate $e^{-ih\Delta t}$ onto this tensor by contraction over the two physical indices. The result is again a tensor of rank four.
c.) A SVD decomposes this rank four tensor back into two MPS-tensors. If the MPS is in the mixed-canonical form, centered at site i or $i+1$ we can truncate safely at this point. Depending on whether the next gate is to the left or to the right we multiply the S-matrix of the SVD onto the left or the right MPS-tensor (the picture shows S added to the right tensor).

order decomposition:

$$\begin{aligned} e^{-iH\Delta t} &= e^{-ih_{\text{even}}\frac{\Delta t}{2}} e^{-ih_{\text{odd}}\Delta t} e^{-ih_{\text{even}}\frac{\Delta t}{2}} + \mathcal{O}(\Delta t^3) \\ e^{-ih_{\text{even}}\frac{\Delta t}{2}} &= \prod_{\text{i:even}} e^{-ih_{i,i+1}\frac{\Delta t}{2}} \\ e^{-ih_{\text{odd}}\Delta t} &= \prod_{\text{i:odd}} e^{-ih_{i,i+1}\Delta t}. \end{aligned} \tag{4.26}$$

Eq 4.26 consists of products of operators acting non-trivially only on two neighboring sites. We will call such operators time evolution gates or just gates. We proceed by applying these gates one at a time. The steps necessary to apply a single gate are shown in Fig. 9. This scheme allows to dynamically increase (decrease if one is very fortunate) the bond dimension during time evolution, ensuring that the truncation error does not grow out of bounds. Finally we want to stress that tDMRG as well as the Suzuki-Trotter decomposition are not restricted to nearest-neighbor Hamiltonians only. The Trotter decomposition is used just to separate exponentials of non-commuting operators. As we will see in the next section, the combination of a Suzuki-Trotter decomposition with tDMRG, can used to time evolve certain kinds of long-range interactions as well.

4.8 Real-Time Green's Functions

The combination of DMRG with time evolution algorithms allows us to calculate Green's functions (Eq. 2.2) in real time at zero temperature using MPS. First, we split the propagator into the usual greater ($G^>$) and lesser Green's function ($G^<$)[12]:

$$\begin{aligned} G(t) &= -i\Theta(t)\left(\langle c(t)c^\dagger\rangle + \langle c^\dagger c(t)\rangle\right) \\ &= -i\Theta(t)\left(\underbrace{\langle ce^{-iHt}c^\dagger\rangle e^{iE_0t}}_{G^>(t)} + \underbrace{\langle c^\dagger e^{iHt}c\rangle e^{-iE_0t}}_{G^<(t)}\right), \end{aligned} \tag{4.27}$$

with E_0 the ground state energy. To calculate $G^>$ we perform the following steps:

- Calculate the ground state $|\psi_0\rangle$ and its energy E_0 with DMRG.
- Apply the creation operator $c^\dagger |\psi_0\rangle$
- Time evolve this state $|\psi(t)\rangle = e^{iHt}c^\dagger |\psi_0\rangle$.
- Calculate the overlap to obtain the Green's function $G^>(t) = \langle\psi_0| ce^{iHt}c^\dagger |\psi_0\rangle e^{-iE_0t} = \left(c^\dagger |\psi_0\rangle\right)^\dagger |\psi(t)\rangle e^{-iE_0t}$.

---

[12] We omit any indices (spin or site) for the creation/annihilation operators

The same recipe works for $G^<$, by swapping creation and annihilation operators and changing the sign of the time evolution. In practice one can improve on this by splitting the time evolution evenly between the bra and the ket vector [92]:

$$G^>(t) = \left(e^{-iH\frac{t}{2}} c^\dagger \left|\psi_0\right\rangle\right)^\dagger \left(e^{iH\frac{t}{2}} c^\dagger \left|\psi_0\right\rangle\right) e^{-iE_0 t}. \tag{4.28}$$

The two separate time evolutions, both to $\frac{t}{2}$, allow to reach longer times, since the entanglement produced during time evolution is split between the bra and ket vector.

5 MPS Impurity Solver

As discussed in Sec. 2.2, there exist a large number of methods to solve impurity problems using MPS-based techniques. Here, we will focus on real-time evolution, since it allows to resolve sharp features in the spectral function [24].

First, let us discuss the single-orbital case. Before we start with algorithmic details, we have to choose a local basis, the order in which we arrange the sites in the MPS, as well as the fermionic order. It turned out to be numerically favorable to separate the two spin species [24], since they only interact at the impurity (see Eq. 2.1). Hence, we place the impurity in the middle of the MPS, the spin-up degrees of freedom to its left and the spin-down degrees of freedom to its right. This arrangement is depicted in Fig.10 and we see that the lattice consists of a total of $N = 2N_b + 2$ sites. At this point it is important to make a clear distinction between two types of geometry. The first type is the representation of the bath of an AIM. The bath can be represented either in the star- (Eq. 2.1), or chain geometry (Eq. 2.6), see also Fig. 1. The second type is the geometry of the tensor network, in our case the MPS which always has a linear (i.e.: also chain-like) arrangement of tensors. Those two geometries are *a priori* independent of each other, but one bath representation might be better suited for MPS than the other (see below). The fermionic order we choose is the same order in which we arrange the sites, i.e.: we represent any basis state in Fock space as:

$$(c^\dagger_{1\uparrow})^{n_{1\uparrow}} \cdots (c^\dagger_{N_b\uparrow})^{n_{N_b\uparrow}} (c^\dagger_{0\uparrow})^{n_{0\uparrow}} (c^\dagger_{0\downarrow})^{n_{0\uparrow}} (c^\dagger_{N_b\downarrow})^{n_{N_b\downarrow}} \cdots (c^\dagger_{1\downarrow})^{n_{1\downarrow}} \left|0\right\rangle . \tag{5.1}$$

MPS and Star Geometry

Traditionally, impurity solvers using MPS performed the calculation in the chain geometry representation of the bath (Eq. 2.6). There are several reasons for this. First, the construction of ever decreasing energy scales in NRG depends on the chain geometry and hence, it was the first choice for impurity

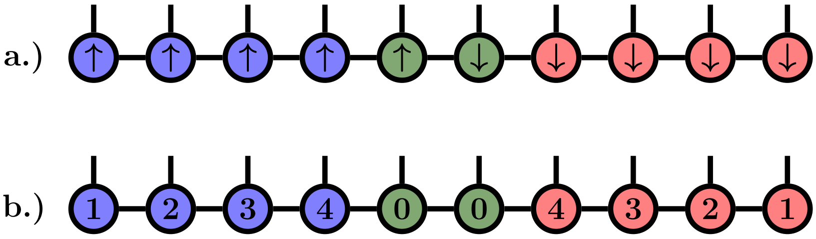

Figure 10: Arrangement of sites when using MPS for a AIM with 4 bath sites ($N_b = 4$). a.) We choose to place the impurity (green) in the middle and the spin-up (spin-down) bath degrees of freedom to its left (right). b.) Indices of the AIM-Hamiltonian for this arrangement. The bath site with index $k = 4$ is closest to the impurity for each spin. The index decreases towards the left (right) for spin up (down) respectively. Note that the impurity has index $k = 0$. This picture might look similar to the picture of the chain geometry in Fig. 1, but it is important to understand that we have not yet specified any representation of the bath. In the chain geometry, every hopping term would act on two neighboring sites in the MPS. In the star geometry on the other hand, the hoppings would be long range, coupling the impurity to every bath site.

solvers using the closely related DMRG. More importantly though, the star geometry seems to be incompatible with the linear tensor geometry of an MPS, because hopping terms from the impurity to *all* bath sites exist. At first glance, it is not clear how to construct MPOs and especially how to perform the time evolution in the star geometry. However, the chain geometry has one disadvantage: At particle hole symmetry, its bath on-site energies $\tilde{\epsilon}_n$ are exactly zero. We therefore expect the ground state to be a complicated linear combination of all the possibilities of distributing the particles on all sites. This means that we anticipate to need rather large bond dimensions in the MPS.

This is very different when we represent the bath in star geometry. Wolf *et al.* [49] demonstrated that the star geometry can be a superior representation than the chain geometry in terms of tensor size of the MPS. Their argument is that on-site energies ϵ_k are direct excitations of the bath spectral function $-\frac{1}{\pi}\Im\Delta(\omega)$ in Eq. 2.5. If we assume $-\frac{1}{\pi}\Im\Delta(\omega)$ to be non-zero only inside an interval $[-D, D]$, we will find some bath on-site energies ϵ_k close to $-D$

and D, i.e.: with high and low energies. Most likely the ground state has most contributions from occupied low-energy bath sites and unoccupied high-energy bath sites. Therefore, these bath sites have small entanglement to the rest of the lattice, which implies low bond dimensions when placed at the borders of the MPS. In the present thesis, we hence focus on the star geometry representation of the bath. Therefore, we order the bath sites according to their on-site energy in ascending order and place the low-energy sites at the edges of the MPS (i.e.: the sites with highest on-site energy are placed close to the impurity). In the following section we will show how to construct the MPO, which to the best knowledge of the author has not been published before. Furthermore, we devise an efficient scheme how to perform time evolution in the star geometry, first published in [1] - one of the main publications of the author. Contrary to Wolf *et al.* [49], who used Krylov-based time evolution, the approach presented here, is much closer to the well established tDMRG [17].

5.1 Construction of the MPO in Star Geometry

MPOs (Eq. 4.21) are tensor networks of tensors with four indices [93] i.e.: two physical indices and two bond-indices (Fig. 5). We usually think of these tensors as a matrix (two indices) of local operators (two indices), see for example Eq. 5.5. The matrix indices correspond to the bond indices, and the operator indices are of course the physical indices. The first and the last MPO-tensors are row and column vectors respectively. If we multiply all vectors and matrices in the correct order, we obtain the Hamiltonian. For the construction of MPOs, the first insight we need is that when writing Hamiltonians we use in fact an abbreviation. The term $c_2^\dagger c_3$, for example, is a shorthand for:

$$\mathbb{1} \otimes c_2^\dagger \otimes c_3 \otimes \mathbb{1} \otimes \cdots \otimes \mathbb{1}. \tag{5.2}$$

Each Hamiltonian is a sum of such terms. Our goal is to find matrices that, when multiplied, produce every one of them. To find the MPO of an AIM with the bath in star geometry, we apply the following rules, starting at the leftmost tensor:

- Every site (except the first) has a matrix index coming from the left given by the left bond index of the MPO in Fig. 5. Each entry of this index has a string (possibly a sum of strings) of operators from all sites to its left, corresponding to the first few terms in Eq. 5.2 (e.g.: $\mathbb{1} \otimes c_2^\dagger$ if the current site is the third site).
- Find the operator strings, which will be needed *separately* at later sites and give each of them a separate outgoing matrix index by adding the corresponding local operators of the current site. This outgoing matrix index corresponds to the right bond index of the MPO in Fig. 5
- If operator strings are not needed separately at later sites, e.g., when only their sum is needed, combine these into a single outgoing index by adding the corresponding local operators of the current site.
- Move on to the next site, at which the outgoing index of the current site becomes the incoming index of the next.

So called finite state machines [85, 94] essentially formalize these steps. To make this rather abstract recipe easier to understand let us try to construct the MPO for the Hamiltonian of an AIM in star geometry. First, let us repeat the Hamiltonian:

$$H = \sum_{k\sigma} \epsilon_k n_{k\sigma} + \sum_{k\sigma} V_k \left(c_{0\sigma}^\dagger c_{k\sigma} + \text{h.c.} \right) + \sum_{\sigma} \epsilon_0 n_{0\sigma} + U n_{0\uparrow} n_{0\downarrow} \tag{5.3}$$

We start at the first site, a bath site with spin-up. The Hamiltonian consists of four operators for this site: the on-site term $\epsilon_1 n_{1\uparrow}$, the identity $\mathbb{1}$ and the hybridization terms $V_1 c_{1\uparrow}$ and $V_1 c_{1\uparrow}^\dagger$. Each of them is needed separately at later sites. Since we have no incoming index from the left, the first MPO tensor is given by:

$$W_1 = \begin{pmatrix} \epsilon_1 n_{1\uparrow} & \mathbb{1} & V_1 c_{1\uparrow} & V_1 c_{1\uparrow}^\dagger \end{pmatrix}. \tag{5.4}$$

The second tensor is a bit more interesting. The Hamiltonian has the exact same four terms again, but we do not need them separated. To the right of both on-site energy terms $\epsilon_1 n_{1\uparrow}$ and $\epsilon_2 n_{2\uparrow}$, only identities appear. Therefore, we can put them in the same outgoing index. The second incoming index is the identity of site 1. At later sites we need the identity from site 1 multiplied with the identity from site 2. The third incoming index is one of the long-range hopping terms. At the impurity we do not need every term $V_i c_{i\sigma}$ separately, just their sum to obtain the hybridization $c^\dagger_{0\sigma}\left(\sum_i V_i c_{i\sigma}\right)$ + h.c.. Hence, it is not necessary to give each hopping term a separate MPO-index. Instead, we can put the sum of all terms into a single index and the MPO for the second site is then given by:

$$W_2 = \begin{pmatrix} \mathbb{1} & 0 & 0 & 0 \\ \epsilon_2 n_{2\uparrow} & \mathbb{1} & V_2 c^\dagger_{2\uparrow} & V_2 c^\dagger_{2\uparrow} \\ 0 & 0 & p & 0 \\ 0 & 0 & 0 & p \end{pmatrix}$$

$$\Rightarrow W_1 W_2 = \begin{pmatrix} \sum_{k=1}^{2} \epsilon_k n_{k\uparrow} & \mathbb{1} & \sum_{k=1}^{2} V_k c_{k\uparrow} & \sum_{k=1}^{2} V_k c^\dagger_{k\uparrow} \end{pmatrix}. \tag{5.5}$$

Above, we introduced the Fermi-operator $p = (-1)^n$ (n is the particle number operator) taking care of the Fermi sign, that appears when applying the operator to any basis state i.e.: from the Jordan Wigner transformation [95]. Similar to the identity operator we omit p-operators in results (for example in the bottom tensor in Eq. 5.5) in the following, but write them explicitly for all MPO tensors. We need these p-operators, since the actual operator string of the long range hoppings for fermions in star geometry is given by:

$$\underbrace{\left(\bigotimes_{1}^{k-1} \mathbb{1}\right) \otimes c^\dagger_{k\uparrow} \otimes p \otimes \cdots \otimes p}_{\text{Spin up bath}} \otimes c_{0\uparrow} \otimes \mathbb{1} \otimes \underbrace{\left(\bigotimes_{1}^{N_b} \mathbb{1}\right)}_{\text{Spin down bath}} \tag{5.6}$$

for a hopping from site k to the impurity.

After multiplication, we find that the tensor $W_1 W_2$ has the same entries as W_1, just the on-site energy term, as well as the hopping terms are summed over the first two sites. Therefore, we can repeat the matrix of W_2 for all the following spin-up sites until we reach the first impurity site:

$$W_k = \begin{pmatrix} \mathbb{1} & 0 & 0 & 0 \\ \epsilon_k n_{k\uparrow} & \mathbb{1} & V_k c_{k\uparrow}^\dagger & V_k c_{k\uparrow}^\dagger \\ 0 & 0 & p & 0 \\ 0 & 0 & 0 & p \end{pmatrix}, \text{ for } k \in \{2, \cdots, N_b\}$$

$$\Rightarrow \prod_{k=1}^{N_b} W_k = \begin{pmatrix} \sum_{k=1}^{N_b} \epsilon_k n_{k\uparrow} & \mathbb{1} & \sum_{k=1}^{N_b} V_k c_{k\uparrow} & \sum_{k=1}^{N_b} V_k c_{k\uparrow}^\dagger \end{pmatrix}. \tag{5.7}$$

Instead of continuing with the spin-up impurity, let us first construct the MPO tensors for the spin-down bath. We start at the rightmost site and move to the left, towards the impurity. Using similar arguments as above, the MPO-tensors of the spin-down bath are given by:

$$W_N = \begin{pmatrix} \epsilon_1 n_{1\downarrow} \\ \mathbb{1} \\ V_1 c_{1\downarrow} \\ V_1 c_{1\downarrow}^\dagger \end{pmatrix}, \text{ with } N = 2N_b + 2$$

$$W_{N-(k-1)} = \begin{pmatrix} \mathbb{1} & \epsilon_k n_{k\downarrow} & 0 & 0 \\ 0 & \mathbb{1} & 0 & 0 \\ 0 & V_k c_{k\downarrow}^\dagger & p & 0 \\ 0 & V_k c_{k\downarrow}^\dagger & 0 & p \end{pmatrix}, \text{ for } k \in \{2, \cdots, N_b\}$$

$$\Rightarrow \prod_{k=1}^{N_b} W_{N-(k-1)} = \begin{pmatrix} \sum_k \epsilon_k n_{k\downarrow} \\ \mathbb{1} \\ \sum_k V_k c_{k\downarrow} \\ \sum_k V_k c_{k\downarrow}^\dagger \end{pmatrix}. \tag{5.8}$$

This leaves us with the two impurity tensors. At this point this task is not too difficult and we just state the result:

$$W_{N_b+1} = \begin{pmatrix} 0 & \mathbb{1} & 0 \\ \mathbb{1} & \epsilon_0 n_{0\uparrow} & n_{0\uparrow} \\ 0 & c^\dagger_{0\uparrow} & 0 \\ 0 & c_{0\uparrow} & 0 \end{pmatrix}$$

$$W_{N_b+2} = \begin{pmatrix} \mathbb{1} & \epsilon_0 n_{0\downarrow} & c^\dagger_{0\downarrow} & c_{0\downarrow} \\ 0 & \mathbb{1} & 0 & 0 \\ 0 & U n_{0\downarrow} & 0 & 0 \end{pmatrix}. \tag{5.9}$$

Indeed, if we multiply all tensors we find that we retrieve the Hamiltonian of the AIM in star geometry given by Eq. 2.1. With this MPO representation we can find ground states using DMRG. Next, we discuss how to time evolve in star geometry in order to be able to calculate Green's functions.

5.2 Time Evolution in Star Geometry using Swap Gates

After finding the ground state of an AIM and application of creation (annihilation) operator, we need to calculate the time evolution of this excited state to obtain the Green's function (Eq. 2.2 via Eq. 4.28). One possibility is to use Krylov based algorithms as in Ref. [49] that only need the MPO for time evolution. In the present thesis we employ a new approach which is much closer to tDMRG and is therefore simpler in the sense that the only approximation is to perform a Suzuki-Trotter decomposition.

Our first goal is to find a product of two-site gates that approximates the time evolution operator $e^{-iH\Delta t}$. To do so we define $H_{k\sigma} = \epsilon_k n_{k\sigma} + V_k \left(c^\dagger_{k\sigma} c_{0,\sigma} + \text{h.c.} \right)$ and first split off the local term H_{loc}, using a Suzuki-Trotter decomposition:

$$e^{-iH\Delta t} \approx e^{-iH_{\text{loc}}\frac{\Delta t}{2}} \left(\prod_\sigma e^{-i\sum_k H_{k\sigma}\Delta t} \right) e^{-iH_{\text{loc}}\frac{\Delta t}{2}}. \tag{5.10}$$

As the interaction in H_{loc} is the only term coupling the two spin species, the

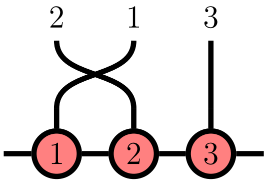

Figure 11: The application of a swap gate, depicted as two crossing arcs. The application of a swap gate acting on sites 1 and 2 gives an MPS in which the actual degrees of freedom of site 1 are located in the second MPS tensor and vice versa. This implies that site 3 is now a neighbor of the degrees of freedom of site 1, which then allows to apply a two-site gate acting only on the degrees of freedom of site 1 and site 3.

remaining time evolution operator trivially splits into a product over spins after this decomposition. Since the two impurity sites are already nearest-neighbors in the MPS, the application of $e^{-iH_{\text{loc}}\frac{\Delta t}{2}}$ is straight forward (see Fig. 9). Next, we deal with the terms involving the bath $e^{-i\sum_k H_{k\sigma}\Delta t}$. By repeated use of Suzuki-Trotter decompositions, we first split off $H_{N_b\sigma}$, then $H_{(N_b-1)\sigma}$ etc. until we are left with the term $H_{1\sigma}$:

$$\begin{aligned} e^{-i\sum_k H_{k\sigma}\Delta t} &\approx \left(e^{-iH_{N_b\sigma}\frac{\Delta t}{2}}\right)\left(e^{-iH_{(N_b-1)\sigma}\frac{\Delta t}{2}}\right)\cdots\left(e^{-iH_{1\sigma}\Delta t}\right)\cdots\left(e^{-iH_{N_b\sigma}\frac{\Delta t}{2}}\right) \\ &= \left(\prod_{k=N_b}^{2} e^{-iH_{k\sigma}\frac{\Delta t}{2}}\right) e^{-iH_{1\sigma}\Delta t}\left(\prod_{k=2}^{N_b} e^{-iH_{k\sigma}\frac{\Delta t}{2}}\right) \end{aligned} \tag{5.11}$$

While Eq. 5.11 is indeed a product of two-site gates, we only know how to apply the first term $e^{-iH_{N_b\sigma}\frac{\Delta t}{2}}$. All other gates couple the impurity to non nearest-neighbor sites. To overcome this issue we use so called swap gates (See Refs. [17, 90, 96, 97] and App. A of the present thesis). Their purpose is to swap the position of two neighboring sites in the MPS. For example, after the application of a swap gate acting on the first and the second site, the degrees of freedom of the first site are now actually on the second tensor of the MPS. Hence, the third site is a nearest-neighbor of the degrees of freedom of the first site. This allows us to apply a gate acting only on the degrees of freedom of site 1 and site 3. This process of swapping two sites is depicted in Fig. 11.

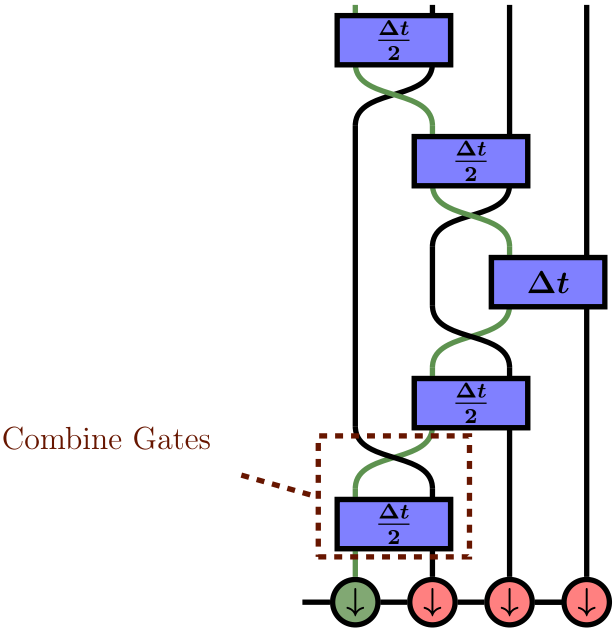

Figure 12: Depiction of the time evolution given by Eq. 5.11 of the spin-down bath in star geometry. The long range hoppings make the use of swap gates necessary. Since we can combine every swap gate with a time evolution gate, this comes with no additional computational cost. The green line visualizes the position of the degrees of freedom of the impurity as it is moved towards the end of the MPS and back again by the swap gates. All gates, except the one at the end of the MPS, need to be applied with half the time step $\frac{\Delta t}{2}$. It is important to note that when swapping the impurity outwards we apply the swap gates *after* the time evolution gate. When swapping the impurity back inwards we need to *first* swap, then time evolve. If we would do it the other way around, we would need to take care of an additional sign stemming from the $\xi = -1$ contributions in Eq. A.1.

Swap gates allow us to perform the time evolution in star-geometry very efficiently. We will explain the time evolution for the spin down bath. The algorithm for the spin-up bath is equivalent. The process discussed below is shown in Fig. 12 for a bath with $N_b = 3$ sites.

Eq. 5.11 tells us to first apply the term $e^{-iH_{N_b\sigma}\frac{\Delta t}{2}}$. After this we usually would perform a SVD as shown in Fig. 9, separating the tensor to retrieve an MPS representation. Here, before we do this, we apply a swap gate, swapping the impurity site with the bath site with index N_b, preparing us for the next time evolution with the term $e^{-iH_{(N_b-1)\sigma}\frac{\Delta t}{2}}$. Now we perform the SVD and obtain an MPS where the impurity and the bath site with index $N_b - 1$ are nearest-neighbors. Next we apply the time evolution gate $e^{-iH_{(N_b-1)\sigma}\frac{\Delta t}{2}}$ and again prepare for the next time evolution by application of a swap gate *before* the SVD. These steps are repeated, until we arrive at the bath site with index 1, which we time evolve as usual, but with full time step Δt (see Eq. 5.11) .

At this point, the impurity degrees of freedom are located at the second last site in the MPS. Since we performed a second order Suzuki-Trotter decomposition, we need to re-apply all time evolution gates again. This gives us the opportunity to swap the impurity back into the middle, which is necessary anyways. Hence, we *first* apply a swap gate swapping the impurity one site to the left, time evolve with $e^{-iH_{(2)\sigma}\frac{\Delta t}{2}}$ and perform a SVD. We repeat this process of swapping *first* and then applying time evolution gates until every gate is dealt with and the impurity is again in the middle of the chain. One of the advantages of this procedure is that we add every swap gate to an actual time evolution gate requiring no additional SVDs.

Before we continue, let us discuss the errors due to the Suzuki-Trotter decomposition. With respect to the time step Δt, all errors are of order $(\Delta t)^3$, since we use a second order breakup. I.e.: terms in the third order of the series expansion differ in the two expressions. More interesting is the error due to the system size N_b, especially compared to the chain geometry. There, we usually use a second order breakup to separate even and odd hopping terms of the Hamiltonian $H = H_{\text{even}} + H_{\text{odd}}$:

$$e^{-i\Delta t H} \approx e^{-i\frac{\Delta t}{2} H_{\text{even}}} e^{-i\Delta t H_{\text{odd}}} e^{-i\frac{\Delta t}{2} H_{\text{even}}}. \tag{5.12}$$

As we show in App. B, the error of the even-odd breakup scales as $\mathcal{O}(N_b)$, while the breakup in Eq. 5.11 scales at most with $\mathcal{O}(N_b^2)$. Surprisingly we find a different behavior in Fig. 13. There, we show the error of the greater Green's function $G^{>}_{\text{exact}} - G^{>}_{\text{DMRG}}$ for the star geometry and the chain geometry for several bath sizes. We find that in all cases the star geometry is superior by more than an order of magnitude. While the error in chain geometry seems to grow linearly with the system size (as expected), in star geometry it does not grow and stays at the surprisingly small value of about $7 \cdot 10^{-7}$ for all bath sizes studied. In these calculations, we found that the maximal bond dimension needed in star geometry (approximately 50) is only about a third of the bond dimension needed for the chain geometry (approximately 150). This emphasizes the huge advantage of the star geometry, since for the computation time this means a speed-up by a factor of 30, while giving results more accurate by more than an order of magnitude.

In Fig. 14 we present the greater Green's function $G^{>}(t)$ for a one-band AIM for $U = 0$ and compare to the exact solution. We note that calculations without interactions suffice to show that this algorithm gives correct results, since the interaction part has been split-off at the beginning in Eq. 5.10, making the time evolution of $e^{-iH_{\text{loc}}\frac{\Delta t}{2}}$ algorithmically independent of the terms connecting the bath and the impurity.

Time evolution in star geometry using swap gates was used in Ref. [3] to benchmark an impurity solver based on Cluster Perturbation Theory (CPT) and exact diagonalization. The contribution of the author of the present thesis to this publication was to perform the MPS calculations and to give support in writing the paper. In Fig. 15 we compare spectral functions obtained from MPS in star geometry to the CPT solver. We find that the MPS-based solver gives smooth spectra without any visible finite size effects,

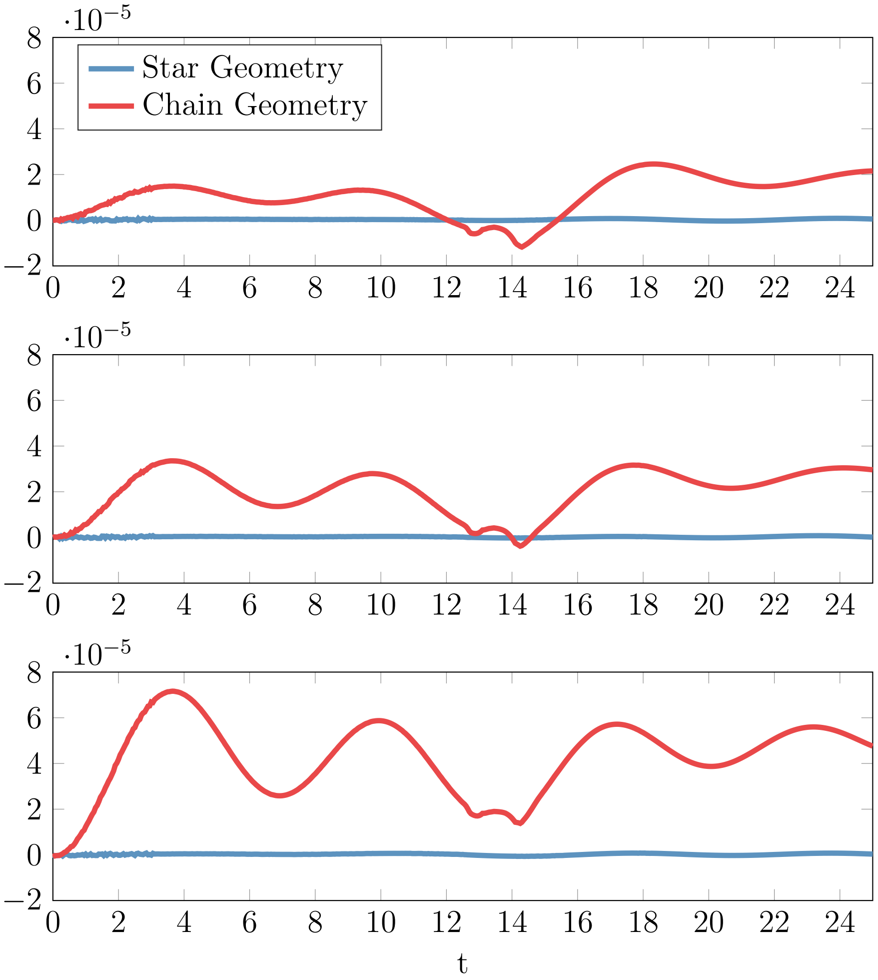

Figure 13: Difference of $G^{>}(t)$ between the exact solution (for $U = 0$) to the DMRG result in star and chain geometry for several bath sizes. *Top*: $N_b = 29$, *Middle*: $N_b = 59$ and *Bottom*: $N_b = 109$. The bath parameters were obtained from a semi-circular bath spectral function $-\frac{1}{\pi}\Im\Delta(\omega) = \frac{1}{2\pi}\sqrt{1-\omega^2}$ using the linear discretization in energy (Eq. 2.9). Note that the exact results differ by $\mathcal{O}(10^{-7})$, because the mapping between star and chain geometry slightly changes the non-interacting Greens function. Therefore, we plot the difference to the respective exact result. The truncated weight of these calculations was 10^{-12} without restricting the bond dimensions. The errors of the star geometry are surprisingly small with a maximal value of about $7 \cdot 10^{-7}$ in all three calculations.

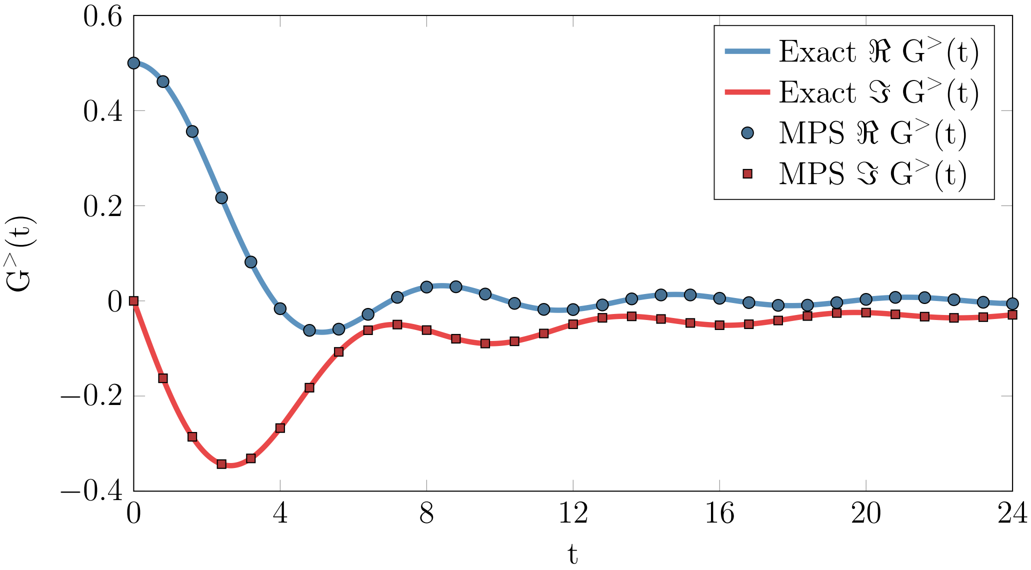

Figure 14: Comparison of the greater Green's function $G^>(t)$ of a one-band AIM between an MPS calculation in star geometry and the exact solution for $U = 0$. Bath parameters are taken from a semi circular bath density of states $-\frac{1}{\pi}\Im\Delta(\omega) = \frac{1}{2\pi}\sqrt{1-\omega^2}$ (normalized to 0.25). The MPS calculation used $N_b = 63$ bath sites with an equidistant discretization in energy (Eq. 2.9). The spectral function of this Green's function is shown in the top plot of Fig. 15.

since it is able to include a large number of bath sites ($N_b = 63$). The purpose of this comparison is to show that even with advanced techniques, a small bath leads to finite size effects in the form of sharp δ-peaks. Hence, a large number of bath sites is necessary to represent the bath hybridization function $\Delta(\omega)$ well enough to avoid such artifacts. In these calculations we used the linear discretization in energy given by Eq. 2.9, allowing for high resolution results at all energies i.e.: not only around the Fermi energy, but also in the Hubbard bands.

5.3 MPS and Multi-Orbital AIMs

The procedure to solve impurity models with MPS as described above is in principle not restricted to one-orbital models, but can be extended to the multi-orbital case (Eq. 2.10). In order to place the sites in the MPS, i.e:, a linear arrangement of tensors, one usually builds super-sites [24, 99]. For the single-orbital model discussed above, the local state space for each site is just two states, empty or occupied ($|0\rangle$ and $|1\rangle$). For an M-orbital model one usually combines M sites (one for each orbital) to a single super-site which then has a local state space of occupied and empty for each orbital, thus dimension 2^M. For example, the local state space for $M = 2$ would be $|0,0\rangle$, $|0,1\rangle$, $|1,0\rangle$ and $|1,1\rangle$ on each site. Hence, we find that the local state space increases exponentially with the number of orbitals. This exponential growth could be cured by placing the sites one after the other, but this often introduces problems in the convergence of DMRG.

Furthermore, we also expect the bond dimension of the MPS to grow very fast with the number of orbitals: Consider a two orbital model with degenerate orbitals (both orbitals have the same bath parameters and on-site energies of the impurity). If these two orbitals do not interact, every eigenstate of this system can be written as a tensor product of eigenstates of each individual orbital:

$$|\psi\rangle = |\psi_1\rangle \otimes |\psi_2\rangle \, . \tag{5.13}$$

For simplicity, we take $|\psi_1\rangle = |\psi_2\rangle = |\psi\rangle$ and assume that $|\psi\rangle$ can be represented as an MPS with bond dimension m. This means that its Schmidt

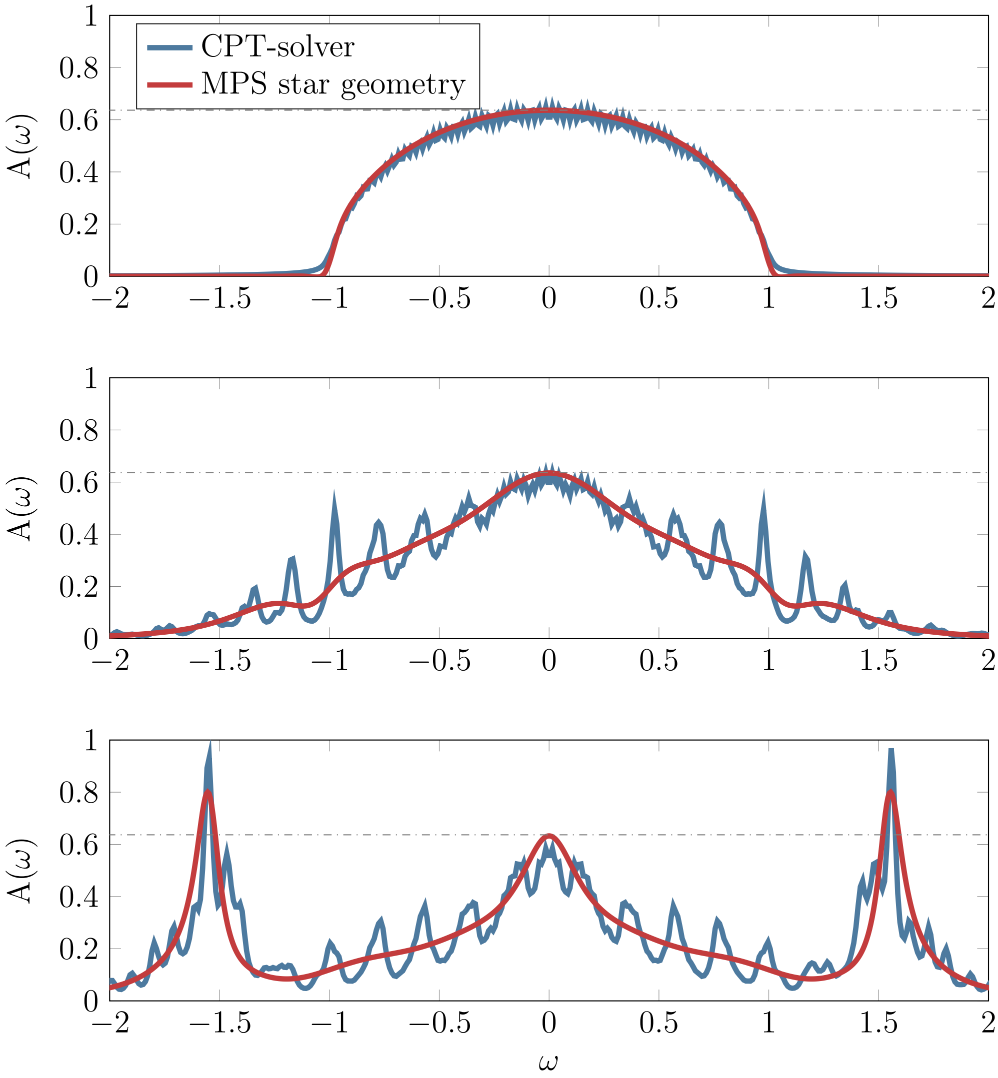

Figure 15: Comparison of impurity spectra obtained with MPS in star geometry to the CPT solver published in [3]. The plot shows results for $U = 0$ (top), $U = 1$ (middle) and $U = 2$ (bottom), for a one band model with the same semi-circular bath as in Fig. 14. The MPS calculation used $N_b = 63$ bath sites and the spectra were obtained by post processing $G(t)$ using linear prediction [98]. The gray dashed-dotted line shows the pinning criteria, stating that $A(\omega = 0) = \frac{2}{\pi}$ for any value of the interaction strength U. We see that MPS gives very accurate results, even around the Fermi energy $\omega = 0$, where the long time behavior of the Green's function determines the spectrum. Furthermore, the large bath allows for smooth spectral functions without any visible finite size effects, contrary to the CPT solver.

decomposition on a relevant bond [13] is given by:

$$|\psi\rangle = \sum_{i=1}^{m} S_i \, |L_i\rangle \otimes |R_i\rangle \,, \tag{5.14}$$

with left- and right bases $|L_i\rangle$ and $|R_i\rangle$. Inserting $|\psi\rangle$ into Eq. 5.13, we obtain:

$$|\psi\rangle = \sum_{i,j=1}^{m} S_i S_j \left(|L_i\rangle \otimes |L_j\rangle\right) \otimes \left(|R_i\rangle \otimes |R_j\rangle\right) . \tag{5.15}$$

This is exactly the Schmidt decomposition of the system using super-sites. It consists of a left basis $(|L_i\rangle \otimes |L_j\rangle)$ and a right basis $(|R_i\rangle \otimes |R_j\rangle)$, both with dimension m^2. Hence, if we want to represent this state as MPS without loosing accuracy, we need a bond dimension of $m^2 = m^{\#\text{orbitals}}$. The same can be done for more than two orbitals and we find that if they are non-interacting, the bond dimension grows exponentially with the number of orbitals. In a sense, this growth is artificial, since for non-interacting orbitals, the best way to place the sites on the lattice would be to arrange the two orbitals one after the other and achieve a representation with bond dimension m. In other words, building the super-sites increases the bond dimensions *unnecessarily* in some sense. The crucial point why the above assumption of non-interacting orbitals is a good starting point for the discussion of interacting orbitals is that in a multi-orbital AIM (Eq. 2.10) the different orbitals only interact via the impurity. The bath degrees of freedom do not couple to each other directly. Electrons move from one bath site to the other exclusively by first hopping onto the impurity. We note that even non-diagonal hybridization functions $\Delta(\omega)_{m,m'}$ can be represented as a bath only coupled to impurity degrees of freedom, see Sec. 7. This special form of the Hamiltonian of AIMs can make one doubt the efficiency of building super-sites. To the best knowledge of the author, for MPS such super-sites are necessary [14] when the orbitals are interacting, since otherwise the im-

---

[13] A bond at which the bond dimension m is needed, not at the beginning or end of the MPS.

[14] For the bond dimension it does not matter whether we truly build super sites, or place the sites one after the other, since we find equivalent Schmidt decompositions in both cases

purity orbitals are far away from each other in the MPS and entanglement between the impurity orbitals needs to be *transported* over the bath bond indices. In the interacting case, we were not able derive similar results as Eq. 5.13. Still, model calculations showed that the bond dimension increases very quickly with increasing number of orbitals, pointing towards a similar problem.

Nevertheless, Ganahl *et al.* demonstrated that for two orbital models the super-sites approach allows to obtain high resolution results employing real time evolution [24] with a large number of bath sites ($\mathcal{O}(100)$). Adding a third orbital, in order to describe the t_{2g} subspace of real materials, seems to be very difficult with this approach though. One possibility would be to exploit non-abelian symmetries in the MPS formalism [35, 100]. Their implementation is rather involved, and for many real materials this symmetry is not realized. Another possibility would be to sacrifice resolution by restricting the number of bath sites and mix real- and imaginary time evolution as for example shown in Ref. [47]. None of these methods to deal with multi-orbital models is completely satisfactory. We would like to find an approach that allows us to use a large bath to represent the bath hybridization well and, at the same time, benefit from the potentially high resolution by performing real-time evolution. In this section we identified a possible problem in the standard super-site approach, namely a strong (and maybe artificial), increase in bond dimension with the number of orbitals. In the next section we will try to solve this problem by proposing a tensor network in which we explicitly try to not build these super-sites at all.

---

and hence, also need the same bond dimension.

6 Fork Tensor-Product States

In the previous section we identified a possible cause of why multi-orbital AIMs are very difficult to solve with MPS. The Hamiltonian of such an AIM, given in Eq. 2.10, does not directly couple bath sites of different orbitals. Conventional methods to solve them with MPS combine these bath sites to a super-site and suffer therefore from a fast growth of bond dimension with the number of orbitals. In this section we introduce a different approach in which the basic idea is to keep the bath degrees of freedom separated as much as possible. We propose a tensor network, whose geometry is a fork-like structure, shown for a two-orbital model in Fig. 16. For every orbital-spin combination we have a row of tensors. The leftmost tensor represents the impurity, while all other tensors incorporate the bath degrees of freedom. The rows are connected only at the impurity tensors, which makes the impurity tensors in the middle of rank 4, i.e.: they have three bond indices and one physical index. Written out, the tensor network in Fig. 16 represents states $|\psi\rangle$ as:

$$\begin{aligned}|\psi\rangle = \sum_{\{s\}\{i\}\{b\}} &\left(I^{s_1}_{i_1,b^1_{N_b}} B^{s_2}_{b^1_{N_b},b^1_{N_b-1}} \cdots B^{s_{N_b+1}}_{b^1_1} \right) \cdot \left(I^{s_{N_b+2}}_{i_1,i_2,b^2_{N_b}} B^{s_{N_b+3}}_{b^2_{N_b},b^2_{N_b-1}} \cdots B^{s_{2(N_b+1)}}_{b^2_1} \right) \\ &\left(I^{s_{2(N_b+1)+1}}_{i_2,i_3,b^3_{N_b}} B^{s_{2(N_b+1)+2}}_{b^3_{N_b},b^3_{N_b-1}} \cdots B^{s_{3(N_b+1)}}_{b^3_1} \right) \\ &\left(I^{s_{3(N_b+1)+1}}_{i_3,b^4_{N_b}} B^{s_{3(N_b+1)+2}}_{b^4_{N_b},b^4_{N_b-1}} \cdots B^{s_{4(N_b+1)}}_{b^4_1} \right) |s_1, s_2 \cdots s_{4(N_b+1)}\rangle \, . \end{aligned} \tag{6.1}$$

Above, we introduced different letters for impurity tensors (I) and bath tensors (B). Similarly, we label indices connecting two impurity tensors by a lower case i_m and bath indices by lower case b^m_j meaning that it is the index coupling the bath site j to bath site $j+1$ (impurity tensor if $j = N_b$) for orbital m. Note that the rightmost tensor has bath index $j = 1$ and the tensor coupling to the impurity has index $j = N_b$. Also note that the physical index in, e.g., $B^{s_{3(N_b+1)+2}}_{b^4_1,b^4_2}$ has a very long subscript $3(N_b+1)+2$. In the following we will often omit the subscript of the physical index for notational simplicity. Similarly we will often omit the orbital index m of b^m_j and just

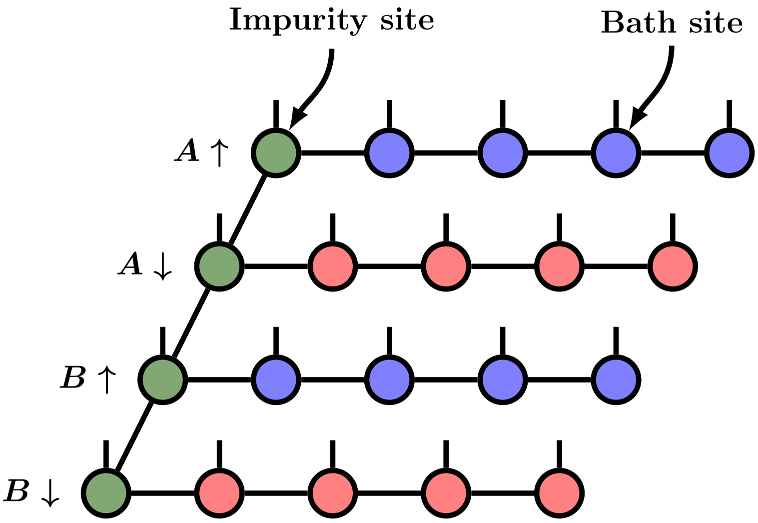

Figure 16: Graphical representation of an FTPS for a two-orbital AIM with orbitals A and B. For the numbering of sites, see Eq. 6.1. In the FTPS we try to avoid super-sites by separating the bath degrees of freedom. This is achieved by representing the bath for each orbital-spin combination using a chain of tensors similar to an MPS, but with an open link pointing towards its impurity tensor. The different orbitals are coupled only at the impurity tensors which introduces two rank four tensors ($A\downarrow$ and $B\uparrow$) in the middle. This tensor network geometry resembles the geometry of the Hamiltonian of an AIM, since also there the bath degrees of freedom for each orbital-spin combination are only coupled to its impurity. To add another orbital C, we would add two more bath chains (below orbital B). The impurity tensors $B\downarrow$ and $C\uparrow$ would have three bond indices, while the impurity $C\downarrow$ would have two.

write b_j or even only b, if it is distinctive. At this point, the reader should be convinced that the graphical representation (Fig. 16) is much more convenient than Eq. 6.1, overloaded with indices. We call such a tensor network Fork Tensor-Product State (FTPS). Similarly, we can define operators in this tensor geometry which we call Fork Tensor-Product Operators (FTPO). As before, the difference between FTPS and FTPO is that the latter has 2 physical indices corresponding the the bra- and ket-vector of the operator. In the following, we call the MPS-like chains representing the bath tensors the *arms* of the FTPS.

Before we continue, a word on related literature. A very similar tensor network was proposed by Holzner *et al.* [50] who used it for an NRG calculation for a two-orbital model. Every impurity tensor with three bond-indices can be interpreted as a *Y-junction* [101], where it has been shown how to perform DMRG. FTPS is also a special case of so called Tree Tensor Networks (TTN) [102–105]. Except for the idea of FTPS, which was inspired by the paper by Holzner *et al.* [50], all algorithms used for FTPS were developed independently by the author of the present thesis with AIMs in mind. Nevertheless, many similar algorithms can be found in related literature, see for example Ref. [104] for DMRG on a TTN or Ref. [102] for time evolution algorithms.

6.1 Schmidt Decomposition and Mixed Canonical Form

In Sec. 4 we emphasized that the algorithms (DMRG, tDMRG etc.) working on MPS can be employed as long as we can find a Schmidt decomposition for each bipartition defined by cutting a bond index. Here, we will show that for FTPS this is indeed possible. To find the Schmidt decomposition for MPS, we introduced left- and right-normalized tensors and defined the mixed canonical form that finally allowed us to obtain the Schmidt decomposition. For FTPS, the only major difference is that some of the impurity tensors have three bond indices. Hence, they also have three normalization properties which we call left-, down-, and up- normalization. We define them for the tensor $I^s_{i_m,i_{m+1},b}$ and denote $\bar{I}^s_{i_m,i_{m+1},b}$ for its complex conjugate:

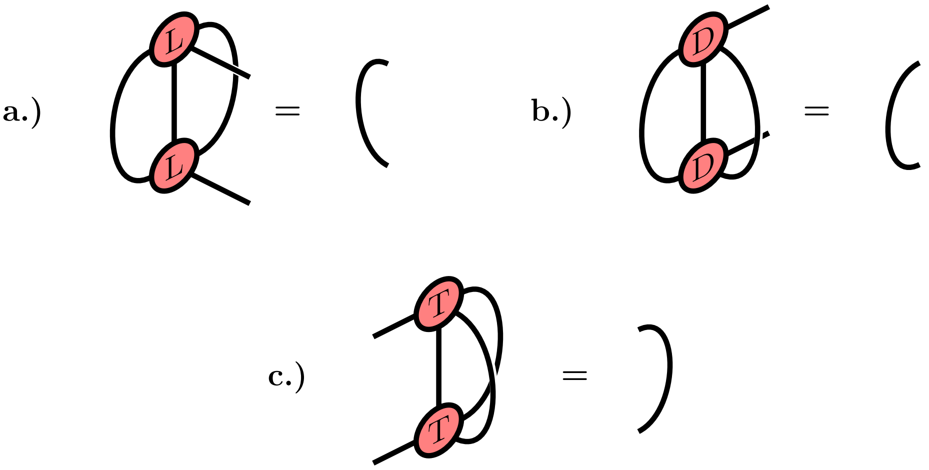

Figure 17: Graphical representation of all three normalization properties of impurity tensors. (a) left-normalized tensors L, (b) down-normalized tensors D and (c) up-normalized tensors T. The bath index points towards the bottom right, while the two impurity indices point top right and bottom left, similarly to Fig. 16.

- *left-normalization*: summation over the two impurity indices i_m and i_{m+1}, as well as the physical index s yields the identity with respect to the bath index (b) i.e.: $\sum_{s,i_m,i_{m+1}} I^s_{i_m,i_{m+1},b}\bar{I}^s_{i_m,i_{m+1},b'} = \delta_{b,b'}$. The graphical representation of this property is shown in Fig. 17 (a). We denote left-normalized tensors by L.

- *down-normalization*: summation over the impurity index pointing *downwards* (i_{m+1}), the bath index b as well as the physical index s yields the identity with respect to i_m i.e.: $\sum_{s,i_{m+1},b} I^s_{i_m,i_{m+1},b}\bar{I}^s_{i'_m,i_{m+1},b} = \delta_{i_m,i'_m}$. The graphical representation of this property is shown in Fig. 17 (b). We denote down-normalized tensors by D.

- *up-normalization*: summation over the impurity index pointing *upwards* (i_m), the bath index b as well as the physical index s yields the identity with respect to i_{m+1} i.e.: $\sum_{s,i_m,b} I^s_{i_m,i_{m+1},b}\bar{I}^s_{i_m,i'_{m+1},b} = \delta_{i_{m+1},i'_{m+1}}$. The graphical representation of this property is shown in Fig. 17 (c). We denote up-normalized tensors by T.

Note that a tensor can only be in one of these three normalizations at a time and that we can change between them using an SVD (see below). Also note that since the first (last) impurity tensor only has one impurity link it can only be down- (up-) and right-normalized. All tensors representing the bath have at most two bond indices and can therefore only be left- or right-normalized, similar to MPS tensors.

First, let us try to construct the mixed canonical form with the orthogonality center on a bath tensor of some arm m and bath index k. The process is depicted in Fig. 18 and involves three steps. We start from an FTPS with no orthogonality properties at all, shown in Fig. 18 (a). First, we completely right-normalize each arm $m' \neq m$, starting at the rightmost bath tensor (of rank two) and moving to the left, towards the impurity tensors. As with MPS tensors, we reshape $B^s_{b_i^{m'} b_{i-1}^{m'}}$ into a matrix $B_{(b_i^{m'}),(b_{i-1}^{m'} s)}$ and perform an SVD:

$$B_{(b_i),(b_{i-1}s)} = \sum_b U_{(b_i),(b)} S_{b,b} (V^\dagger)_{(b),(b_{i-1}s)}. \tag{6.2}$$

We multiply the matrices US onto the tensor to the left of the current site and keep $V^\dagger$ as the new FTPS tensor of the bath site. The orthogonality properties after these steps are shown in Fig. 18 (b). The right-normalization of $V^\dagger$ ensures that after the last bath tensor, we obtain an orthogonal basis for each arm m':

$$\begin{aligned} |u^{m'}_{b_{N_b}}\rangle &= \sum_{\{b_i\}\{s^{m'}\}} \left(B^s_{b_{N_b},b_{N_b-1}} \cdots B^s_{b_1} \right) |\{s^{m'}\}\rangle \\ \langle u^{m'}_{b_{N'_b}} | u^{m'}_{b_{N_b}} \rangle &= \delta_{(b_{N'_b}),(b_{N_b})}, \end{aligned} \tag{6.3}$$

where $\{s^{m'}\}$ is the set of all bath sites of arm m'. The graphical representation of $|u^{m'}_{b_{N_b}}\rangle$ for one arm is shown Fig. 19 (a).

Next, we up-normalize all impurity tensors for arms $m' < m$ starting at $m' = 1$. We achieve this by regrouping the physical index s, the bath index b, as well as the impurity index from above $i_{m'-1}$ (if it exists) into a single matrix index and the impurity index from below $i_{m'}$ into the other matrix

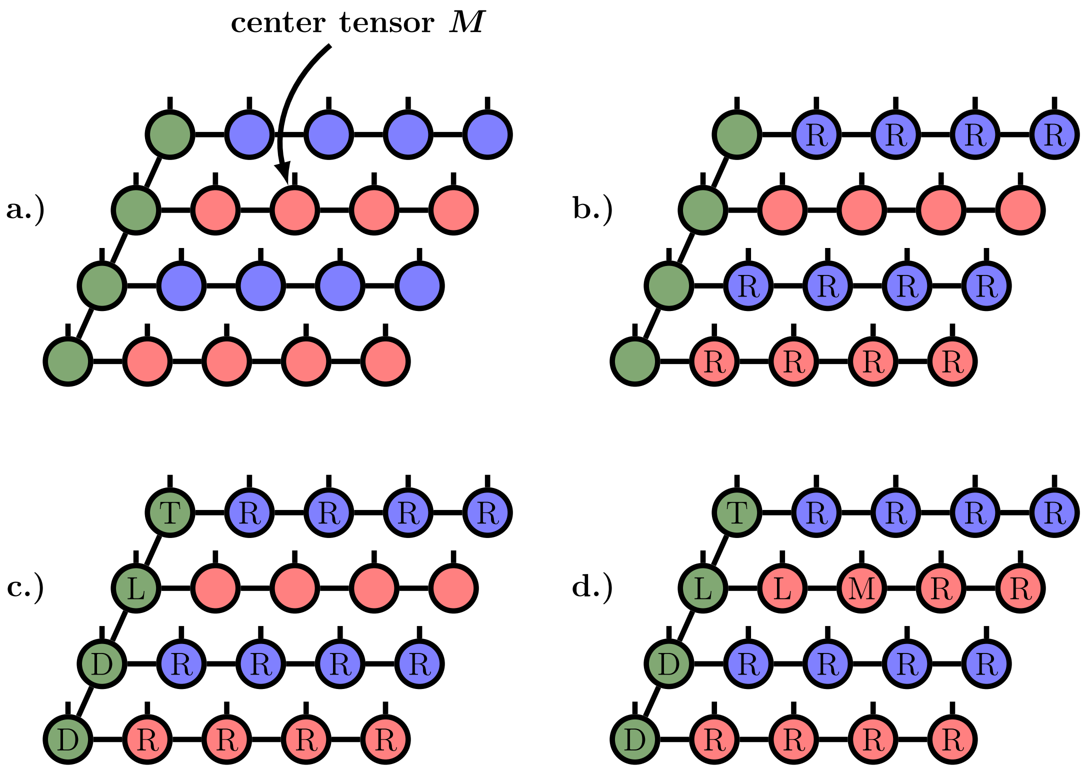

Figure 18: Construction of the mixed canonical form, starting from an FTPS with no orthogonality properties at all (a). The center tensor will be located at the second arm ($m = 2$) with bath index $k = 3$. First, we right-normalize all bath tensors for all arms $m' \neq m$, as shown in (b). Then, we down-normalize all impurity tensors below m, up-normalize the impurity tensors above m and left-normalize the impurity tensor at m, as shown in (c). Finally, we left-normalize all bath tensors with index $i > k$ and right-normalize all bath tensors $i < k$ on arm m (see Eq. 6.1 for numbering convention). The resulting state is shown in (d). A final SVD of center tensor M gives us the Schmidt decomposition on one of the two bonds of M, depending on which indices are the column- and row indices of the matrix. Since the singular values are the Schmidt values, we can truncate safely.

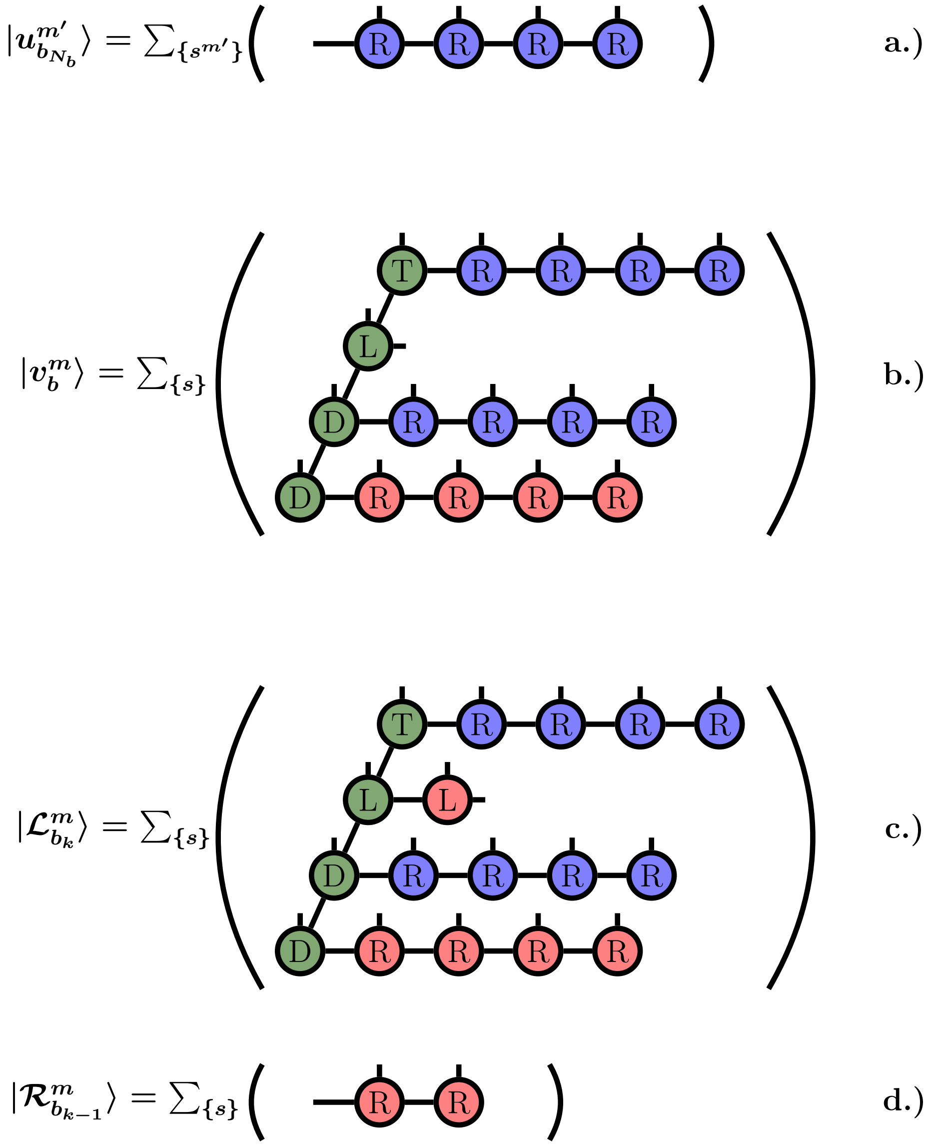

Figure 19: Graphical representation of (a) $|u^{m'}_{b_{N_b}}\rangle$ of a single arm, (b) $|v^m_b\rangle$, (c) left basis of orthogonality center $|\mathcal{L}_{b_k}\rangle$ and (d) right basis of orthogonality center $|\mathcal{R}_{b_{k-1}}\rangle$ (d). Summations run over every physical index present in each tensor network.

index and perform an SVD:

$$\begin{aligned} I^s_{i_{m'-1},i_{m'},b} &= I_{(i_{m'-1},b,s),(i_{m'})} = \sum_i U_{(i_{m'-1},b,s),(i)} S_{i,i} \left(V^\dagger\right)_{(i),(i_{m'})} , \\ \text{with } \left(U^\dagger U\right)_{i,i'} &= \sum_{s,i_{m'-1},b} \bar{U}_{(i),(i_{m'-1},b,s)} U_{(i_{m'-1},b,s),(i)} = \delta_{i,i'} . \end{aligned} \tag{6.4}$$

The second line above is exactly the up-normalization property defined before. Hence, we keep U as the new impurity tensor and multiply $SV^\dagger$ onto the impurity below, where we repeat these steps until we arrive at impurity m. Similarly, we down-normalize all impurity tensors $m' > m$ by using the impurity index from above as one matrix index and all other indices as the other matrix index i.e.: $I^s_{i_{m'-1},i_{m'},b} = I_{(i_{m'},b,s),(i_{m'-1})}$. Then, we left-normalize the impurity tensor of impurity m by reshaping $I^s_{i_{m'-1},i_{m'},b} = I_{(i_{m'},i_{m'-1}s),(b)}$, subsequent SVD and multiplication of $SV^\dagger$ onto the bath tensor of arm m connected to this impurity tensor. The orthogonality properties after these steps are shown in Fig. 18 (c). Again, we find an orthogonal basis, which now describes all arms $m' \neq m$ and all impurity degrees of freedom:

$$\begin{aligned} |v^m_b\rangle = \sum_{\{b\}\neq b^m_{N_b},\{s\}_I,\{i\}} & T^s_{i_1,b_1} \cdots L^s_{i_{m-1},i_m,b_m} \cdots D^s_{i_{N_{\text{orb}}},b_{N_{\text{orb}}}} \bigotimes_{m'\neq m} \left(|u^{m'}_{b_{N_b}}\rangle\right) |\{s\}_I\rangle , \\ & \text{with } \langle v^m_{b'}|v^m_b\rangle = \delta_{b,b'} . \end{aligned} \tag{6.5}$$

N_{orb} is the number of arms and $\{s\}_I$ are the impurity degrees of freedom. Using the graphical representation, $|v^m_b\rangle$ is shown Fig. 19 (b).

Finally, we only need to left-normalize all bath tensors on arm m with index $i > k$ and right-normalize all tensors for $i < k$. This gives us the mixed canonical form with the center tensor at arm m and bath index k, shown in Fig. 18 (d). This construction provides two orthogonal bases, one to the left and one to the right of the orthogonality center with tensor M:

$$|\mathcal{L}^m_{b_k}\rangle = \sum_{b_{N_b}\cdots b_{k+1}} L^s_{b_{N_b},b_{N_b-1}} \cdots L^s_{b_{k+1},b_k} \, |v^m_{b_{N_b}}\rangle \otimes |\{s\}_L\rangle$$

$$\text{with } \langle \mathcal{L}^m_{b'_k}|\mathcal{L}^m_{b_k}\rangle = \delta_{b'_k,b_k}.$$

$$|\mathcal{R}^m_{b_{k-1}}\rangle = \sum_{b_{k-2}\cdots b_1} R^s_{b_{k-1},b_{k-2}} \cdots R^s_{b_2,b_1} R^s_{b_1} \, |\{s\}_R\rangle$$

$$\text{with } \langle \mathcal{R}^m_{b'_{k-1}}|\mathcal{R}^m_{b'_{k-1}}\rangle = \delta_{b'_{k-1},b_{k-1}}.$$

$$|\psi\rangle = \sum_{b_k,b_{k-1},s} M^s_{b_k,b_{k-1}} \, |\mathcal{L}^m_{b_k}\rangle \, |s\rangle \, |\mathcal{R}^m_{b_{k-1}}\rangle \tag{6.6}$$

$|v^m_{b_{N_b}}\rangle$ is given in Eq. 6.5. $|\{s\}_L\rangle$ are the bath degrees of freedom of arm m to the left of site k and $|\{s\}_R\rangle$ those to the right. The graphical representation of the two bases is shown in Fig. 19 (c) and (d). From the mixed canonical form in Eq. 6.6, we can easily determine the Schmidt decomposition for any of the two bonds b_k and b_{k-1} by performing a last SVD of the center tensor M.

To obtain the mixed canonical form for an impurity tensor with index m, we perform similar steps. First, we right-normalize *all* arms. Then, we down-normalize all impurity tensors below and up-normalize all impurity tensors above (starting from the top (bottom) respectively). Again, a last SVD of center tensor M gives us the Schmidt decomposition. Depending on how we arrange the indices of $M^s_{i_{m-1},i_m,b}$ when reshaping it as a matrix, we obtain Schmidt decompositions separating different regions of the lattice. For example, if we SVD $M_{(i_{m-1},i_m,s),(b)}$, the separation is between all bath sites of arm m and all other sites (every impurity site as well as every bath $m' \neq m$).

With this, we have shown how to find the Schmidt decomposition for every FTPS bond. During time evolution or DMRG we will need to truncate the tensor network at some point to prevent unbounded growth of bond dimension. The Schmidt decomposition allows us to perform this truncation safely, since the Schmidt values correspond to the eigenvalues of the reduced density matrix [17].

As a final remark, we note that the crucial property of our tensor network which enables us to find the Schmidt decomposition is that its graph is loop-free (i.e.: there is only one unique way to get from any point A to any point B). Therefore, for each bond it is always possible to define some part of the lattice to be strictly to the left and the other strictly to the right allowing us to find the left- and right bases of the Schmidt decomposition.

6.2 DMRG

The approach of DMRG for FTPS is the same that we used for MPS: DMRG is a variational method on the space of FTPS. We view the tensor entries as variational parameters, and minimize with respect to one (two) tensor(s) at a time. For the single-site DMRG this results in (see Eq. 4.24):

$$\mathcal{L} = \langle\psi|\, H \,|\psi\rangle - \lambda\langle\psi|\psi\rangle$$

$$\frac{d\mathcal{L}}{dB^{s}_{b_{i-1},b_i}} \overset{!}{=} 0,$$

$$\Longrightarrow \sum_{s',b'_{i-1},b'_i} H^{\text{eff}}_{(s,b_{i-1},b_i),(s',b'_{i-1},b'_i)} B_{(s',b'_{i-1},b'_i)} = \lambda B_{(s,b_{i-1},b_i)}$$

$$\text{and} \qquad \frac{d\mathcal{L}}{dI^{s}_{i_{m-1},i_m,b_m}} \overset{!}{=} 0.$$

$$\Longrightarrow \sum_{s',i'_{m-1},i'_m,b'_m} H^{\text{eff}}_{(s,i_{m-1},i_m,b_m),(s',i'_{m-1},i'_m,b'_m)} I_{(s',i'_{m-1},i'_m,b_m)} = \lambda I_{(s,i_{m-1},i_m,b_m)} \tag{6.7}$$

The effective Hamiltonian H^{eff} is defined as a contraction of the tensor network of $\langle\psi|H|\psi\rangle$ with the optimized tensor from $\langle\psi|$ as well as $|\psi\rangle$ missing. Its graphical representation during the optimization of a bath tensor is shown in

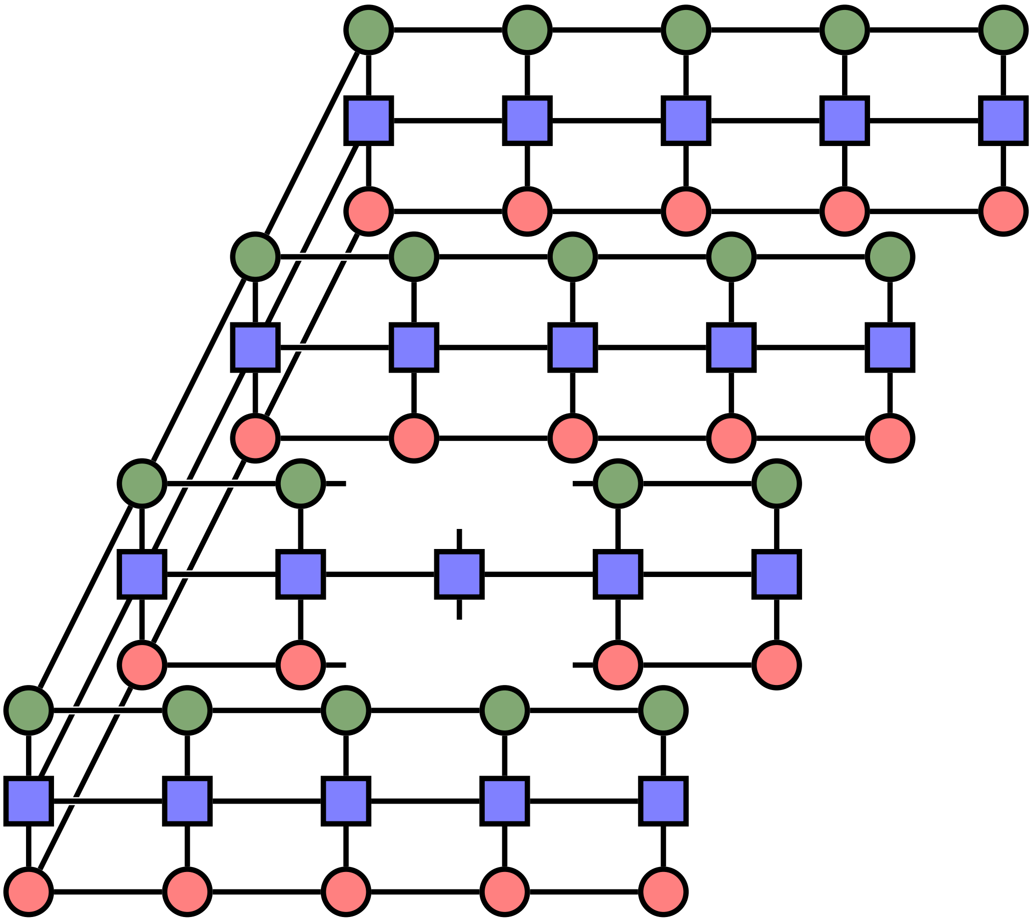

Figure 20: Graphical representation of the effective Hamiltonian H^{eff} for a single-site DMRG step for the tensor on arm $m = 3$ with index $k = 3$.

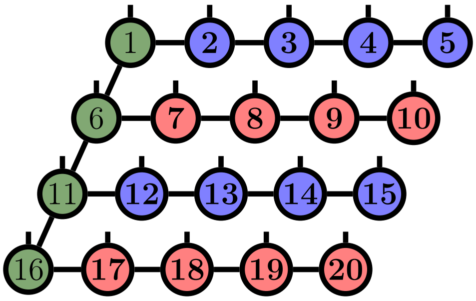

Figure 21: Fermionic order used in FTPS calculations. See also App. C (this is the same order as the physical indices in Eq. 6.1).

Fig. 20. We solve these eigenvalue equations using a sparse eigenvalue solver. To obtain the action of H^{eff} [15], we need the Hamiltonian of a multi-orbital AIM in FTPO-form. For the Kanamori interaction with the bath in star geometry, we show how to construct it in App. C. Furthermore, we need to decide on the fermionic order. It turns out that the most convenient order is the one depicted in Fig. 21 (see also Eq. C.1). After the optimization step on one site, we perform the next optimization on a neighboring tensor. For MPS this resulted in the right-left sweeps. Here, it is important to realize, that because DMRG is a variational method, the actual sweeping order in which we optimize the tensors is usually not important [16]. For the single-site DMRG we sweep through the tensor network the same way as presented below for the two-site approach.

As in standard DMRG, it is often better to minimize with respect to two neighboring tensors, since it allows to adjust the bond dimension during the DMRG simulation [17]. The resulting eigenvalue equations for such a two-site scheme are equivalent to Eq. 6.7. The only difference is that the effective Hamiltonian, as well as the optimized *vector* posses all indices of the two tensors that are optimized. We perform the two-site DMRG by repeating the following steps for each arm m (starting at $m = 1$) until convergence:

- Optimize the m-th impurity tensor and the bath site connected to it (for $m = 1$ sites 1 and 2 in Fig. 21).
- In a right-left sweep optimize the m-th bath by minimizing two neighboring bath tensors (for $m = 1$ the sweep consists of optimization steps for the sites $(2, 3)$, $(3, 4)$, $(4, 5)$, $(3, 4)$, $(2, 3)$ in Fig. 21).
- Optimize the m-th impurity tensor and the bath site connected to it a second time.
- If $m \neq N_{\text{orb}}$, optimize the m-th impurity tensor and and the $(m + 1)$-th impurity tensor (for $m = 1$: sites 1 and 6 in Fig. 21).

---

[15] Remember we never calculate H^{eff} directly [17].

[16] It might affect convergence though.

When performing a DMRG step on two impurity tensors, we optimize with respect to a rank six tensor possessing 2 physical indices and 4 bond indices (2 pointing towards the bath and one to the impurity above as well as below). After the optimization, we need to SVD this tensor which will be computationally very expensive. If we assume all bond indices to have bond dimension m, the SVD of such a rank six tensor would scale as $\mathcal{O}((dm^2)^3) = \mathcal{O}(d^3m^6)$. Hence, the optimization of two impurity tensors will be the bottleneck of the ground state search. Fortunately, in numerical practice it is very often the case that the bond dimension of the bath link is much smaller than the bond dimension of the impurity-impurity links, making the above m^6-scaling a bit less severe. For example, if we assume the impurity bonds to have bond dimension m and the bath indices to have bond dimension n, the SVD scales as $\mathcal{O}(dmn)^3$. While optimization of the impurity tensors will be very expensive, we expect the bath tensors to be much cheaper than in the super sites approach, since they will need only rather small tensor dimensions.

After two-site DMRG we often switch to the single-site approach which is much faster, since it does not show the m^6-scaling.

6.3 Time Evolution

Time evolution for multi-orbital AIMs with Kanamori interaction is very similar to time evolution for MPS. As in the single-orbital case (see Sec. 5), we first split off the interactions and time evolve the remaining terms coupling the baths to the impurities using swap-gates. For the Kanamori interaction (Eq. 2.11), we need to be careful with the fermionic sign, since the spin-flip and pair-hopping terms locally change the occupation of the impurity. This in turn affects the bath, since in the fermionic order the bath tensors are in between impurity tensors (see Fig. 21). Therefore, we decompose the time evolution operator $e^{-i\Delta t H}$ into:

$$e^{-i\Delta t H} \approx \left(\prod_{m'>m} e^{-i\frac{\Delta t}{2} H^{\text{SF-PH}}_{m,m'}} \right) \cdot e^{-i\frac{\Delta t}{2} H_{\text{DD}}} \cdot \\ \times e^{-i\Delta t \sum_{k\sigma m} H_{k\sigma m}} \cdot e^{-i\frac{\Delta t}{2} H_{\text{DD}}} \cdot \left(\prod_{m'>m} e^{-i\frac{\Delta t}{2} H^{\text{SF-PH}}_{m,m'}} \right). \tag{6.8}$$

The terms $\sum_{k\sigma m} H_{k\sigma m}$ connecting bath and impurity, factor into a product over every orbital-spin combination without any additional approximation. As already mentioned, we time evolve these terms in star geometry using swap gates, shown in Sec. 5.2.

To time evolve the density-density interactions, we directly construct the FTPO of $e^{-i\frac{\Delta t}{2} H_{\text{DD}}}$ and apply it. Since H_{DD} does not change the particle number, its action onto the bath tensors is trivial and we only need to construct the $4^{N_{orb}} \times 4^{N_{orb}}$ matrix of H_{DD} which we then exponentiate. This is possible even for a 5-band model, since the size of the matrix stays manageable (1024×1024). Using repeated SVDs on this matrix, we finally obtain the FTPO of the time evolution operator.

To time evolve the spin-flip and pair-hopping terms this strategy does not work, because of the fermionic sign already mentioned. Both, the spin-flip as well as the pair hopping operator (for example the spin-flip operator is given by $c^\dagger_{m0\uparrow} c_{m0\downarrow} c_{m'0\uparrow} c^\dagger_{m'0\downarrow} + h.c.$), individually have the property $A^3 = A$. For such operators we can simplify the exponential using its series expansion as we have shown in [1]:

$$e^{-i\Delta t J A} = I + A^2 \big(\cos(\Delta t J) - 1 \big) - i A \sin(\Delta t J). \tag{6.9}$$

The right hand side of Eq. 6.9 can be written in FTPO form, since we know how to incorporate the fermionic sign for A as well as for A^2. The construction of this operator is given in App. D.

Now, we only need to apply all operators and gates in the correct order to time evolve by one time-step Δt.

With this, we are capable of calculating the Green's functions of a multi-orbital AIM. The general strategy is outlined in Sec. 4.8. In the following two sections we will show the capabilities of FTPS used as a solver for DMFT for real-material calculations.

7 Fork Tensor-Product States: Efficient Multi-orbital Real-Time DMFT Solver (*Phys. Rev. X 7, 031013)*

In this section I present the results published in Ref. [1], which is one of the main publications of the author. The author implemented the FTPS impurity solver, performed all FTPS calculations and was the main contributor in writing the publication. Manuel Zingl performed the DFT calculation and implemented the DMFT self consistency on the real frequency axis within the TRIQS library (v1.4) [106]. Furthermore, he performed the CTQMC calculations that were used to compare our results with, and helped in writing the paper. Robert Triebl performed the analytic continuation of the imaginary time Green's functions and also played an important role in interpreting the results and writing the paper. Since this section is a direct copy of Ref. [1] (Phys. Rev. X 7, 031013), it will repeat some of the basics of the theory already discussed in the previous sections.

In this publication we used the FTPS solver for the typical benchmark compound $SrVO_3$. As low energy subspace we use the three t_{2g} bands i.e.: we employ a three-orbital model in DMFT. Our major insight was that the real-time (real-frequency) approach of FTPS allows to resolve a multiplet structure in the spirit of the atomic excitations discussed in Sec. 2.1. We also show that such a multiplet structure cannot be found with CTQMC, since the ill-posed analytic continuation cannot resolve it, especially if the imaginary time Green's function is subject to statistical noise. Finally, we show that the FTPS solver can be applied for 5-orbital models as well.

The paper is included in its entirety in the following. To obtain a single, coherent bibliography for the present thesis the citations are merged into one list of references at the end of the thesis.

7.1 Abstract

We present a tensor network especially suited for multi-orbital Anderson impurity models and as an impurity solver for multi-orbital dynamical mean-field theory (DMFT). The solver works directly on the real-frequency axis and yields high spectral resolution at all frequencies. We use a large number ($\mathcal{O}(100)$) of bath sites, and therefore achieve an accurate representation of the bath. The solver can treat full rotationally-invariant interactions with reasonable numerical effort. We show the efficiency and accuracy of the method by a benchmark for the three-orbital testbed material $SrVO_3$. There we observe multiplet structures in the high-energy spectrum which are almost impossible to resolve by other multi-orbital methods. The resulting structure of the Hubbard bands can be described as a broadened atomic spectrum with rescaled interaction parameters. Additional features emerge when U is increased. Finally we show that our solver can be applied even to models with five orbitals. This impurity solver offers a new route to the calculation of precise real-frequency spectral functions of correlated materials.

7.2 Introduction

Strongly correlated systems are among the most fascinating objects solid-state physics has to offer. The interactions between constituents of such systems lead to emergent phenomena that cannot be deduced from the properties of non-interacting particles [107].

One of the most widely used methods to describe strongly-correlated electrons is the dynamical mean-field theory (DMFT) [9, 63]. DMFT treats local electronic correlations by a self-consistent mapping of the lattice problem onto an effective Anderson impurity model (AIM). Calculating the single particle spectral function of this impurity model in an accurate and efficient way is at the heart of every DMFT calculation. To this end, many numerical methods have been developed or adapted. These are based for instance on continuous-time quantum Monte Carlo (CTQMC) [14, 15], exact diagonalization (ED) [25–27], the numerical renormalization group (NRG) [19, 20], configuration interaction (CI) based solver [28, 29], and also the density-matrix renormalization group (DMRG) with matrix-product states (MPS) [16, 17].

Every algorithm has strengths and weaknesses: CTQMC is exact apart from statistical errors on the imaginary axis and can deal with multiple orbitals, but it is in some cases plagued by the fermionic sign problem. Additionally, an ill-posed analytic continuation is necessary to obtain real-frequency spectra, which therefore become broadened, especially at high energies. ED directly provides spectra on the real axis, but it is severely limited in the size of the Hilbert space, i.e. in the number of bath sites. Quite recently, NRG was shown to be a viable three-band solver by exploiting non-abelian quantum number conservation [32–34]. NRG works on the real axis and captures the low-energy physics well, but it has by construction a poor resolution at higher energies. Another interesting route that has been proposed recently are solvers that tackle the problem of exponential growth of the Hilbert space using ideas from quantum chemistry, i.e. the configuration interaction [28, 29]. They allow to go beyond the small bath sizes of ED, keeping all the advantages such as absence of fermionic sign problems. However, in multi-orbital applications (see Appendix of Ref. [29]), the spectral resolution has so far been restricted by the restricted number of bath sites ($\mathcal{O}(20)$).

MPS based techniques like DMRG, finally, do not suffer from a sign problem and can be used on the real- as well as on the imaginary-frequency axis. The price to pay for the absence of the sign problem is an, in general, very large growth of bond dimension with the number of orbitals.

Dynamical properties and spectral functions can be calculated within DMRG and have been used for impurity solvers, e.g. with the Lanczos-like continued-fraction expansion [41, 108]. Other solvers using the more stable correction vector [109] and dynamical DMRG (DDMRG) [110] methods were developed [42–45]. Both algorithms produce very accurate spectral functions, but have the disadvantage that a separate calculation for each frequency has to be performed. The Chebyshev expansion [111] with MPS [112], supplemented by linear prediction [98], was used for impurity solvers in the single band case [46] and for two bands [48]. Recently, some of us introduced a method based on real-time evolution [89, 113–115] and achieved a self consistent DMFT solution for a two-band model [24]. In such calculations, the physical orbitals for each spin direction are usually combined to one large site in the MPS. Three or more orbitals have not been feasible with this approach, because of a large increase in computational cost with the number of orbitals. Another MPS-based solver, which works on the imaginary axis, was recently introduced [47] and it was applied as a solver for three bands in two-site cluster DMFT. It was supplemented by a single real-time evolution to compute the spectral function, avoiding the analytic continuation. However, this method is restricted by the number of bath sites which can be employed. In the calculation mentioned, only three bath sites per orbital were used, limiting the energy resolution for real-frequency spectral functions.

In the present paper, we introduce a novel impurity solver which works directly on the real-frequency axis. To this end, we use a tensor network that captures the geometry of the interactions in the Anderson model better than a standard MPS. Our approach is to some extent inspired by the work of Ref. [50], which used a similar network for a two orbital NRG ground state calculation. We are not restricted to a small number of bath sites. This is imperative for exploiting the spectral resolution achievable with real-time calculations. We emphasize that (i) our method is by construction free of any fermionic sign problem, (ii) one can fully converge the DMFT self-consistency loop on the real-frequency axis and (iii) we can achieve an almost exact representation of the bath spectral function. We apply this method to multi-orbital DMFT for the testbed material $SrVO_3$ and show that one can resolve a multiplet structure in the Hubbard bands, keeping at the same time a good description of the low-energy quasi-particle excitations.

The paper is structured as follows. First we show how impurity solvers with tensor networks work in general and introduce our new tensor network approach which we call fork tensor-product states (FTPS) (Sec. 7.3). Next we explain in detail how our solver is used in the context of multi-orbital DMFT (Sec. 7.4). In Sec. 7.5, we apply our approach to $SrVO_3$ and discuss the multiplet structure that the FTPS solver allows to resolve. In order to check the accuracy of the method, we also compare the FTPS results to CTQMC for $SrVO_3$. Finally, we show the efficiency of the FTPS solver by applying it to a five-orbital model.

7.3 Tensor Network Impurity Solvers

The Anderson impurity model (AIM) describes an impurity (with Hamiltonian H_{loc}) coupled to a bath of non-interacting fermions hybridized with it. A typical AIM Hamiltonian is given by:

$$\begin{aligned}
H &= H_{\text{loc}} + H_{\text{bath}} \qquad (7.1)\\
H_{\text{loc}} &= \epsilon_0 \sum_{m\sigma} n_{m0\sigma} + H_{\text{DD}} + H_{\text{SF-PH}}\\
H_{\text{DD}} &= U \sum_{m} n_{m0\uparrow} n_{m0\downarrow}\\
&\quad + (U-2J) \sum_{m'>m,\sigma} n_{m0\sigma} n_{m'0\bar{\sigma}}\\
&\quad + (U-3J) \sum_{m'>m,\sigma} n_{m0\sigma} n_{m'0\sigma}\\
H_{\text{SF-PH}} &= J \sum_{m'>m} \left(c^{\dagger}_{m0\uparrow} c_{m0\downarrow} c_{m'0\uparrow} c^{\dagger}_{m'0\downarrow} + \text{h.c.} \right)\\
&\quad - J \sum_{m'>m} \left(c^{\dagger}_{m0\uparrow} c^{\dagger}_{m0\downarrow} c_{m'0\uparrow} c_{m'0\downarrow} + \text{h.c.} \right)\\
H_{\text{bath}} &= \sum_{ml\sigma} \epsilon_l n_{ml\sigma} + V_l \left(c^{\dagger}_{m0\sigma} c_{ml\sigma} + \text{h.c.} \right),
\end{aligned}$$

where $c^{\dagger}_{ml\sigma}$ ($c_{ml\sigma}$) creates (annihilates) an electron in band m ($m \in \{1,2,3\}$ for a three-orbital model) with spin σ at the l-th site of the system (the impurity has index $l=0$, the bath degrees of freedom have $l \geq 1$), and $n_{ml\sigma}$ are the corresponding particle number operators. H_{DD} describes density-density (DD) interactions between all orbitals and $H_{\text{SF-PH}}$ are the spin-flip and pair-hopping terms. This three-orbital Hamiltonian is not only important in the context of real-material calculations. It has also been studied extensively on the model level, most importantly because it hosts unconventional correlation phenomena. For a selection of recent work, see for instance Refs. [23, 32, 116–118]

An impurity solver calculates the retarded impurity Green's function $G(t)$

$$G(t) = -i\theta(t) \langle\psi_0| [c^\dagger(t), c(0)] |\psi_0\rangle \tag{7.2}$$

of the interacting problem (7.1), either in real or imaginary time t. In the present paper, we introduce a new tensor network similar to an MPS, which can be used as a real-time impurity solver for three orbitals. We first introduce MPS before moving on to what we call fork tensor-product states (FTPS) in Sec. 7.3.2.

7.3.1 Matrix Product States (MPS) and DMRG

MPS are a powerful tool to efficiently encode quantum mechanical states. Consider a state $|\psi\rangle$ of a system consisting of N sites:

$$|\psi\rangle = \sum_{s_1,s_2,\cdots,s_N} c_{s_1,\cdots,s_N} |s_1, s_2, \cdots, s_N\rangle . \tag{7.3}$$

Each site i has a local Hilbert space of dimension d_i spanned by the states $|s_i\rangle$. Through repeated use of singular-value decompositions (SVDs), it is possible to factorize every coefficient $c_{s_1,\cdots,s_N}$ into a product of matrices [17], i.e. into an MPS,

$$|\psi\rangle = \sum_{s_1,s_2,\cdots,s_N} A_1^{s_1} \cdot A_2^{s_2} \cdots A_N^{s_N} |s_1, s_2, \cdots, s_N\rangle . \tag{7.4}$$

Each $A_i^{s_i}$ is a rank-3 tensor, except the first and last ones ($A_1^{s_1}$, $A_N^{s_N}$), which are of rank two. The index s_i is called physical index, and the *matrix* indices, which are summed over, are the so called bond indices. A general state of the full Hilbert space is unfeasible to store, but it can be shown that ground states are well described by an MPS with limited bond dimension m (dimension of the bond index) [119].

In complete analogy to the states, one can factorize an operator into what

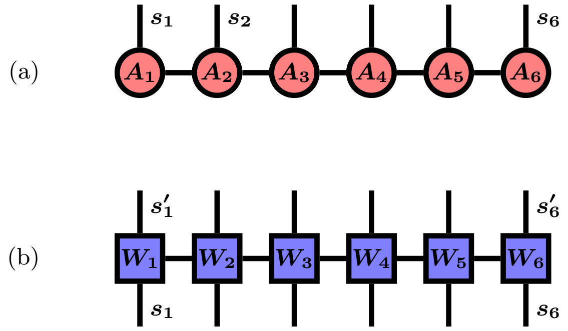

Figure 22: (a) Graphical representation of an MPS. Every circle corresponds to a tensor $A_i^{s_i}$ and each line to an index of this tensor. In this picture, the physical indices are the vertical lines, while the horizontal lines show the bond indices. Connected lines mean that the corresponding index is summed over. Fixing all the physical indices s_i for each site results in a tensor of rank zero with the value of the coefficient $c_{s_1,\cdots,s_N}$.
(b) Graphical representation of an MPO. The difference to an MPS is that an MPO has incoming indices s_i and outgoing indices s'_i corresponding to the bra- and ket vectors of the operator.

is called a matrix-product operator (MPO) [17],

$$H = \sum_{\substack{s_1,\cdots,s_N \\ s'_1,\cdots,s'_N}} W_1^{s_1,s'_1} \cdots W_N^{s_N,s'_N} \left|s'_1,\cdots,s'_N\right\rangle \left\langle s_1,\cdots,s_N\right| , \tag{7.5}$$

where each $W_i^{s_i,s'_i}$ is a rank-4 tensor. Tensor networks in general have a very useful graphical representation, which is shown for an MPS and an MPO in Fig. 22. Note that when we use the term MPS we always mean a one-dimensional chain of tensors as shown in Fig. 22.

To calculate Green's functions within the MPS formalism, one usually first applies the DMRG [16, 17], which acts on the space of MPS and finds a variational ground state $|\psi_0\rangle$ and ground-state energy E_0. It minimizes the expectation value

$$E_0 = \min_{|\psi\rangle} \frac{\langle\psi|H|\psi\rangle}{\langle\psi|\psi\rangle} \tag{7.6}$$

by updating usually two neighboring MPS tensors before moving on to the next bond. This procedure also yields the Schmidt decomposition of the state at the current bond on the fly. The DMRG approximation is to keep only those states with the largest Schmidt coefficient. It is important to note that one can perform a DMRG calculation for any tensor network, as long as one can generate a Schmidt decomposition [104].

For obtaining the Green's function, we employ an evolution in real time. Eq. (7.2) is split into the greater $G^>$ and lesser Green's function $G^<$:

$$\begin{aligned} G(t) &= -i\Theta(t)\Big(G^>(t) + G^<(t)\Big) \\ G^>(t) &= \langle\psi_0|ce^{-iHt}c^\dagger|\psi_0\rangle\, e^{iE_0t} \\ G^<(t) &= \langle\psi_0|c^\dagger e^{iHt}c|\psi_0\rangle\, e^{-iE_0t}, \end{aligned} \tag{7.7}$$

which are calculated in two separate time evolutions. This is done by first applying $c^\dagger$ (or c) and then time evolving this state and calculating the overlap with the state at time $t = 0$. The time evolution is the most computationally expensive part, since time evolved states are not ground states anymore, and the needed bond dimensions usually grow very fast with time.

7.3.2 Fork Tensor Product States (FTPS)

So far, the usual way of dealing with Hamiltonians like Eq. (7.1) using MPS [24, 46, 48] has been to place the impurity in the middle of the system and the up- and down-spin degrees of freedom to its left and right, resp. The local state space of each bath site then consists of M spinless-fermion degrees of freedom, with dimension 2^M, where M is the number of orbitals in the Hamiltonian Eq. (7.1). This exponential growth is usually accompanied by a very fast growth in bond dimension when using the above arrangement. We did indeed encounter this very fast growth upon calculating the ground state of some one- two- and three-orbital test cases.

For treatment by MPS, the general Hamiltonian Eq. (7.1) with hopping terms from the impurity to each bath site is usually transformed into a Wilson chain with nearest-neighbor hoppings only, i.e. of the form $t_i(c_i^\dagger c_{i+1} + \text{h.c.})$ [20]. This was thought to be necessary since long-range interactions look problematic for MPS-based algorithms. Quite recently, though, it was

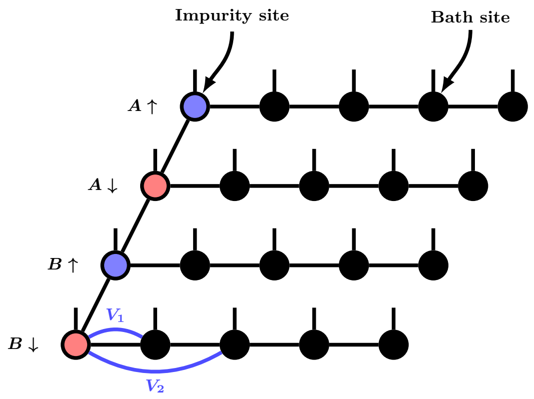

Figure 23: Graphical representation of a fork tensor product state (FTPS) for multi-orbital AIM. The idea to separate bath degrees of freedom leads to a fork-like structure. In this picture, a two-orbital model with four bath sites each is shown. Orbitals are labeled A and B and the arrows denote the spin. Each spin-orbital combination has its *own* bath sticking out to the right. As in Fig. 22, the vertical lines are the physical degrees of freedom (all of dimension two, for empty, resp. occupied bath sites). All other lines are bond indices and like in the MPS they are summed over. As mentioned in the text, the bath is represented in star geometry due to the smaller bond dimensions needed. The bath sites are ordered according to their on-site energies. Two example hoppings V_1 and V_2 are drawn.

discovered that MPS can deal with the original form of H_{bath} in Eq. (7.1) better [49]. Because all hopping terms in H_{bath} originate from the impurity, this is called the *star* geometry. The reason for the better performance is that in the star geometry one has many nearly fully occupied (empty) bath sites with very low (high) on-site energies ϵ_l.

Since basis states with many unoccupied low-energy sites have a very low Schmidt coefficient, these states are discarded from the MPS. The same holds for occupied high energy sites. However, when dealing with multi-orbital models, the star geometry is not enough to be able to calculate Green's functions using MPS. The growth of the bond dimensions still makes those calculations unfeasible.

The key idea of the present work is to construct a tensor network which is beyond a standard MPS, but similar enough to be able to use established methods like DMRG and time evolution. From Hamiltonian (7.1) one can immediately notice that there are no terms coupling bath sites of different orbitals. Hence, it might not be advantageous to combine those, not directly interacting, degrees of freedom into one large physical index in the MPS.

Our proposed tensor network, therefore, separates the bath degrees of freedom as much as possible. It consists of separate tensors for every orbital-spin combination, each connected to bath tensors as shown in Fig. 23. This tensor network is no MPS anymore, since there are some tensors (labeled $A\downarrow$ and $B\uparrow$ in the example of Fig. 23) that have three bond indices and one physical index, i.e. which are of rank 4. Cutting any bond splits the network into two separate parts. Therefore, one can calculate the Schmidt decomposition in a way very similar to an MPS, which means that also DMRG is possible. The main bottleneck of calculations with FTPS is to perform SVDs of the rank-4 tensors representing the impurities. When all bond indices have the same dimension χ, it is necessary to do a SVD for a $\chi^2 d \times \chi$ matrix with computational complexity $\mathcal{O}(\chi^4 d)$. However, as we show below, this operation does not pose a substantial problem for calculations using FTPS. Since the impurity tensors pose the biggest challenge, our tensor network would likely also allow us to deal with the chain geometry without a drastic increase in computational cost. In the present paper we will only

use FTPS with baths in star geometry.
The proposed FTPS are similar to the tensor network used by Holzner *et al.* [50] to perform NRG calculations for ground state properties of an AIM with two orbitals.

The three-legged tensors in our network (Fig. 23) can also be interpreted as two coupled junctions with three legs in the language of Ref. [101], where it has been shown that DMRG is possible on such junctions. Furthermore, our approach has similarities with the so called Tree Tensor Networks (TTN) [102–105].

Time Evolution

Time evolution with the Hamiltonian Eq. (7.1) is not straightforward, since it features long-range hoppings. Possible methods include Krylov approaches [120], the time-dependent variational principle [83, 121] and the series expansion of e^{iHt} proposed by Zaletel *et al.* [86]. In this work, however, we use a much simpler approach.

First, we split the Hamiltonian into the following terms: (i) the spin-flip and pair-hopping terms $H^{\text{SF-PH}}_{m,m'}$ for each orbital combination, with $\sum_{m'>m} H^{\text{SF-PH}}_{m,m'} = H_{\text{SF-PH}}$ (see Eq. (7.1)), (ii) the density-density interaction terms H_{DD}, and (iii) all other terms $H_{\text{free}} = H_{\text{bath}} + \epsilon_0 \sum_{m\sigma} n_{m0\sigma}$. With these terms, we write the time-evolution operator for a small time step Δt using a second-order Suzuki-Trotter decomposition [91],

$$\begin{aligned} e^{-i\Delta t H} \approx & \left(\prod_{m'>m} e^{-i\frac{\Delta t}{2} H^{\text{SF-PH}}_{m,m'}} \right) \cdot e^{-i\frac{\Delta t}{2} H_{\text{DD}}} \cdot \\ & \times e^{-i\Delta t H_{\text{free}}} \cdot e^{-i\frac{\Delta t}{2} H_{\text{DD}}} \cdot \left(\prod_{m'>m} e^{-i\frac{\Delta t}{2} H^{\text{SF-PH}}_{m,m'}} \right) . \end{aligned} \tag{7.8}$$

Note that in this decomposition, the order of the spin-flip and pair-hopping terms is important. The order of operators in the second product must be opposite to the one in the first.

We see that Eq. (7.8) involves three different operators $H^{\text{SF-PH}}_{m,m'}$, H_{DD} and H_{free}, each of which will be treated differently.

Time evolution of the density-density interactions is performed with an MPO-like representation of the time-evolution operator $e^{-i\frac{\Delta t}{2}H_{\rm DD}}$. For a three-orbital model, first the full matrix $(4^3 \times 4^3)$ of $e^{-i\frac{\Delta t}{2}H_{DD}}$ is created, which is then decomposed into MPO-form by repeated SVDs. Since $H_{\rm DD}$ only consists of density-density interactions, no fermionic sign appears in $e^{-i\Delta t H_{\rm DD}}$.

Time evolution of the spin-flip and pair-hopping terms is more involved than the density-density interactions, since the operators change the particle numbers on the impurity sites. Therefore, it can be difficult to deal with the fermionic sign of the time evolution operator when the impurities are not next to each other in the fermionic order. It turns out that the spin-flip and the pair-hopping terms have the property $\hat{A}^3 = \hat{A}$ individually, with $\hat{A}$ being either the spin-flip or the pair-hopping operator, resp. Furthermore they commute with each other allowing us to separate them without Trotter error. The time-evolution operator of $J\hat{A}$ is then given by:

$$e^{-i\Delta t J\hat{A}} = I + \hat{A}^2\big(\cos(\Delta t J) - 1\big) - i\hat{A}\sin(\Delta t J)\,. \tag{7.9}$$

For this operator, an MPO can be found for which the fermionic sign can easily be determined[17].

To time evolve the bath terms we use an iterative second-order Suzuki-Trotter breakup for *each* term in $H_{\rm free}$. Neglecting orbital (m) and spin (σ) indices, the first step in this breakup is the following: $e^{-i\Delta t\sum_{l=1}^{N_b} H_l} \approx e^{-i\frac{\Delta t}{2}H_1} \cdot e^{-i\Delta t\sum_{l=2}^{N_b} H_l} \cdot e^{-i\frac{\Delta t}{2}H_1}$. Next we split off H_2 and iterate this procedure until we end up with

$$e^{-i\Delta t H_{\rm free}} \approx \prod_{m\sigma}\left[\left(\prod_{l=1}^{N_b-1} e^{-i\frac{\Delta t}{2}H_{ml\sigma}}\right) \cdot e^{-i\Delta t H_{mN_b\sigma}} \cdot \left(\prod_{l=N_b-1}^{1} e^{-i\frac{\Delta t}{2}H_{ml\sigma}}\right)\right], \tag{7.10}$$

---

[17] Note that we use the term MPO a bit loosely here. What we mean is an operator factorized in the same fork-like structure as the state in Fig. 23.

with N_b the number of bath sites and $H_{ml\sigma} = \epsilon_l n_{ml\sigma} + V_l \left(c^\dagger_{m0\sigma} c_{ml\sigma} + \text{h.c.} \right)$. In the above equation, we neglected the term $\epsilon_0 n_{m0\sigma}$ that we add to $H_{m1\sigma}$. Eq. (7.10) is a product of two-site gates (an operator acting non-trivially only on two sites) with one of the two sites always being the impurity. This means that those two sites are not nearest neighbors in the tensor network. To overcome this problem, we use so called swap gates [17, 90]. The two-site operator

$$S_{ij} = \delta_{s_i, s'_j} \delta_{s_j, s'_i} \cdot (-1)^{n_i n_j} \tag{7.11}$$

swaps the state of site i (s_i with occupation n_i) with the state of site j (s_j with occupation n_j). The factor $(-1)^{n_i n_j}$ gives the correct fermionic sign and is negative if an odd number of particles on site i gets swapped with an odd number of particles on site j. To be more precise, the matrix representation of the swap gates used in this work is:

$$S_{ij} = |00\rangle \langle 00| + |10\rangle \langle 01| + |01\rangle \langle 10| - |11\rangle \langle 11| \,. \tag{7.12}$$

It turns out that every swap gate can be combined with an actual time evolution gate without additional computational time. For example, the first step in this time evolution would be to apply $e^{-i\frac{\Delta t}{2} H_{m1\sigma}}$. Immediately afterwards, even before the SVD (to separate the tensors again), the swap gate is applied so that the impurity and the first bath sites are swapped. By repeating this process one moves the impurity along its horizontal arm in Fig. 23. Because a second-order decomposition is used, now all time evolution gates except the one at site N_b have to be applied again. But now, the impurity and bath site needs to be swapped *before* time evolution.

Note that the algorithm presented above cannot only be used to perform real-time evolutions, but it is applicable also to evolution in imaginary time simply by replacing idt by $d\tau$.

7.4 Multi orbital DMFT with FTPS

In this section we present details of our impurity solver.

We refer to Refs. [11, 63] for DMFT in general, and to Refs. [13, 122] for DMFT in the context of realistic ab-initio calculations for correlated materials.

In the latter approach, called density-functional theory (DFT)+DMFT, the correlated subspace is described by a Hubbard-like Hamiltonian. Within DMFT, this model is mapped onto the AIM Hamiltonian (7.1). This mapping defines the bath hybridization function $\Delta(\omega)$ describing the influence of the surrounding electrons.

Since FTPS provide the Green's function of the AIM on the real-frequency axis, also the self-consistency loop is performed directly for real frequencies. For calculating the bath hybridization, we use retarded Green's functions with a finite broadening η_{SC} in order to avoid numerical difficulties with the poles of the Green's function. Throughout this work, we use $\eta_{SC} = 0.005\,\mathrm{eV}$[18].

The impurity solver calculates the self energy $\Sigma(\omega)$ of the AIM, given the bath hybridization function $\Delta(\omega)$ and the interaction Hamiltonian on the impurity. To this end, our solver performs the following steps, which are explained in more detail in the text below:

1. Obtain bath parameters ϵ_l and V_l by a deterministic approach based on integration of the bath hybridization function $\Delta(\omega)$.

2. Calculate the ground state $|\psi_0\rangle$ and ground-state energy E_0 of the interacting problem.

3. Apply impurity creation or annihilation operators, and time evolve these states to determine the interacting Green's function (Eq. (7.2)).

4. Fourier transform Eq. (7.2) to obtain $G(\omega)$ and calculate the local self-energy,

$$\Sigma(\omega) = G_0(\omega)^{-1} - G(\omega)^{-1}. \tag{7.13}$$

---

[18] For stability reasons, a larger broadening of $\eta_{SC} = 0.01\,\mathrm{eV}$ was used in the first two DMFT-cycles.

To perform step 1 we use

$$\begin{aligned} V_l^2 &= \int_{I_l} \left[-\frac{1}{\pi} \operatorname{Im} \Delta(\omega) \right] d\omega \\ \epsilon_l &= \frac{1}{V_l^2} \int_{I_l} \omega \left[-\frac{1}{\pi} \operatorname{Im} \Delta(\omega) \right] d\omega, \end{aligned} \tag{7.14}$$

similar to Refs. [20] (NRG) and [49]. Each interval I_l corresponds to a bath site. This discretization can be interpreted as representing each interval I_l as a delta peak at position ϵ_l and weight V_l^2. Sum rules for such discretization parameters can be found analytically [123]. In this work we choose the length of each interval such that the area of the bath spectral function $-\frac{1}{\pi}\operatorname{Im}\Delta(\omega)$ is approximately constant for each interval [124]. For the case at hand, this discretization was found to be numerically more stable than using intervals of constant length. Unless stated otherwise, we use $N_b = 109$ bath sites per orbital and spin. We note that this scheme is not restricted to diagonal hybridizations. In the general case of off-diagonal hybridizations the hybridization function is a matrix $\underline{\Delta}$. Therefore, instead of taking the imaginary part we can use the bath spectral function $\frac{i}{2\pi}(\underline{\Delta} - \underline{\Delta}^\dagger)$. Similarly to Eq. (7.14), we represent each interval by one delta-peak for each orbital. For instance, fixing ϵ_l to the center of the interval, the hopping parameters V_l can be found systematically from the Cholesky factorization of $\int_{I_l} \frac{i}{2\pi}(\underline{\Delta} - \underline{\Delta}^\dagger) d\omega$. Most importantly, this scheme does not involve any fitting procedure on the Matsubara axis. A very similar approach was developed independently in Ref. [125].

In step 2 we use a DMRG approach with the following parameters, unless specified otherwise. The truncated weight t_w (sum of all discarded singular values of each SVD) is kept smaller than 10^{-8}. When spin-flip and pair-hopping terms are neglected, we use an even smaller cutoff of 10^{-9}. Note that, except in the five-band calculation, we do *not* restrict the bond dimensions by some hard cutoff (see App. 7.7.2).

During time evolution (step 3), we use a truncated weight of $t_w = 2 \cdot 10^{-8}$, or 10^{-8} with density-density interactions only. We time evolve to $t = 16\,\mathrm{eV}^{-1}$, with a time step of $\Delta t = 0.01\,\mathrm{eV}^{-1}$. Green's functions are measured every fifth time step. The time-evolution operator of H_{loc} is applied using the zip-up algorithm [90]. Afterwards the Green's functions are extrapolated in time using the linear prediction method [24, 98] up to $t = 250\,\mathrm{eV}^{-1}$. Time evolution is split into two runs one forward and one backwards in time [126] to be able to reach longer times.

In the Fourier transform to ω-space (step 4), we use a broadening in the kernel $e^{i\omega t - \eta_{FT}|t|}$ of $\eta_{FT} = 0.02\,\mathrm{eV}$ to avoid cutoff effects remaining after the linear prediction. The influence of the linear prediction on our results is discussed in App. 7.7.1. We want to stress that although a calculation with full rotational symmetry is more demanding, the computational effort is still very feasible. With the parameters mentioned above one full DMFT-cycle takes about five hours on 16 cores.

To verify that our implementation of DMRG and time evolution produces correct results when used with our tensor network, we first compared Green's functions and ground-state energies for $U = J = 0$ for several bath parameter sets. The next step of our testing was to include density-density interactions, one term at a time. For example, we only included $(U' - J)n_{10\uparrow}n_{30\uparrow}$ and compared energy and Green's function to a standard one-orbital MPS solver. Finally, we also compared our method to the MPS two-band solver used in Ref. [24]. Indeed all tests performed produced correct energies and Green's functions.

7.5 Results

We performed DMFT calculations based on a band structure obtained from density functional theory (DFT) for the prototypical compound $SrVO_3$, using the approximation of the Kanamori Hamiltonian (Eq. (7.1)). It has a cubic crystal structure with a nominal filling of one electron in the V-3d shell [19]. Due to the crystal symmetry, the five orbitals of the V-3d shell split into two e_g and three t_{2g} orbitals. The latter form the correlated subspace.

---

[19] Indeed, model calculations done for fillings of $N = 2$ and $N = 3$ electrons, the latter in the insulating phase, show that these calculations are of comparable computational effort. For any N we do expect increased numerical effort close to the Mott transition though.

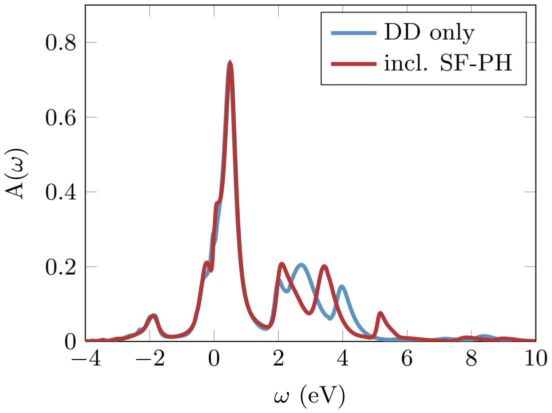

Figure 24: Spectral functions $A(\omega)$ for density-density interactions (DD) only (blue line), and with spin-flip and pair-hopping terms included (red line). In both calculations we used $U = 4.0\,\mathrm{eV}$ and $J = 0.6\,\mathrm{eV}$. Both spectra show a three-peak structure in the upper Hubbard band and additional features at high energies (around 8 eV).

We performed the DFT calculation with Wien2k [127], and used 34220 k-points in the irreducible Brillouin zone in order to reach an energy resolution comparable with the $\eta_{SC} = 0.005\,\mathrm{eV}$ broadening.

The TRIQS/DFTTools package (v1.4) [68, 128, 129], which is based on the TRIQS library (v1.4) [106], was used to generate the projective Wannier functions and to perform the DMFT self-consistency cycle.

Fig. 24 shows the main results of this paper, the DMFT spectral function $A(\omega)$ for $SrVO_3$, (i) in the approximation of density-density interactions only and (ii) with full rotational invariance including spin-flip and pair-hopping terms. Overall, both cases show the well known features of the $SrVO_3$ spectral function [130, 131]. We see a hole excitation at around $-2\,\mathrm{eV}$, and the quasi-particle peak at zero energy whose shape and position does not depend on the inclusion of full rotational invariance. In the upper Hubbard band, a distinctive three-peak structure can be seen. This structure has not been resolved in other exact methods like CTQMC (problem with analytic continuation, see below) or NRG (logarithmic discretization problem). In our real time approach, high energies correspond to short times, where

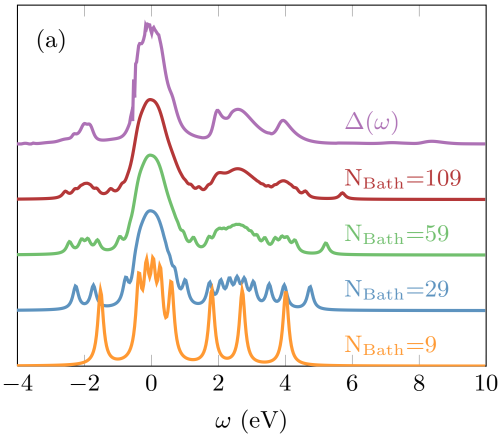

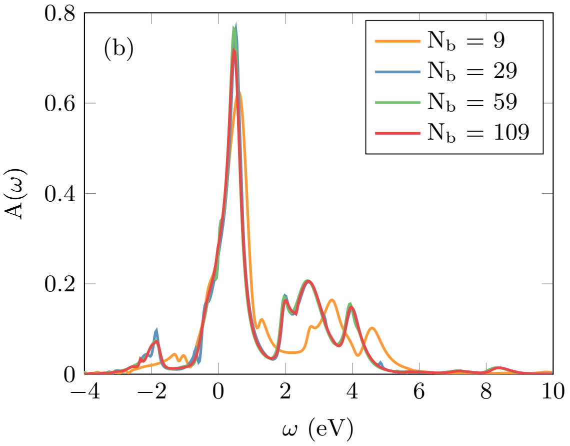

Figure 25: (a) We take the bath spectral function $\Delta(\omega)$ from the DMFT self-consistent solution for $N_b = 109$ and represent it using various numbers of bath sites. It is obvious that $N_b = 9$ is too small to represent the bath well. (b) Converged DMFT spectral function using the AIM with different numbers of bath sites. Only the smallest bath shows a noticeable difference. This is mostly due to the fact that in this case a higher broadening of $\eta_{FT} = 0.1\,\mathrm{eV}$ had to be used in the Fourier transform and time evolution was only possible to $t = 14\ \mathrm{eV}^{-1}$. The additional small structure at $\omega = 0$ for $N_b = 59$ bath sites is most likely a linear prediction artifact.

the calculations are particularly precise[20]. Most methods allow to resolve structures in the Hubbard bands only in special cases (see Ref. [132] for an example using ED). Of course, atomic-limit based algorithms such as the Hubbard-I approximation or non-crossing approximation (NCA) show atomic-like features, but they have very limited accuracy for the description of the low-energy quasi-particle excitations in the metallic phase [133]. Thus, our FTPS solver combines the best of the two worlds, with atomic multiplets at high energy and excellent low-energy resolution *at the same time*.

The energies of the three peaks in the upper Hubbard band differ depending on whether SF-PP terms are taken into account or not. Details of this peak structure, as well as additional excitations visible at higher energies, will be discussed below in Sec. 7.5.3.

First we examine the convergence of our results with respect to the number of bath sites and compare our spectrum to CTQMC. The following discussion is mostly based on calculations without spin-flip and pair-hopping terms. In this case, the calculations can be done faster and with higher precision, since there is no particle exchange between impurities. In all subsequent plots, we show results from calculations with DD interactions only.

7.5.1 Effect of Bath Size

In order to achieve a reliable high resolution spectrum on the real-frequency axis, it is imperative to have a good representation of the hybridization function $\Delta(\omega)$ in terms of the bath parameters, for which a sufficient number of bath sites is needed. Fig. 25 shows how well a hybridization function can be represented with our approach (Eq. (7.14)) using a certain number of bath sites. We see that for $N_b = 9$ bath sites (we always denote sites per orbital), $\Delta(\omega)$ can be reconstructed only very roughly, which in turn gives an incorrect spectral function (Fig. 25 bottom). To some extent, the difference in the spectrum is due to the shorter time evolution and therefore a higher broadening η_{FT} we were forced to use. For such a small bath, the finite size effects from reflections at the bath ends appear much earlier in the time

---

[20] We note that high energy peaks already appear in the first DMFT iteration, for which the bath does not have any spectral weight at high energies.

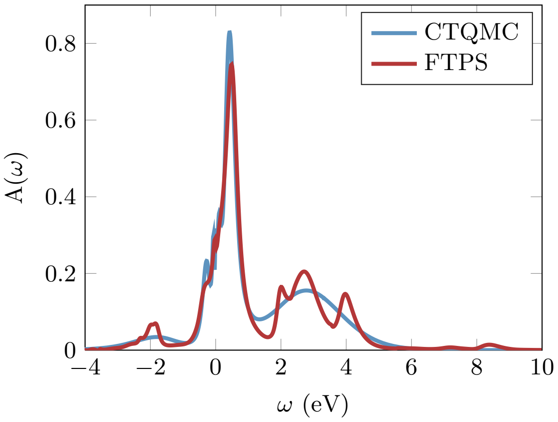

Figure 26: DMFT spectral functions $A(\omega)$ from CTQMC+MaxEnt (blue line) at $\beta = 200$ eV^{-1}, and from FTPS (red line). The FTPS result shows a distinctive three-peaked structure in the upper Hubbard band.

evolution.

Increasing the number of bath sites to $N_b = 29$, we observe that the reconstructed bath spectral function already shows the relevant features of $\Delta(\omega)$. The spectrum is well converged for the largest bath sizes $N_b = 59$ and $N_b = 109$.

7.5.2 Comparison to CTQMC

In Fig. 26 we compare the converged spectral function of our approach (FTPS) with a spectrum obtained from CTQMC and analytic continuation. In both calculations, we used the same interaction Hamiltonian with density-density interactions only. The CTQMC calculation was performed with the TRIQS CTHYB-solver (v1.4) [134, 135] with $3.2 \cdot 10^7$ measurements and at inverse temperature $\beta = 200\,\text{eV}^{-1}$. For the analytic continuation we applied the ΩMaxEnt method [136].

The three-peak structure in the upper Hubbard band is not present in the CTQMC spectrum. We will show below in an example that even for a Green's function that does contain these peaks the analytic continuation does not resolve this structure.

For another comparison, we consider the imaginary time Green's functions $G(\tau)$ in Fig. 27. Apart from the effect of statistical errors, CTQMC pro-

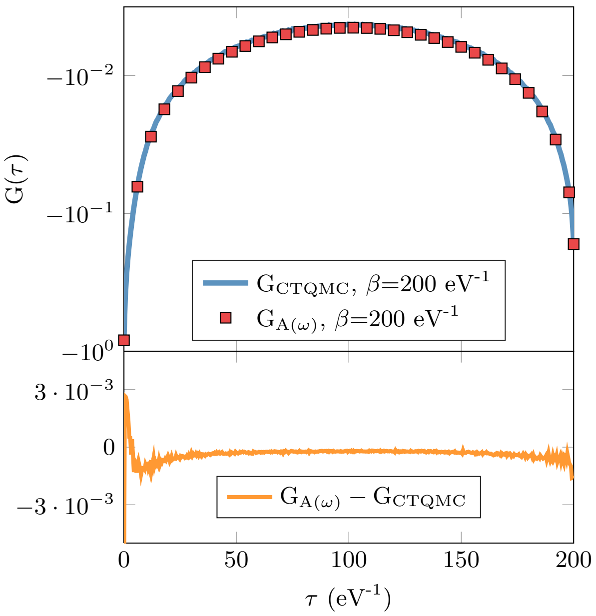

Figure 27: Comparison of imaginary time Green's functions $G(\tau)$ from CTQMC ($\mathrm{G}_{\mathrm{CTQMC}}$, blue line) and FTPS using Eq. (7.15) ($\mathrm{G}_{\mathrm{A}(\omega)}$, red squares). The agreement is equally good also at $\beta = 100$ eV^{-1} and $\beta = 400$ eV^{-1} (not shown). The difference between the two Green's functions is shown in the bottom panel. Note that on both ends $\mathrm{G}_{\mathrm{A}(\omega)}$ is smaller than $\mathrm{G}_{\mathrm{CTQMC}}$. The normalization of the spectral function demands that $G(\tau = 0) + G(\tau = \beta) = -1$. The CTQMC data deviates in the order of 10^{-2} from this constraint due to statistical noise, while FTPS gives (by construction) the correct result to a precision of 10^{-8}. This explains the bigger differences of the Green's functions around $\tau = 0$ and $\tau = \beta$. For better visibility of the $\tau > 0$ data, the value of $9 \cdot 10^{-3}$ at $\tau = 0$ is not shown.

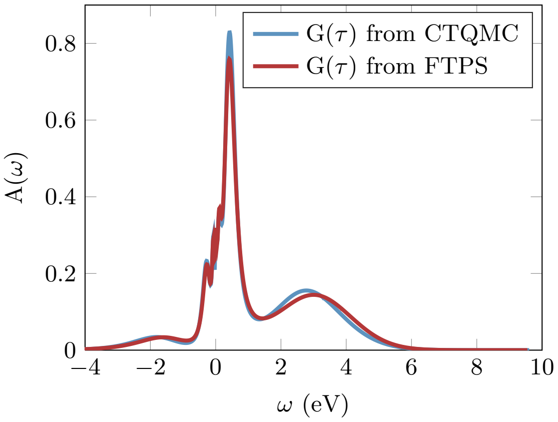

Figure 28: Spectral functions from analytically continued imaginary-time Green's functions $G(\tau)$ calculated by CTQMC (blue line) and by FTPS (red line). Clearly, the analytic continuation cannot resolve the peak structure in the upper Hubbard band.

vides an exact self consistent solution of DMFT on the imaginary-frequency axis. As mentioned above, when we use the FTPS solver, we formulate the DMFT self-consistency equations on the real-axis. To obtain an approximate finite temperature imaginary-time Green's function from FTPS that we can compare to the CTQMC result, we need to take the finite temperature of the CTQMC calculation into account. Therefore, we use the FTPS spectrum $A(\omega)$ and assume that we would obtain the same spectrum for a finite (but high enough) inverse temperature β, and use:

$$G(\tau) = \int \frac{d\omega}{2\pi} A(\omega) \frac{e^{-\omega\tau}}{e^{-\beta\omega}+1} \tag{7.15}$$

The results in Fig. 27 show very good agreement on a logarithmic scale.

Another important indication of the validity of our results is the value of $A(\omega=0)$. To get a comparable number, we use the CTQMC imaginary time Green's function $G(\tau)$ and Fourier transform it to get $G(i\omega_n)$:

$$G(i\omega_n) = \int e^{i\omega_n\tau} G(\tau) d\tau.$$

Looking at the last few DMFT-cycles, we estimate it to be around $A(\omega = 0) = -\frac{1}{\pi}\lim_{i\omega_n\to 0} \Im G(i\omega_n) \approx 0.272\,\mathrm{eV}^{-1}$ with fluctuations in the last digit.

For the FTPS, the exact height of $A(\omega = 0)$ of the FTPS spectrum changes a little for each DMFT iteration, mainly due to slight variations in the linear prediction. Using the same prescription as for CTQMC, we estimate it to be $A(\omega = 0) = 0.28$ eV^{-1}, with fluctuations of about 0.01 eV^{-1}. This agreement is very good considering that linear prediction has its strongest influence at small energies. Further benchmarks concerning the linear prediction can be found in App. 7.7.1.

Finally, we show that the ill-posedness of the analytic continuation is the most likely explanation for the missing peak structure in the upper Hubbard band of the spectral function obtained from the CTQMC data. To do so, we take the FTPS spectrum $A(\omega)$, calculate $G(\tau)$ as described above, and perform the same analytic continuation that we did for the $G(\tau)$ from CTQMC. We added noise of the order of the CTQMC error to the FTPS data. The resulting spectrum is shown in Fig. 28, and indeed the peak structure in the upper Hubbard band vanishes.

7.5.3 Discussion of Peak Structure - Effective Atomic Physics

In order to understand the peak structure observed in the spectral functions, we take a look at the underlying atomic problem, where for simplicity we start with density-density interactions only. We will show that the same arguments hold for full rotationally invariant interactions.

Tab. 2 shows the relevant atomic states and their corresponding energies. The atomic model has a hole excitation at energy $-\epsilon_0$ and three single electron excitations with energies $U + \epsilon_0$, $U - 2J + \epsilon_0$ and $U - 3J + \epsilon_0$ relative to the ground state. If we measure the energy differences between the three peaks of the upper Hubbard band in our results, we find values of 1.27 eV and 0.69 eV, which is close to the atomic energy differences of 1.2 eV and 0.6 eV ($J = 0.6$ eV). We also find the hole excitation at -2.0 eV. This indicates that we can describe the positions of the observed peaks approximately by atomic physics with effective parameters $\bar{\epsilon}_0$, $\bar{U}$ and $\bar{J}$ and widened peaks. Furthermore, the heights of the peaks roughly correspond to the degeneracy of the states in the atomic model (see Tab. 2).

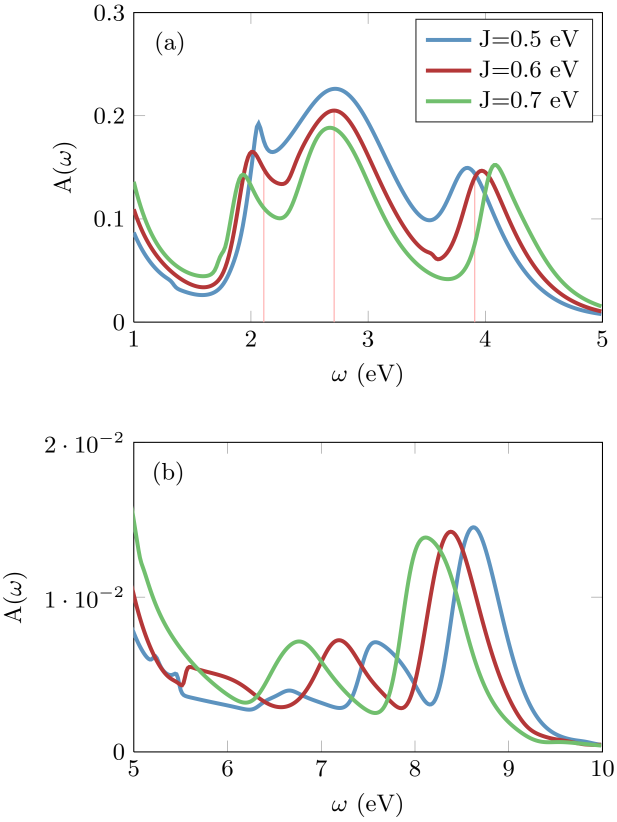

Figure 29: (a) Closeup of the three-peak structure for various values of J. Additionally, we show vertical lines for the $J = 0.6\,\mathrm{eV}$ spectrum at energies ω_M (position of the middle peak) and at $\omega_M + 2J$ and $\omega_M - J$. We see that the width of the upper Hubbard band is close to $3J$. (b) Closeup of the small spectral peaks at high energies. These correspond to excitations into the $N = 3$ sector of the atomic model (see Tab. 2). The height of each peak can be estimated by the degeneracy of the atomic states. Effective parameters $\bar{J}$ are $0.53\,\mathrm{eV}$ ($J = 0.5\,\mathrm{eV}$), $0.59\,\mathrm{eV}$ ($J = 0.6\,\mathrm{eV}$) and $0.68\,\mathrm{eV}$ ($J = 0.7\,\mathrm{eV}$). They are obtained from the difference between the two peaks highest in energy.

Table 2: Relevant states of the atomic problem of Hamiltonian (7.1) without spin-flip and pair-hopping terms. The energy is given as energy difference to the ground state.

type	states	energy	degeneracy
$N = 1$, ground state	$\lvert\uparrow, 0, 0\rangle \quad \lvert\downarrow, 0, 0\rangle \quad \lvert 0, \uparrow, 0\rangle \cdots$	0	6
$N = 0$	$\lvert 0, 0, 0\rangle$	$-\epsilon_0$	1
$N = 2$, same spin	$\lvert\uparrow, \uparrow, 0\rangle \quad \lvert\uparrow, 0, \uparrow\rangle \quad \lvert 0, \uparrow, \uparrow\rangle \cdots$	$U - 3J + \epsilon_0$	6
$N = 2$, different spin	$\lvert\uparrow, \downarrow, 0\rangle \quad \lvert\uparrow, 0, \downarrow\rangle \quad \lvert\downarrow, \uparrow, 0\rangle \cdots$	$U - 2J + \epsilon_0$	6
$N = 2$, double occupation	$\lvert\uparrow\downarrow, 0, 0\rangle \quad \lvert 0, \uparrow\downarrow, 0\rangle \quad \lvert 0, 0, \uparrow\downarrow\rangle$	$U + \epsilon_0$	3
$N = 3$, all spins equal	$\lvert\uparrow, \uparrow, \uparrow\rangle \quad \lvert\downarrow, \downarrow, \downarrow\rangle$	$3U - 9J + 2\epsilon_0$	2
$N = 3$, one spin different	$\lvert\uparrow, \uparrow, \downarrow\rangle \quad \lvert\uparrow, \downarrow, \uparrow\rangle \quad \lvert\downarrow, \uparrow, \uparrow\rangle \cdots$	$3U - 7J + 2\epsilon_0$	6
$N = 3$, double occupation	$\lvert\uparrow\downarrow, \uparrow, 0\rangle \quad \lvert\uparrow\downarrow, \downarrow, 0\rangle \quad \lvert\uparrow\downarrow, 0, \uparrow\rangle \cdots$	$3U - 5J + 2\epsilon_0$	12

Table 3: Atomic parameters and their effective values obtained from the spectral functions shown in Fig. 26 and 29. For J the values itself were obtained from the energy difference of the highest peak to the lowest peak, whereas the uncertainty is estimated from $\omega_M + 2J$ and $\omega_M - J$.

parameter	atomic value (eV)	effective value (eV)
ϵ_0	-0.86	-2.00
U	4.00	5.97
J	0.50	0.59(6)
J	0.60	0.66(3)
J	0.70	0.72(2)

We can determine $\bar{U} = 5.97\,\mathrm{eV}$ (where $U = 4.00\,\mathrm{eV}$) from the energy difference of the peak highest in energy to the hole excitation. This increase of $\bar{U}$ compared to U is plausible considering the following. When coupling the impurity to the bath, particles have the possibility to avoid each other by jumping into unoccupied sites of the bath. This results in a decrease of $\langle n_\uparrow n_\downarrow\rangle$. To model this situation using atomic physics, one needs to increase the interaction strength. Finally, it is well known that J is much less affected by the surrounding electrons than U, since the latter is screened significantly stronger [137].

Tab. 3 shows how bare atomic parameters change when adding a bath and we see that our qualitative arguments give a correct idea of how parameters are rescaled.

Further evidence that the observed three-peaked structure is indeed a result of atomic physics can be seen in Fig. 29. It shows a closeup of the upper Hubbard band for three different values of J. The corresponding effective parameters $\bar{J}$ are shown in Tab. 3. We observe that also J is rescaled slightly, but the rescaling gets smaller for higher J. Furthermore, increasing J also increases the total width of the Hubbard band, which scales mostly linearly with J. At the same time, measuring the quasi-particle spectral weight as a function of J at constant U shows that it *increases* with increasing J, implying also an increasing critical U_c for the metal-to-insulator transition [23].

Upon a careful inspection of the spectral function in Fig. 26, we observe small peaks at energies around $8\,\mathrm{eV}$. A closeup of this energy region for different values of J is shown in Fig. 29. The energy difference between the peaks is close to $2J$ and can, again, be well explained by atomic physics, namely excitations into states with 3 electrons on the impurity (Tab. 2) [21]. These excitations originate from small admixtures of $N = 2$ states to the ground state.

With atomic physics in mind, let us take a look again at the spectrum using full rotational symmetry (Fig. 24). The spin-flip and pair-hopping terms only contribute if there are two or more particles present. Thus, the quasi-particle peak and the hole excitation do not change. The atomic $N = 2$ sector does change, however. Diagonalizing the Hamiltonian, we find eigenstates with three different energies and differences of $3J = 1.8\,\mathrm{eV}$ and $2J = 1.2\,\mathrm{eV}$, resp. Measuring the energy differences in Fig. 24, we find $3\bar{J} = 1.75\,\mathrm{eV}$ and $2\bar{J} = 1.32\,\mathrm{eV}$. Estimating $\bar{U} = 5.81(5)$ we see that it does not change much compared to DD only[22]. Again, we can describe the spectrum approximately by atomic physics with effective parameters. Like in the case with density-density terms only, we also see the tiny excitations to states belonging to the atomic $N = 3$ sector.

---

[21] Nevertheless, the effective parameters $\bar{J}$ differ a little from those obtained from the main Hubbard band.

[22] Note that the peak highest in energy has an atomic energy of $E = U + 2J + 2\epsilon_0$. Therefore, $\bar{U}$ can only be determined after $\bar{J}$ is found.

7.5.4 Beyond Atomic Physics

The previous section showed that at $U = 4.0\,\text{eV}$ the spectral features in the Hubbard bands can be well described by atomic physics with effective parameters and widened peaks. It is not clear whether this picture is valid for higher interaction strengths U in the metallic regime. In Fig. 30 we show results with $U = 5.5\,\text{eV}$ at constant $J = 0.6\,\text{eV}$. We see a shift of the upper Hubbard band to higher energies, but little shift of the hole-excitation. Also the central peak is shifted and gets slimmer since more weight is transferred into the Hubbard bands. Most importantly, as we approach the strongly-correlated metallic regime, we clearly leave the realm where atomic physics can describe all the spectral features.

We find that the three-peak structure of the upper Hubbard bands smears out, and even vanishes. The closeup of the upper Hubbard band in Fig. 30 shows that with the help of the bare energy differences all three atomic peaks can be discerned again, accompanied by an additional structure at the low-energy side of the Hubbard band, which is reminiscent of the Hubbard side peaks found in the one- and two-band Hubbard model on the Bethe lattice [24] upon increasing U. We leave further investigation of this feature to future work.

It might at first seem counter-intuitive that increasing U makes the physics less atomic-like. Indeed, at very high interaction strengths, in the insulating regime, the spectrum must become atomic-like again. Here, however, we identify an intermediate regime where additional structures appear when increasing U, since we get closer to the Mott metal-to-insulator transition.

7.5.5 Solution of a five-band AIM

In this section we show that FTPS can not only deal with three-band models, but also work in the case of five orbitals. To do so, we use the bath parameters ϵ_k and V_k from the converged $N_b = 59$ calculation for SrVO_3 and construct an

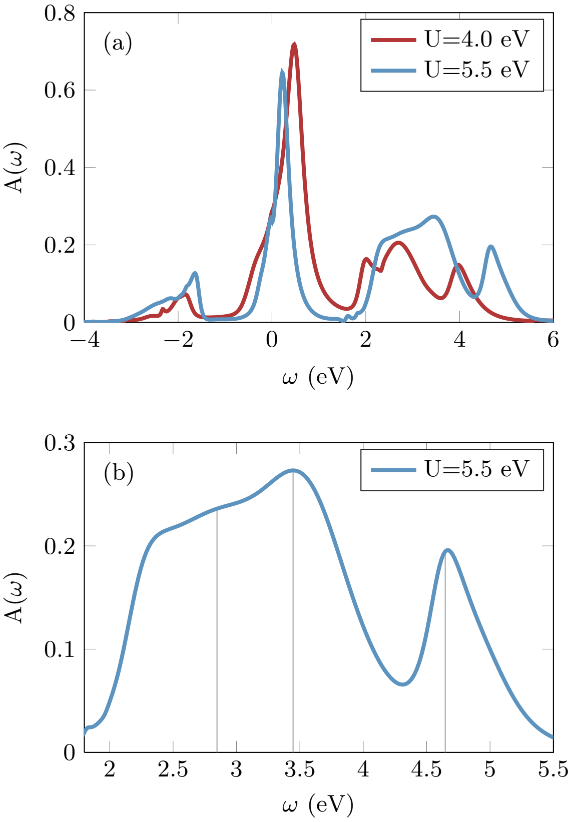

Figure 30: (a) Increasing U results in a slimmer central peak and a shift of the upper Hubbard band. Also the three-peaked structure gets smeared out. (b) Closeup of the upper Hubbard band. As in Fig. 29, additional vertical lines are plotted at ω_M (position of the middle peak) and at $\omega_M + 2J$ and $\omega_M - J$ as a rough guide to where the atomic peaks would be located. With the help of these lines one can discern a three-peaked structure again, but extended by a feature at the inside of the Hubbard band.

artificial degenerate five-band AIM. Interaction parameters are $U = 4.0\,\text{eV}$ and $J = 0.6\,\text{eV}$. We decrease the on-site energy ϵ_0 to get a similar occupation of each impurity orbital as for SrVO$_3$ ($\langle n_{m,0,\sigma}\rangle \approx \frac{1}{6}$). Note that in doing so we have a model with, in total, $\frac{5}{3}$ electrons on the impurity. We only use density-density interactions and carry out the time evolution to $t = 16\,\text{eV}^{-1}$. We set the truncated weight to $t_w = 10^{-8}$, but restrict the bond dimension of the impurity-impurity links to $\chi_{max} = 200$.

In Fig. 31 we compare the results obtained for this five-band model to results from CTQMC, where we used the same discretized bath hybridization as input to CTQMC. We again see excellent agreement, even on a logarithmic scale. The spectrum $A(\omega)$ (not shown) again exhibits strong structure in the upper Hubbard band. Of course, the computational complexity is larger than in the three-orbital case and it grows during time evolution. Calculating the Green's function took about 190 hours on the processors specified in App. 7.7.2. We want to stress tough that the resulting spectrum (as well as Fig. 31) was already fully converged at $t = 12\,\text{eV}^{-1}$ (70 hours). We note that even with only one CPU hour ($t = 6\,\text{eV}^{-1}$) the resulting spectrum is almost converged and barely distinguishable from the final result. The benchmark therefore shows that with our FTPS approach a full five-orbital DMFT calculation is well within reach.

7.6 Conclusions

We have presented a novel multi-orbital impurity solver which uses a fork-like tensor network whose geometry resembles that of the Hamiltonian. The network structure is simple enough to generate Schmidt decompositions, allowing us to truncate the tensor network safely and to use established methods like DMRG and real time evolution. The solver works on the real frequency axis, and hence allows to formulate the full DMFT self consistency procedure for real frequencies. Therefore, results are not plagued by an ill-conditioned analytic continuation. Our approach exhibits no sign problem, tough it does become more involved for larger numbers of orbitals.

We tested the solver within DMFT on a Hamiltonian typically used for

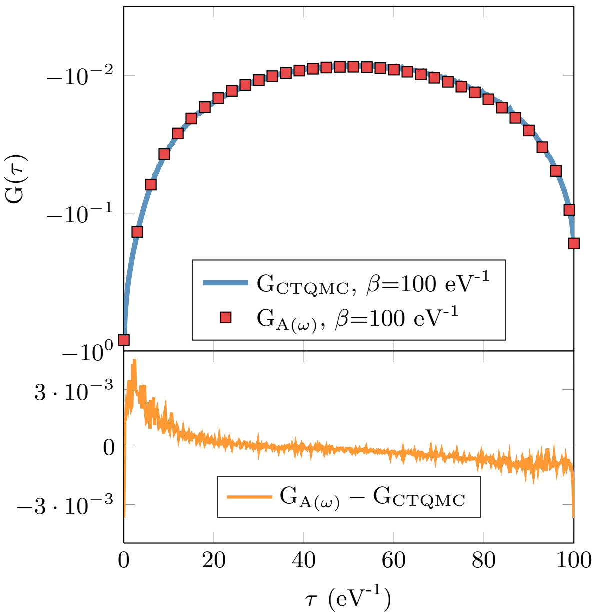

Figure 31: Comparison of imaginary time Green's functions $G(\tau)$ from CTQMC ($\mathrm{G}_{\mathrm{CTQMC}}$, blue line) and FTPS using Eq. (7.15) ($\mathrm{G}_{\mathrm{A}(\omega)}$, red squares). As in Fig. 27 they compare very well.

the testbed material SrVO_3 and investigated the influence of full rotational invariance on the results. We found clear spectral structures in particular in the upper Hubbard band that have not been accessible by CTQMC, for which the necessary analytic continuation prohibits the resolution of fine structures in the spectral function at higher energies. For our calculations with $U = 4.0\,\mathrm{eV}$, each peak in the spectrum corresponds to an atomic excitation. Even excitations into states with three particles on the impurity are resolved, as tiny spectral peaks at high energies. Furthermore, upon increasing U, an additional structure appears on the inside of the Hubbard bands, similar to the precursors of the sharp Hubbard side peaks found for the one- and two-band Hubbard models on the Bethe lattice [24, 46]. We have also shown that our approach is feasible for five-orbital models, by comparing results from the FTPS solver to CTQMC for an artificial five-band model.

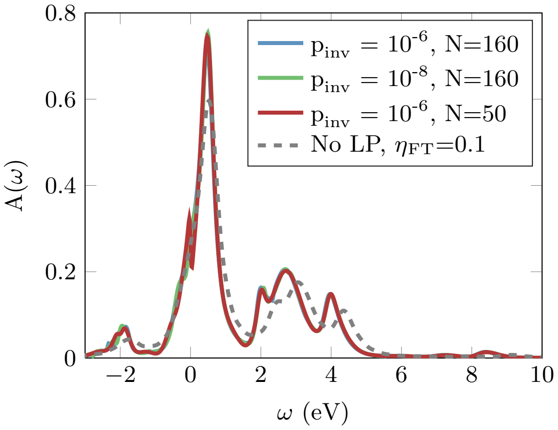

Figure 32: Spectrum $A(\omega)$ using different linear prediction (LP) parameters for a calculation without spin-flip and pair-hopping terms. The calculations with LP were performed with a broadening of $\eta_{FT} = 0.02$ eV. Except for small changes around $\omega = 0$, the effect of the various LP parameters is minor. The blue line directly lies below the red and green line. We also show a DMFT calculation without any LP. Even then the main features are still present.

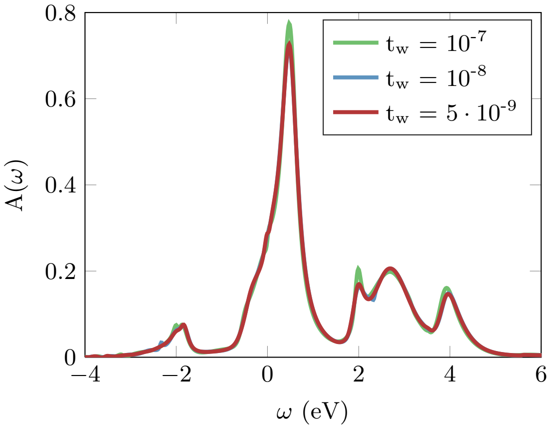

Figure 33: Different truncation values t_w in the time evolution do not influence the shape of the spectrum $A(\omega)$.

7.7 Appendix

In this appendix we show that our results are very stable over a wide range of computational parameters. First we focus on the linear prediction method (Sec. 7.7.1). Then we show that the results are converged with respect to the usual MPS-approximation (Sec. 7.7.2).

7.7.1 Linear Prediction

In order to obtain smooth and sharp spectra, we used linear prediction (LP) to extrapolate the Greens function in time [24, 98]. Without going into detail, we state the fact that linear prediction has two parameters, the pseudo inverse cutoff p_{inv} and the order N of the linear prediction. Fig. 32 shows that the results are converged in these parameters.

We also show a DMFT run without any linear prediction, which is only possible if we increase the broadening parameter of the Fourier transform to $\eta_{FT} = 0.1\,\text{eV}$, since otherwise we would get oscillations due to the hard cutoff of the time series. Except for a shift towards the right, omitting the linear prediction only changes the height (and width) of the peaks, but not the overall structure. This is a strong indicator of the stability of these features.

7.7.2 Truncation of the Tensor Network

One, if not the most important, parameter in any MPS-like calculation is the sum of discarded singular values in each SVD (truncated weight t_w). We want to emphasize that this parameter is the only approximation in the representation of a state as a tensor-product state, as we do not impose any hard cutoff on the bond dimensions. Fig. 33 shows that the spectrum is well converged with respect to the truncation error during time evolution.

Finally, we want to comment on the required computational effort. In the calculation without full rotational symmetry, the size of the largest tensor to represent the ground state was[23] $35 \times 22 \times 9 \times 2$ ($t_w = 10^{-9}$) and at the end of time evolution $127 \times 79 \times 30 \times 2$ ($t_w = 10^{-8}$). For a truncated weight of $t_w = 10^{-7}$, calculating the Greens function took about 17 minutes on a node with two processors (Intel Xeon E5-2650v2, 2.6 GHz with 8 cores, and $G^>$ and $G^<$ each calculated on one processor). This time increases to five hours for the lowest truncated weight of $t_w = 5 \cdot 10^{-9}$. Using the full

---

[23] 35 and 22 correspond to the impurity links, 9 is the bond dimension to the first bath site and 2 is the physical bond dimension.

rotationally invariant Hamiltonian, the biggest tensor in the ground-state search was $90 \times 40 \times 10 \times 2$ ($t_w = 10^{-8}$) and at the end of time evolution $79 \times 46 \times 21 \times 2$ ($t_w = 2 \cdot 10^{-8}$). The Greens function takes about three hours, and we need five hours for one full DMFT-cycle on the same two processors as above.

8 $SrMnO_3$ Atomic- and Hybridization Multiplets (*arXiv:1712.08055*)

In this section we present the results published in Ref. [4], which is one of the main publications of the author of the present work. The author implemented the FTPS impurity solver, performed all FTPS calculations and was the main contributor in writing the publication. Manuel Zingl performed the DFT calculation and implemented the DMFT self consistency on the real frequency axis within the TRIQS library (v1.4) [106]. Furthermore, he performed the CTQMC calculations that we used to compare our results with, and helped with writing the paper. Robert Triebl performed the analytic continuation of the imaginary time Green's functions and together with the author was responsible for the development and discussion of the *toy models* presented below. Furthermore, he played an important role in writing the paper.

In this publication we used the FTPS solver for the strongly correlated insulator $SrMnO_3$ with a nominal filling of three electrons. Therefore, the half filled t_{2g} subspace tends to become a Mott insulator with a lower- and upper Hubbard band. In addition to the low energy t_{2g} bands, the DFT band structure shows e_g bands directly above the Fermi energy. Furthermore, hybridizations of the Mn-3d bands with oxygen p-bands are close to the lower Hubbard band. Including them would mean to increase the energy window in which the low-energy Hubbard Hamiltonian is constructed. Therefore, we asked the following question. How does the number of correlated orbitals and the size of the energy window affect the DMFT spectral function? Since differences between these low-energy models are most apparent in the high-energy spectral features, it is vital to have high resolution on the real frequency axis, calling for a real-frequency solver such as FTPS. We found that the hybridizations of the t_{2g} bands with the oxygen p-bands lead to a splitting of the lower Hubbard band into a more complex structure. This shows that this compound is neither a pure Mott- nor a pure charge transfer insulator. Furthermore, we found that also the e_g bands should be included, as their spectrum shows a multiplet structure through interactions with the half filled t_{2g} bands. We therefore argue that in order to describe the spectrum of SrMnO$_3$, a five band calculation including the full Mn-3d-shell and using a large energy window has to be performed. We found that the spectral function of such a calculation is in good agreement with XAS and PES experiments. Especially, the XAS measurement shows a three peak structure of alternating e_g -t_{2g} -e_g character, a feature that we can observe in the DMFT spectrum as well.

The paper is included in its entirety in the following. To obtain a single, coherent bibliography for the present thesis the citations are merged into one list of references at the end of the thesis.

8.1 Abstract

We investigate the electronic structure of SrMnO$_3$ with Density Functional Theory (DFT) plus Dynamical Mean-Field Theory (DMFT). Within this scheme the selection of the correlated subspace and the construction of the corresponding Wannier functions is a crucial step. Due to the crystal field splitting of the Mn-3d orbitals and their separation from the O-2p bands, SrMnO$_3$ is a material where on first sight a 3-band d-only model should be sufficient. However, in the present work we demonstrate that the resulting spectrum is considerably influenced by the number of correlated orbitals and the number of bands included in the Wannier function construction. For example, in a *d*-*dp* model we observe a splitting of the t_{2g} lower Hubbard band into a more complex spectral structure, not observable in d-only models. To illustrate these high-frequency differences we employ the recently developed Fork Tensor Product State (FTPS) impurity solver, as it provides the necessary spectral resolution on the real-frequency axis. We find that the spectral structure of a 5-band *d*-*dp* model is in good agreement with PES and XAS experiments. Our results demonstrate that the FTPS solver is capable of performing full 5-band DMFT calculations directly on the real-frequency axis.

8.2 Introduction

The combination of density functional theory (DFT) and dynamical mean-field theory (DMFT) has become the work-horse method for the modeling of strongly-correlated materials [12, 13, 122]. For DMFT, a (multi-orbital) Hubbard model is constructed in a selected correlated subspace, which usually describes the valence electrons of the transition metal orbitals in a material. An adequate basis for these localized orbitals are projective Wannier functions [67, 68]. In contrast to the Bloch wave functions, these functions are localized in real space, and therefore provide a natural basis to include local interactions as they resemble atomic orbitals and decay with increasing distance from the nuclei. However, the selection of the correlated subspace itself and the Wannier function construction are not uniquely defined.

In the present work, we use $SrMnO_3$ to analyze the differences of some common models. This perovskite is an insulator [24] with a nominal filling of three electrons in the Mn $3d$ shell. There are various works concerning its electronic structure, both on the experimental [138–143] as well as on the theoretical side [144–147]. For the construction of the correlated subspace, we explicitly identify the following meaningful cases: The first is a three orbital model for the t_{2g} states only. For the second choice, usually denoted as *d-dp* model, the transition metal $3d$-states and the oxygen $2p$-states are considered in the Wannier function construction, but the Hubbard interaction is only applied to the $3d$-states. The correlated subspace is then affected by the lower lying oxygen bands due to hybridizations. In both cases, the full $3d$ manifold can be retained by including the e_g orbitals in genuine 5 orbital models.

To assess the consequences of the different low-energy models, a good resolution of the spectral function on the real-frequency axis is beneficial. Due to its exactness up to statistical noise, Continuous Time Quantum Monte Carlo (CTQMC) is often used as a DMFT impurity solver [14, 15, 135]. However, when using a CTQMC impurity solver, an analytic continuation is necessary, which results in spectral functions with a severely limited resolution at higher

---

[24] Although most published work suggest that the compound is insulating, the experimental magnitude of the gap ranges from approximately 1.0 eV to 2.0 eV, see citations in the main text.

frequencies [1]. This can make it difficult to judge the influence of the choices made for the correlated subspace. In the present paper, we therefore employ the real-frequency Fork Tensor Product States (FTPS) solver [1]. This recently developed zero temperature impurity solver was previously applied to $SrVO_3$, making it possible to reveal an atomic multiplet structure in the upper Hubbard band [1]. This observation of a distinct multiplet structure in a real-material calculation is an important affirmation of the atom-centered view promoted by DMFT.

The present work also serves as a deeper investigation of the capabilities of the FTPS solver. We show that the FTPS solver can be applied to d-dp models, leading to new insight into the interplay of the atomic physics of the transition metal impurity and hybridization effects with the oxygen atoms as a natural extension to the atom-centered view. Furthermore, the physics of $SrMnO_3$ is different from $SrVO_3$, since the manganate is an insulator, and thus it constitutes a new challenge for the FTPS solver. While we presented a proof of concept for FTPS on a simple 5-band model before [1], we now perform full 5-band real-frequency DFT+DMFT calculations for both d-only and d-dp models.

We find that the choices made for the correlated subspace strongly affect the resulting spectral function and its physical interpretation. Additionally, we show that the interplay of atomic and hybridization physics can already be found in very simple toy models.

This paper is structured as follows. In section 8.3 we discuss the methods employed, namely DFT, the different models obtained from different Wannier constructions, DMFT, and the impurity solvers used. Section 8.4 focuses on the results of the DMFT calculations and the underlying physics of these different models. This knowledge will then be used in Sec. 8.5 to compare the spectral function to experiments by Kim *et al.* [143].

8.3 METHOD

8.3.1 DFT and WANNIER BASIS

We start with the DFT density of states (DOS) from a non-spin-polarized DFT calculation for $SrMnO_3$ in the cubic phase (shown in Fig. 34). The calculation was performed with Wien2k [127], using 969 k-points in the irreducible Brillouin zone and a lattice parameter of $a = 3.768\,\text{Å}$. Around the Fermi energy E_F, $SrMnO_3$ has the characteristic steeple-like shaped DOS, stemming from the Mn-t_{2g} bands with a bit of O-$p_{x/y}$ contribution. Below $-2.0\,\text{eV}$, the DOS is mainly determined by oxygen bands which also exhibit manganese hybridizations. With the exception of some additional weight below $-5.0\,\text{eV}$, the Mn-e_g states lie mainly in the energy range from $0.0\,\text{eV}$ to $5.0\,\text{eV}$.

In this work we use projective Wannier functions, where an energy interval has to be chosen as a projection window [67, 68]. The bands around E_F have mainly t_{2g} character, suggesting a selection of only a narrow energy window for the Wannier function construction ($-2.0\,\text{eV}$ to $0.82\,\text{eV}$). We call this set of projective Wannier functions the 3-band d-only model. However, the t_{2g} orbitals also show a considerable hybridization with the O-2p states below $-2\,\text{eV}$, and hence, one might want to enlarge the projective energy window by setting its lower boundary to $-10\,\text{eV}$. We refer to this model as the 3-band d-dp model.

At the same time, we realize that also the e_g orbitals are not entirely separated from the t_{2g} orbitals in energy and that they have even some weight around E_F (see middle graph of Fig. 34). These states lie directly above E_F and therefore their influence on the resulting spectrum needs to be checked. One should then use a window capturing 5 bands, the e_g and t_{2g} , as a correlated subspace (from $-2\,\text{eV}$ to $5\,\text{eV}$). This is a 5-band d-only model. Note that empty orbitals do not pose a problem for the FTPS solver. Like before, we can again enlarge the energy window to include the oxygen hybridization ($-10\,\text{eV}$ to $5\,\text{eV}$). We denote this model as the 5-band d-dp model.

In total, we end up with 4 different choices. The settings for these 4 models are summarized in Tab. 4. All of them are justified, have different descrip-

Table 4: Summary of models with their projective energy windows and the parameters used in the FTPS solver: number of bath sites N_B, Fourier transform broadening η_{FT}, truncated weight t_w and maximal bond dimension allowed for the links between impurities as well as for the links between an impurity and the first bath tensor. We keep at most this number of states and increase t_w if needed. The number in brackets is the maximal bond dimension during ground state search, while the first number is used for the time evolution. The bath links were not restricted to any maximal bond dimension. The FTPS time evolution is performed up to t_{max}, given in eV^{-1}.

Model	**Window** (eV)	**Comments**	$\mathbf{N_B}$	$\boldsymbol{\eta_{FT}}$	$\mathbf{t_w}$	**Bond dim.**	$\boldsymbol{t_{max}}$
3-band *d*-only	-2.0 - 0.82	only major t_{2g} weight around E_F	79	0.08	$5 \cdot 10^{-9}$	-	14.0
5-band *d*-only	-2.0 - 5.0	include e_g , neglect hybridizations	49	0.15	$1 \cdot 10^{-8}$	200 (150)	12.0
3-band *d*-*dp*-model	-10.0 - 5.0	include hybridized t_{2g} weight on oxygen bands	59	0.1	$1 \cdot 10^{-8}$	450 (150)	14.0
5-band *d*-*dp*-model	-10.0 - 5.0	t_{2g} and e_g bands with hybridizations	49	0.2	$1 \cdot 10^{-8}$	200 (150)	7.0

tive power, and have been employed in various DFT+DMFT calculations for SrMnO$_3$ [144, 145, 147].

8.3.2 DMFT

Once the correlated subspace is defined, we use DMFT [9, 13, 63, 122] to solve the resulting multi-band Hubbard model. As interaction term we choose the 5/3-band Kanamori Hamiltonian [21]. Within DMFT, the lattice problem is mapped self consistently onto an Anderson impurity model (AIM) with the Hamiltonian

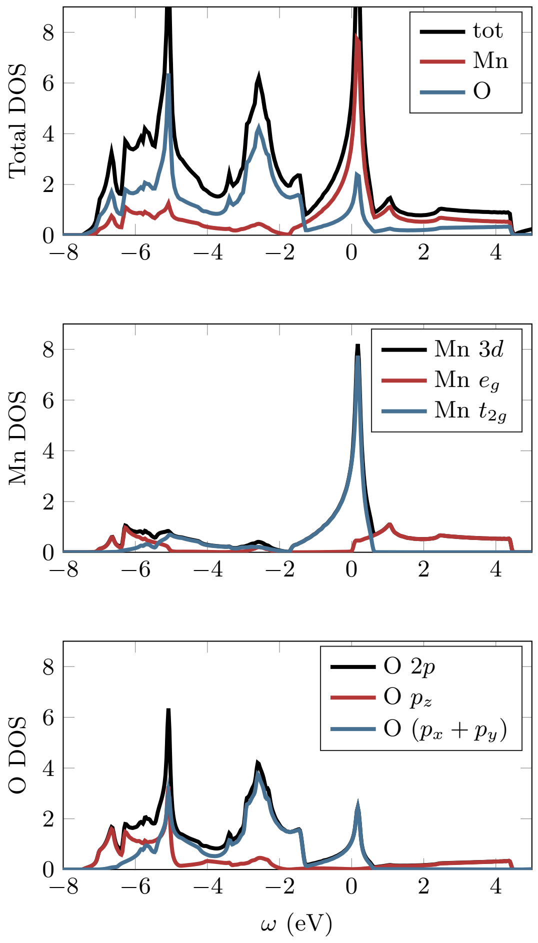

Figure 34: *Top:* Total DFT-DOS for $SrMnO_3$. *Middle:* partial Mn-$3d$ DOS. *Bottom:* partial O-$2p$ DOS for $SrMnO_3$. Below approximately $-1.5\,\mathrm{eV}$, the band structure consists of oxygen bands that have mostly p-character but also have some e_g and t_{2g} weight due to hybridizations. The t_{2g} bands are located around the Fermi energy from $-1.5\,\mathrm{eV}$ to about $0.5\,\mathrm{eV}$, which have small p-character. Directly above the Fermi energy and partly overlapping with the t_{2g} bands we find the e_g bands that have small p-contributions as well.

$$
\begin{aligned}
H &= H_{\text{loc}} + H_{\text{bath}} \qquad (8.1)\\
H_{\text{loc}} &= \sum_{m\sigma} \epsilon_{m0} n_{m0\sigma} + H_{\text{DD}} + H_{\text{SF-PH}}\\
H_{\text{DD}} &= U \sum_{m} n_{m0\uparrow} n_{m0\downarrow}\\
&\quad + (U-2J) \sum_{m'>m,\sigma} n_{m0\sigma} n_{m'0\bar{\sigma}}\\
&\quad + (U-3J) \sum_{m'>m,\sigma} n_{m0\sigma} n_{m'0\sigma}\\
H_{\text{SF-PH}} &= J \sum_{m'>m} \left(c^{\dagger}_{m0\uparrow} c_{m0\downarrow} c_{m'0\uparrow} c^{\dagger}_{m'0\downarrow} + \text{h.c.} \right)\\
&\quad - J \sum_{m'>m} \left(c^{\dagger}_{m0\uparrow} c^{\dagger}_{m0\downarrow} c_{m'0\uparrow} c_{m'0\downarrow} + \text{h.c.} \right)\\
H_{\text{bath}} &= \sum_{ml\sigma} \epsilon_{ml} n_{ml\sigma} + V_{ml} \left(c^{\dagger}_{m0\sigma} c_{ml\sigma} + \text{h.c.} \right) .
\end{aligned}
$$

Here, $c^{\dagger}_{ml\sigma}$ ($c_{ml\sigma}$) creates (annihilates) an electron in orbital m, with spin σ at site l (site zero is the impurity). $n_{ml\sigma}$ are the corresponding particle number operators. ϵ_{m0} is the orbital dependent on-site energy of the impurity and ϵ_{ml} as well as V_{ml} are the bath on-site energies and the bath-impurity hybridizations, respectively.

The interaction part of Hamiltonian (8.1), $H_{\text{DD}} + H_{\text{SF-PH}}$, is parametrized by a repulsive interaction U and the Hund's coupling J. For each of the models presented in Tab. 4, we choose these parameters *ad hoc* in order to obtain qualitatively reasonable results. In addition, for the full 5-band *d-dp* model we also estimate them quantitatively via a comparison to an experiment.

Within DFT+DMFT, a so-called double counting (DC) correction is necessary, because part of the electronic correlations are already accounted for by DFT. For general cases, exact expressions for the DC are not known, although there exist several approximations [74–77]. In the present work we use the fully-localized-limit (FLL) DC (Eq.(45) in Ref. [78]). When needed, we adjust it to account for deviations from the true, unknown DC. Note that in the d-only models, the DC is a trivial energy shift that can be absorbed into the chemical potential [76], which is already adjusted to obtain the correct number of electrons in the Brillouin zone. This step, as well as all other interfacing between DFT and DMFT, is performed using the TRIQS/DFTTools package (v1.4) [68, 106, 128, 129].

8.3.3 CTQMC + MaxEnt

We compare some of our results to CTQMC data at an inverse temperature of $\beta = 100\,\mathrm{eV}^{-1}$ obtained with the TRIQS/CTHYB solver (v1.4) [134, 135]. We calculate real-frequency spectra with an analytic continuation using the freely available Ω-MaxEnt implementation of the Maximum Entropy (MaxEnt) method [136]. However, the analytic continuation fails to reproduce high-energy structure in the spectral function, as we have shown in Ref. [1] on the example of $SrVO_3$. This is especially true when the imaginary-time Green's function is subject to statistical noise, which is inherent to Monte Carlo methods.

8.3.4 FTPS

For all models studied we employ FTPS [1]. This recently developed impurity solver uses a tensor network geometry which is especially suited for AIMs. The first step of this temperature $T = 0$ method is to find the absolute ground state including all particle number sectors with DMRG [16]. Then the interacting impurity Green's function is calculated by real-time evolution. Since entanglement growth during time evolution prohibits access to arbitrary long times [17], we calculate the Green's function up to some finite time (see Tab. 4) and predict the time series using the linear prediction method [1, 98] up to times $\mathcal{O}(100eV^{-1})$. The linear prediction could potentially produce artifacts in the spectrum, and therefore we always make sure that every spectral feature discussed in this work is already present in the finite-time Green's function without linear prediction.

The main approximations that influence the result of the FTPS solver are the broadening η_{FT} used in the Fourier transform [25], and the truncation of the tensor network [1]. The former corresponds to a convolution with a Lorentzian in frequency space making its influence predictable, while the truncation can be controlled by including more states. This control over the approximations allows us to analyze spectral functions in greater detail than what would be possible with CTQMC+MaxEnt. The parameter values for our FTPS calculations are listed in Tab. 4.

Note that we choose η_{FT} larger than in our previous work [1]. The reason for doing this is two-fold: First, some of the calculations we show in this work have a large bandwidth, which lowers the energy resolution if we keep the number of bath sites fixed. Second, FTPS uses a discretized bath to represent the continuous non-interacting lattice Green's function G_0^{cont}. When calculating the self energy $\Sigma = G_0^{-1} - G^{-1}$, we can either use the discretized version of G_0^{discr} or the continuous one, G_0^{cont}. In this work we choose G_0^{discr}, which is formally the correct choice. This then requires to use a larger broadening to obtain causal self energies that do not show finite discretization effects from inverting G_0^{discr}. However, when calculating the final impurity spectral function shown in all figures, we employ a very small broadening of $\eta_{FT} = 0.01\,\text{eV}$ in order to obtain optimal resolution.

The real-frequency approach of FTPS allows to resolve spectral features with higher precision than CTQMC+MaxEnt. This is especially true for high energy multiplets. On the other hand, with FTPS and real-time evolution it is difficult to obtain perfect gaps, since the results are less precise at small ω, encoded in the long-time properties of the Green's function which we obtain only approximately using linear prediction [98].

With FTPS we calculate the greater and lesser Green's functions separately [1]. Since the greater (lesser) Green's function has no contribution at $\omega < 0$ ($\omega > 0$) we restricted the contributions of the calculated Green's functions in frequency space.

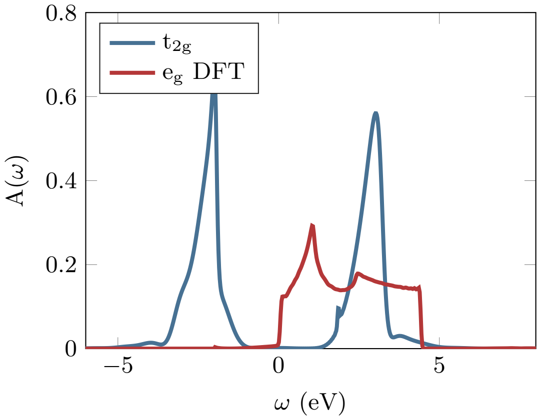

Figure 35: 3-band d-only calculation: t_{2g} correlated spectral function for $U = 4.0\,\mathrm{eV}$ and $J = 0.6\,\mathrm{eV}$, as well as e_g DFT-DOS. The t_{2g} spectrum shows a Mott insulator at half-filling with pronounced lower and upper Hubbard bands.

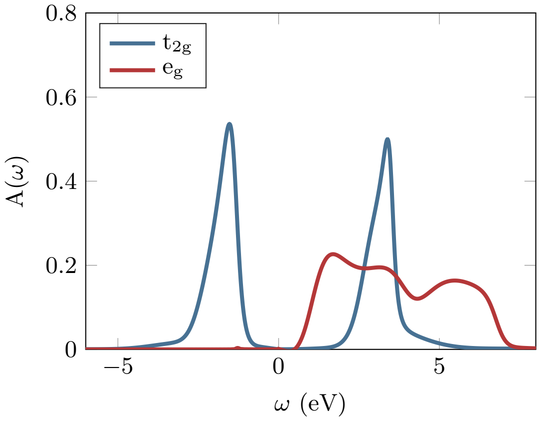

Figure 36: 5-band d-only calculation: correlated spectral function of the e_g and the t_{2g} orbitals for $U = 4.0\,\mathrm{eV}$ and $J = 0.6\,\mathrm{eV}$.

8.4 RESULTS

8.4.1 *d*-only models

First we focus on d-only calculations using a projective energy window with a lower energy boundary of $-2.0\,\mathrm{eV}$ for the Wannier-function construction, neglecting the occupied Mn-3d weight at lower energies (see Tab. 4 and middle graph of Fig. 34). With this choice of the correlated subspace, the occupation of the e_g orbitals is nearly zero and the three degenerate t_{2g} orbitals are half-filled.

3-band calculation

Considering only the t_{2g} subspace, the resulting impurity spectral function (Fig. 35) is gapped for the chosen interaction values. The peaks of the lower and upper Hubbard bands are separated by 5.0 eV in energy, which is roughly $U + 2J = 5.2\,\mathrm{eV}$, as expected from atomic physics [23].
Contrary to SrVO$_3$, where a distinct 3-peak multiplet structure in the upper Hubbard band is present [1], both SrMnO$_3$ Hubbard bands show only one dominant peak. The structure observed in SrVO$_3$ was well explained by the atomic multiplets of the interaction Hamiltonian H_{loc} in Eq. 8.1 for a ground state with one electron occupying the t_{2g} orbitals. The absence of such an atomic multiplet structure in this model for SrMnO$_3$ can be understood in a similar way: The large Coulomb repulsion in combination with Hund's rules (due to the density-density interaction strengths U, $U - 2J$ and $U - 3J$) lead to a ground state $|\psi_0\rangle$ which consists mostly of the states $|\uparrow, \uparrow, \uparrow\rangle$ and $|\downarrow, \downarrow, \downarrow\rangle$ on the impurity. Adding a particle, when calculating the Green's function, produces a single double occupation, e.g., $c^\dagger_{1,\downarrow} |\psi_0\rangle = |\uparrow\downarrow, \uparrow, \uparrow\rangle$. This state is an eigenstate of the atomic Hamiltonian, because it is trivially an eigenstate of H_{DD}, and both the spin-flip and pair-hopping terms annihilate this state. Hence, all t_{2g} single-particle excitations from the ground state have the same energy, and as a consequence, only *one* atomic excitation energy is observed. Although not included in the low-energy model, the uncorrelated states still

---

[25] We Fourier transform with a kernel $e^{i\omega t - \eta_{FT}|t|}$

need to be taken into account for the single-particle gap of $SrMnO_3$. On the unoccupied side, the onset of the e_g orbitals leads to a reduction of the single-particle gap to about half the size of the t_{2g} gap (see Fig. 35). On the occupied side, depending on U and J, either the lower Hubbard band or the O-bands (at about $-1.5\,\mathrm{eV}$) determine the gap size, and thus also the type of the insulating state (Mott or charge transfer insulator [148]). For $SrMnO_3$ to be clearly classified as Mott insulator, $U + 2J < 3.0\,\mathrm{eV}$ would be required. However, it is questionable if the d-only picture is correct, as in this case the lower Hubbard band is not influenced by the t_{2g} /O-2p hybridizations between $-6.0\,\mathrm{eV}$ and $-2.0\,\mathrm{eV}$ (see Fig 34). We will discuss the effect of these hybridizations in detail in Sec. 8.4.2 and Sec. 8.4.3.

5-band calculation

Next, we add the e_g orbitals to the correlated subspace, which now comprises the full Mn-3d manifold. The resulting impurity spectral functions of the e_g and t_{2g} orbitals are shown in Fig. 36. The t_{2g} spectral weight does not change much compared to the 3-band calculation. This is to be expected, because the e_g orbitals remain nearly empty during the calculation of the t_{2g} Green's function.

The e_g spectral function, on the other hand, becomes much broader in comparison to the DFT-DOS, showing spectral weight above $4.5\,\mathrm{eV}$. The unoccupied part of the spectrum is encoded in the greater Green's function, i.e., adding a particle in an e_g orbital to the ground state. If we again assume $|\psi_0\rangle \propto |\uparrow,\uparrow,\uparrow\rangle + |\downarrow,\downarrow,\downarrow\rangle$ as the t_{2g} ground state, we can add a particle to the e_g orbitals either in a high-spin or low-spin configuration:

$$c^\dagger_{e_g\uparrow}\,|\psi_0\rangle \propto \underbrace{|\uparrow,\uparrow,\uparrow\rangle}_{t_{2g}} \otimes \underbrace{|\uparrow,0\rangle}_{e_g} + |\downarrow,\downarrow,\downarrow\rangle \otimes |\uparrow,0\rangle\,. \tag{8.2}$$

Using the Kanamori Hamiltonian, the high-spin configuration (first term in Eq. 8.2) generates a single atomic excitation energy, while the low-spin configuration (second term in Eq. 8.2) leads to two energies (due to the spin-flip terms). According to this atomistic picture, the splitting of the e_g peaks

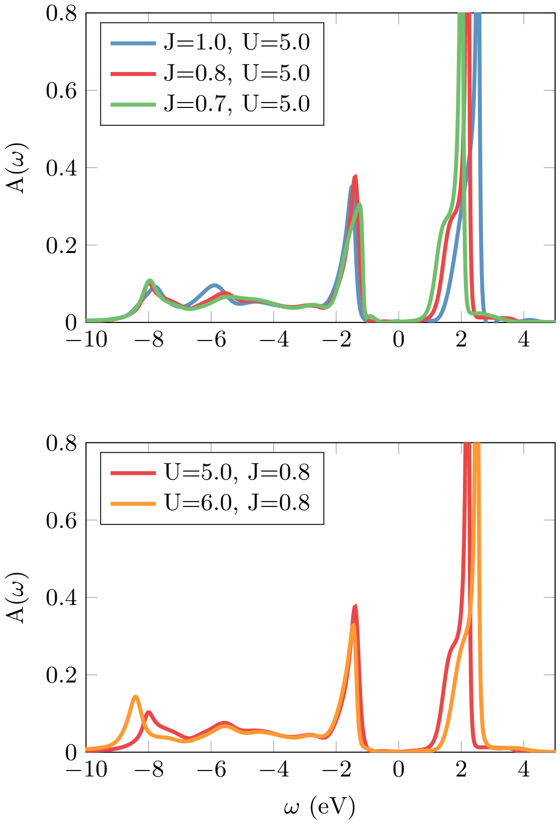

Figure 37: 3-band *d*-*dp* model: spectral functions for different J (top) and different U (bottom). All interaction parameters are given in eV. Upon increasing both parameters the gap increases. Changing J shifts the peak at around $-6.0\,\mathrm{eV}$, while changing U only shifts the one at $-8.0\,\mathrm{eV}$.

is proportional to Hund's coupling J (see Fig. 36). Their position relative to the upper t_{2g} Hubbard band is influenced by the crystal field splitting and J. From this clear atomic-like structure we see that even empty orbitals need to be included in the correlated subspace because of correlation effects with other occupied orbitals.

8.4.2 3-band *d*-*dp* model

In the energy region where the lower Hubbard band is located, we also find t_{2g} weight stemming from the Mn-3d/O-2p hybridization (see middle plot of Fig. 34). This suggests that those states should be included in the construction of the projective Wannier functions, i.e., a *d*-*dp* model. In the following we will use the term High Energy Spectral Weight (HESW) to denote the Wannier function weight on the oxygen bands (located below $-1.5\,\mathrm{eV}$). The first and most obvious consequence of a larger projective energy window is an increased bandwidth of the Wannier DOS. To obtain a similar insulating behavior as in the *d*-only model we increase U and J. Secondly, now also the DC correction has a non-trivial effect, since it shifts the correlated t_{2g} states relative to the oxygen bands. The t_{2g} weight on the oxygen bands is rather small, which means that the effect of the DC correction on the HESW is equally low. Thirdly, in the 3-band *d*-*dp* model the impurity occupation grows (the exact value depending on U and J), changing the character of the ground state to a mix of states with mainly three and four particles on the impurity, while in the 3-band *d*-only calculation the occupation of the impurity was three electrons. Due to the increased complexity of the ground state, we expect a richer dependence of the spectrum on the interaction parameters U and J.

In Fig. 37 we compare calculations for different values of J (top) and different values of U (bottom). Overall, the spectral functions consist of a (smaller) lower Hubbard band connected to states from the hybridized oxygen bands and an upper steeple-like Hubbard band of similar shape as in the *d*-only calculation. By comparing the two peaks at $-6.0\,\mathrm{eV}$ and $-8.0\,\mathrm{eV}$, we observe that they behave differently when changing U or J. While the former is only affected by J, the latter is not, but shifts with U. The resolution of the structure in the lower-Hubbard-band/HESW complex demonstrates the capabilities of the FTPS solver.

The t_{2g} gap grows when increasing either U or J, which is a typical sign of Mott physics at half filling [23]. Nevertheless, in the *d*-*dp* model the gap size increases slowly: when increasing U by $1.0\,\mathrm{eV}$, the gap only grows by about half of that. Considering also the uncorrelated e_g orbitals, we observe that the single-particle gap is not much affected by the interaction values studied. An artificial lowering of the DC correction by $-0.5\,\mathrm{eV}$, which corresponds to a relative shift in energy between the correlated subspace and the uncorrelated states, also increases the t_{2g} gap (Fig. 38). This growth of the gap

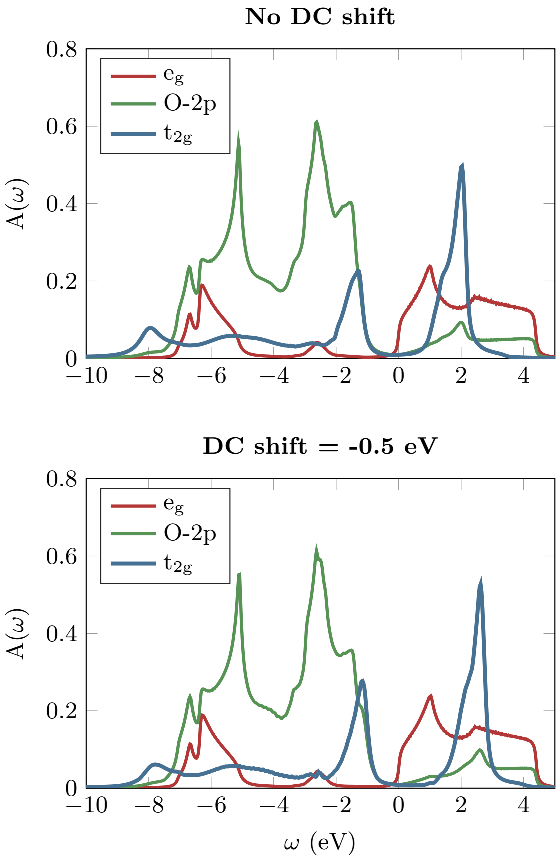

Figure 38: 3-band *d-dp* model: effect of the DC correction. *Top:* FLL DC, *Bottom:* FLL DC with an additional shift of $-0.5\,\mathrm{eV}$. $U = 5.0\,\mathrm{eV}$ and $J = 0.7\,\mathrm{eV}$ are used as interaction parameters. Contrary to all other figures, in this plot we show the spectrum of the correlated local Green's function.

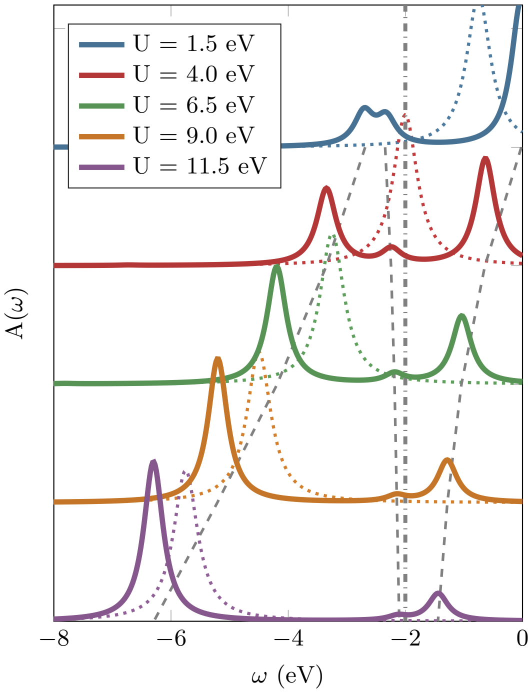

Figure 39: Spectrum of a one-band AIM with one interacting site coupled to a single non-interacting site (Eq. 8.3). The spectrum is calculated with the absolute ground state over all particle number sectors. The on-site energy ϵ_1 is shown as gray dashed-dotted vertical line. The gray dashed lines visualize the evolution of the location of the three peaks as a function of the interaction strength U. The colored dotted peaks show the atomic spectrum with peaks at $-U/2$. The upper Hubbard band (additional peak at $\omega > 0$) is not shown. All spectra have been broadened by $\eta_{FT} = 0.2\,\mathrm{eV}$.

is mostly due to a shift of the t_{2g} upper Hubbard band, since the chemical potential is pinned by the e_g bands. The first excitation below E_F has a mix of t_{2g} and O-p character. This indicates that in this model, $SrMnO_3$ is not a pure Mott insulator, but a mixture between Mott- and charge transfer insulator. This classification is consistent with previous results [139, 140, 142, 144].

Let us employ a simple toy model to qualitatively understand this intermediate regime. We use a correlated site coupled to only one non-interacting site:

$$H = U(n_{0,\uparrow} - 0.5)(n_{0,\downarrow} - 0.5) \\ + \sum_{\sigma} V_1(c^{\dagger}_{0,\sigma} c_{1,\sigma} + h.c.) + \epsilon_1 n_{1,\sigma} \tag{8.3}$$

The purpose of the non-interacting site is to mimic the effect of the HESW. We set the on-site energy to $\epsilon_1 = -2.0\,\mathrm{eV}$ and use a coupling to the impurity of $V_1 = 1.0\,\mathrm{eV}$. Since we want to understand the occupied part of the spectrum, we focus on negative energies only. In Fig. 39 we show the resulting spectral functions ($\omega < 0$) for various values of the interaction strength U (full lines). The atomic excitation spectra of this model (corresponding to $V_1 = 0$), whose peaks are positioned exactly at $-U/2$, are indicated by dotted lines. This toy model shows three important features:
First: The peak highest in energy (above $-2.0\,\mathrm{eV}$) corresponds to the lower Hubbard band for small values of U [26]. We see that it does not cross the on-site energy ϵ_1 with increasing U, but approaches it asymptotically. The bath site *repels* this level and upon increasing U its weight decreases.
Second: The peak lowest in energy shows the opposite behavior. The uncorrelated site repels it towards lower energies and the spectral weight increases when we increase U. For large U this level asymptotically approaches the atomic limit at energy $-U/2$ and eventually becomes the lower Hubbard band. These two peaks together form what one could call a split lower Hubbard band.
Third: The excitation at the on-site energy ϵ_1 shifts to lower energy and splits under the influence of U. Upon increasing U, one part develops into the lower Hubbard band discussed above, and the other approaches ϵ_1 from below, with diminishing weight.
The DMFT spectral functions (Fig. 37) also show roughly a 3-peak structure, where the peaks at about $-1.5\,\mathrm{eV}$ ($-8.0\,\mathrm{eV}$) could be the first (last) peak of the split lower Hubbard band of our toy model. The region in between then

---

[26] If we use a larger bath energy ϵ_1, for example $\epsilon_1 = -5.0\,\mathrm{eV}$, the position of the first peak of the impurity spectrum is proportional to U at small U, showing that it is indeed a lower Hubbard band.

corresponds to the small, middle peak in the toy model stemming from the HESW.

The repulsion of the first peak explains why increasing U (Fig. 37 lower graph) has only a relatively weak effect on the size of the gap. On the other hand, effectively shifting the oxygen bands with the DC correction to lower energies (Fig. 38) corresponds to shifting the bath energy ϵ_1. This means that the repulsion gets weaker, which explains the growth of the gap. Furthermore, when increasing U we find that the peak highest in energy gets smaller, while spectral weight is transferred to the lowest energy peak, which is also shifted to lower energies (Fig. 37). Additionally, a lowering of the DC correction leads to an opposite behavior, where the first peak below E_F grows at the expense of the lowest one in energy. Note that the middle region of our DMFT spectrum shows a J-dependence (Fig. 37 top), which cannot be explained by a one-orbital toy model. Using a similar toy model with two orbitals and Kanamori interaction, we indeed observe a splitting proportional to J in the spectra (not shown here). Since the effect is small we will refrain from discussing it in more depth.

We emphasize that the close relation between the toy model and the actual impurity Green's function of $SrMnO_3$ in the *d*-*dp* model suggests that the HESW has the effect of splitting the lower Hubbard band into two bands; their separation increases with the hybridization strength. Therefore, including the oxygen states in the model strongly influences the size of the gap.

8.4.3 5-band *d*-*dp* model

From the DFT-DOS in Fig. 34, we see that the e_g orbitals are actually not empty. They possess additional spectral weight at around $-7.0\,\text{eV}$, stemming from hybridizations with the oxygen bands. Similarly to the previous section where we included hybridizations of t_{2g} and O-2p, we now also include the hybridizations of e_g and O-2p.

As mentioned at the beginning, only approximations to the DC correction are known. For the present 5-band calculation we find that using the FLL

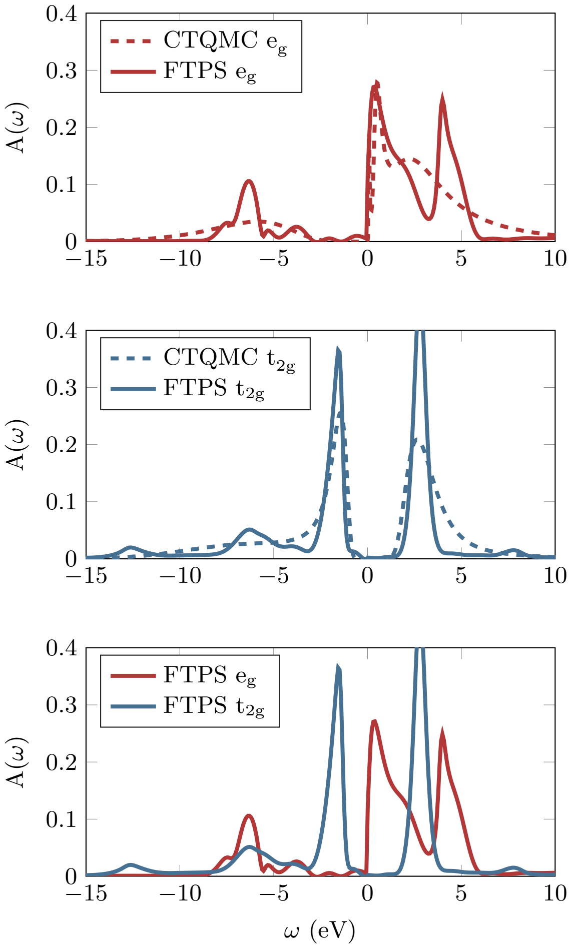

Figure 40: Comparison of the spectral functions for the 5-band *d*-*dp* model between FTPS and CTQMC+MaxEnt. *Top:* e_g orbitals. *Middle:* t_{2g} orbitals. For both calculations we use $U = 6.0\,\text{eV}$ and $J = 0.8\,\text{eV}$. *Bottom:* Combined spectral function.

DC does not produce a pronounced gap. This can be traced back to the additional hybridizations of e_g with O-2p (see discussion below). Furthermore, the FLL formula is based on five degenerate orbitals. In the case at hand we find an approximately half filled t_{2g} impurity ($\langle n_{t_{2g}0\sigma}\rangle \approx 0.5$) and about one electron in total on the e_g part of the impurity ($\langle n_{e_g0\sigma}\rangle \approx 0.2$). One therefore needs to adapt the DC correction to reproduce experimental results. In order to obtain a pronounced gap, we decrease the FLL DC energy by 2.0 eV. Note that it has been argued that very often the FLL-DC is too high [74]. A reduction of the DC can also be accomplished by adjusting U in the FLL formula [75, 144].
Fig. 40 shows the spectral function of the full 5-band d-dp calculation with adjusted DC as well as the respective spectral function obtained by a DMFT calculation using CTQMC+MaxEnt. Overall, the FTPS spectrum is in good agreement with the CTQMC+MaxEnt result. However, FTPS provides a much better energy resolution at high energies, which is especially apparent from the pronounced peak structure in the e_g spectrum. From this comparison we also see that the sharp, step-like shape of the e_g spectrum at E_F is not an artifact of the FTPS solver. We note that for the 5-band calculation presented in Fig. 40, FTPS (720 CPU-h) and CTQMC (600 CPU-h) need similar computational effort for one DMFT iteration [27].
The unoccupied part of the total spectrum (sum of the e_g and t_{2g} spectra shown in the bottom plot of Fig. 40) consists of a three peak structure with alternating e_g -t_{2g} -e_g character, which is much more pronounced than in the 5-band d-only calculation (Fig. 36). Compared to the 3-band d-dp model we find differences mainly in the occupied part of the t_{2g} spectral function (Fig. 42). This is especially apparent in the lowest peak, which seems to be shifted from -9.0 eV to -13.0 eV. Although this high energy excitation is small, the FTPS solver can reliably resolve it.

The differences in the position of this peak are again similar to the behavior of a toy model. Here we use a two-orbital AIM with a single bath site

---

[27] CTQMC used $128 \cdot 10^6$ measurements and the calculations were performed on the same processors: Intel Xeon E5-2650v2, 2.6 GHz with 8 cores.

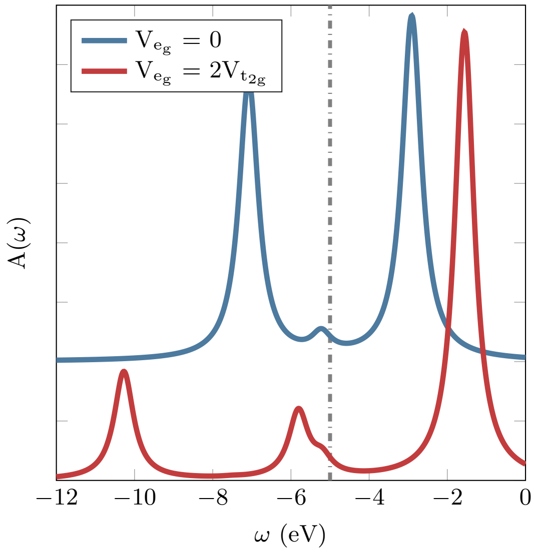

Figure 41: Effect of the e_g hybridizations on the t_{2g} spectrum of the toy model (Eq. 8.4). Parameters (in eV): $U = 10.0$, $J = U/10$, $E_{t_{2g}} = -U/2$, $E_{e_g} = -U/2 + 1.0$, $\epsilon_{t_{2g}} = \epsilon_{e_g} = -5.0$ and $V_{t_{2g}} = 1.5$. The gray dashed dotted line shows the bath energy levels. All spectra have been broadened by $\eta_{FT} = 0.2\,\text{eV}$.

for each orbital:

$$\begin{aligned} H =& H_{\text{int}} + \sum_{m\in(t_{2g},e_g)} E_m n_{0,m} + \\ & \sum_{\sigma} V_m (c^{\dagger}_{0,m,\sigma} c_{1,m,\sigma} + h.c.) + \epsilon_m n_{1,m,\sigma}. \end{aligned} \tag{8.4}$$

For the interaction H_{int} we choose the Kanamori Hamiltonian. As before, we use a single bath site for each orbital to mimic the effect of the HESW. We are interested in the influence of the hybridizations of e_g and O-2p on the t_{2g} spectral function. In Fig. 41, we compare the spectrum without e_g -HESW states ($V_{e_g} = 0$) with the one obtained from $V_{e_g} = 2V_{t_{2g}}$[28]. Although one would expect the e_g hybridization to only have a minor influence on the t_{2g} spectrum, we observe a rather surprising behavior. The additional hy-

---

[28] In the full 5-band calculation, the e_g bath spectral function is much larger than the one for the t_{2g} orbitals in the energy region of the oxygen bands, which we mimic by a factor of 2 in V_{e_g}.

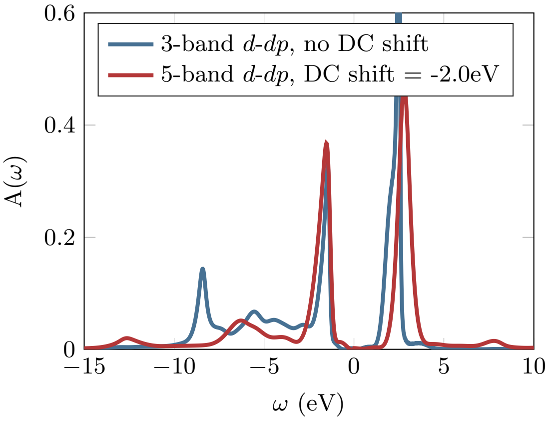

Figure 42: Comparison of the t_{2g} spectral functions of the 3-band *d-dp* and 5-band *d-dp* calculations at $U = 6.0\,\text{eV}$ and $J = 0.8\,\text{eV}$, taken from Figs. 37 and 40. In the 5-band calculation we shifted the double counting by $-2.0\,\text{eV}$ to increase the gap. The influence of the number of bands is most apparent in the high-energy features. The increased repulsion of the first peak of the lower-Hubbard-band/oxygen complex (Fig. 41) makes a shift in the DC necessary, if the single particle gap should remain the same.

bridization leads to a stronger repulsion of the lowest energy peak from the bath energy, qualitatively explaining the shift from $-9.0\,\text{eV}$ to $-13.0\,\text{eV}$ in Fig. 42.

Additionally, this toy model provides an explanation for the necessary adjustment of the DC correction in the 5-band calculation: The peak highest in energy in Fig. 41 is repelled more strongly with the additional e_g hybridizations, therefore the gap decreases. If we would want to obtain a similar t_{2g} gap as with $V_{e_g} = 0$, the interaction in the toy model would need to be increased to $U \approx 20\,\text{eV}$ (keeping $J = U/10$). Since this is unphysical, the only other option is to shift the bath site energies of the toy model. In the DMFT calculation this corresponds to a shift in the DC correction, effectively shifting the HESW to lower energies. This behavior can be observed in Fig. 42, where we compare the spectra of the 3- and 5-band *d-dp* models. The onset of the lower-Hubbard-band/HESW complex is exactly at the same position in both spectra, although the DC shift differs by $2.0\,\text{eV}$.

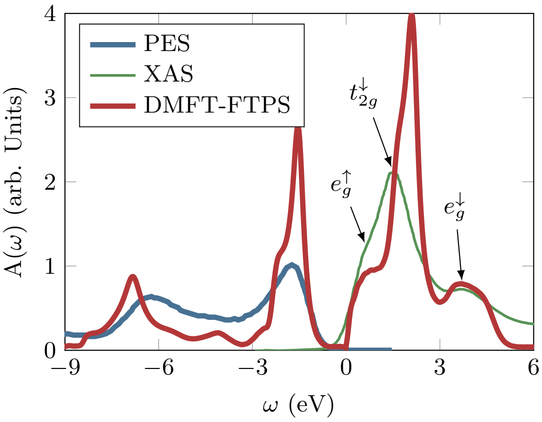

Figure 43: Photo Emission Spectroscopy (PES) and X-ray Absorption Spectroscopy (XAS) compared to the 5-band *d-dp* DMFT-FTPS results ($U = 5.0\,\mathrm{eV}$ and $J = 0.6\,\mathrm{eV}$). The experimental curves are reproduced from Ref. [143], Fig. 5. We normalized the experimental curves to $\int_{-9}^{0} A_{\mathrm{PES}} d\omega = \int_{-9}^{0} A_{\mathrm{FTPS}} d\omega$ and $\int_{0}^{6} A_{\mathrm{XAS}} d\omega = \int_{0}^{6} A_{\mathrm{FTPS}} d\omega$. FTPS as well as the experiments show a 3-peak structure of alternating e_g - t_{2g} - e_g character in the unoccupied part of the spectrum (indicated by arrows). For the arrow labels we adopted the notation of Ref. [143], where $e_g^{\uparrow}$ means an excitation into the e_g spectrum with majority spin, while $t_{2g}^{\downarrow}$ and $e_g^{\downarrow}$ are excitations into the t_{2g} and e_g spectrum with minority spin (see also Eq. 8.2).

8.5 Comparison to experiment

Equipped with a good understanding of the model-dependent effects on the spectral function, we are finally in a position to compare our results to experiments. Several studies concluded that the unoccupied part of the spectrum consists of three peaks with alternating e_g - t_{2g} - e_g character [141–143]. As we have shown, with DMFT+FTPS we are able to resolve such a structure when including the e_g states as correlated orbitals in a genuine 5-band model. Additionally, we need to choose the energy window, i.e., whether the HESW should be included in the construction of the projective Wannier functions. The nature of the insulating state (Mott or charge transfer) has been debated in the literature [139, 140, 142, 144], but it is likely that $SrMnO_3$ falls in an intermediate regime where a clear distinction is difficult. In the present work we have come to the same conclusion. This implies that the lower Hubbard band and the O-2p bands are not separated in energy, which favors the use of a *d*-*dp* model. We therefore conclude that a 5-band *d*-*dp* model is necessary to fully capture the low-energy physics of $SrMnO_3$.

Having decided on the model for the correlated subspace, we still need to determine the interaction parameters U and J as well as the DC. To do so we use PES and XAS data for the Mn-3d orbitals obtained by Kim *et al.* [143] and compare to our total impurity spectrum ($6A_{t_{2g}}(\omega) + 4A_{e_g}(\omega)$ from Fig. 40). According to Ref. [143], the XAS (PES) spectrum can be considered to represent the unoccupied (occupied) Mn-3d spectrum. In the measured spectrum the chemical potential is in the middle of the gap. In all our calculations, the chemical potential is determined by the onset of the unoccupied e_g spectrum. However, the absolute position in energy is not exactly known in XAS [149]. Our calculation is in good agreement with the experiment when we use a rigid shift of the XAS spectrum by $0.8\,\mathrm{eV}$ to lower energies. Additionally, we deduce from the peak positions in the experiment that the interaction parameters used for the calculations presented in Fig. 40 are too high. The separation of the two e_g peaks ($\sim J$) and also the relative position of the t_{2g} upper Hubbard band is different than in the experiment. Therefore, we decrease the interaction parameters to $U = 5.0\,\mathrm{eV}$

and $J = 0.6\,\mathrm{eV}$ but keep the static shift of the FLL DC by $-2.0\,\mathrm{eV}$. Note that these parameters are similar to the ones used in other DFT+DMFT studies on $SrMnO_3$ [144, 145].

The resulting spectral function for the new set of parameters is compared to the experimental spectrum in Fig. 43. Notably, the bandwidths of both, the unoccupied and the occupied spectrum, agree very well with the experiment. The unoccupied part of the experimental spectrum (XAS) shows that the first e_g peak is just a shoulder of the t_{2g} upper Hubbard band, and that the separation of the two e_g peaks is about $3.2\,\mathrm{eV}$, which is in agreement with our result. Since this separation is proportional to the Hund's coupling, we conclude that $J \approx 0.6\,\mathrm{eV}$ for this compound. The t_{2g} upper Hubbard band at $2.0\,\mathrm{eV}$ is still slightly too high in energy.

The experiment also shows a lower-Hubbard-band/oxygen complex with two main peaks at about $-6.0\,\mathrm{eV}$ and $-2.0\,\mathrm{eV}$. As discussed in the previous sections (bottom plot of Fig. 40), our results identify the first peak at $-2.0\,\mathrm{eV}$ to have mainly t_{2g} character and to correspond to the largest part of the split lower Hubbard band, whereas the second peak at $-6.0\,\mathrm{eV}$ has both e_g and t_{2g} character and stems from the hybridizations with the oxygen bands. We note that the region between these two peaks has larger spectral weight in the experiment than in our calculations. Importantly, no prominent spectral features are observed in the experiment around $-8.0\,\mathrm{eV}$, strengthening our conclusion that the 3-band *d*-*dp* model is not sufficient to describe the experiment (see also Fig. 42).

8.6 Conclusions

We have studied the influence of the choice of the correlated subspace, i.e. the number of bands and the energy window, on the DFT+DMFT result for the strongly correlated compound $SrMnO_3$. For *d*-only models (neglecting *p*-*d* hybridizations), we have shown that the empty e_g orbitals should be included in the correlated subspace because interactions with the half-filled t_{2g} bands affect the spectrum, leading to a multiplet structure and a broadening of the e_g DFT-DOS. Including the Mn-3*d*/O-2*p* hybridizations in a

3-band model for the t_{2g} bands only, i.e., the 3-band d-dp model, we found a situation similar to avoided crossing, which leads to an interesting interplay of atomic physics (lower Hubbard band) and Mn-d/O-p hybridizations. In $SrMnO_3$, the lower Hubbard band hybridizes with the t_{2g} Wannier-weight on the oxygen bands, giving rise to a spectrum that can be approximated by three peaks. This result provides new perspectives on an intermediate regime, where both Mott and charge transfer physics are found. By performing a 5-band calculation including the p-d hybridization, we investigated the effect of the e_g hybridization on the t_{2g} spectrum. The splitting due to avoided crossing is heavily increased, which strongly affects the 3-peak structure and also decreases the gap. Equipped with a good understanding of the different correlated subspaces and the effects of the model parameters (U, J, DC) we were able to obtain a spectral function in good agreement with experimental data. We conclude that the choice of a suitable model for the correlated subspace is important, since the inclusion of both the O-$2p$ hybridizations and the e_g states is essential for a correct description of the observed spectral function in $SrMnO_3$.
Finally, we would also like to stress that we have shown that FTPS is a viable real-time impurity solver for real material calculations with five bands.

Acknowledgments

The authors acknowledge financial support by the Austrian Science Fund (FWF) through SFB ViCoM F41 (P04 and P03), through project P26220, and through the START program Y746, as well as by NAWI-Graz. This research was supported in part by the National Science Foundation under Grant No. NSF PHY-1125915. We thank J.-S. Kang for the permission to reproduce data and for helpful suggestions. We are grateful for stimulating discussions with J. Mravlje, F. Maislinger and G. Kraberger. The computational resources have been provided by the Vienna Scientific Cluster (VSC). All calculations involving tensor networks were performed using the ITensor library [150].

9 Conclusions

In the present thesis, we have introduced an Fork Tensor Product States (FTPS) tensor network that can be used as a real-frequency impurity solver for Dynamical Mean Field Theory (DMFT). The fork-like geometry of an FTPS resembles the geometry of the Hamiltonian of a multi-orbital AIM. It allows us to represent the bath with high accuracy by employing a large number of bath sites. Although FTPS are more involved than Matrix Product States (MPS), they share one important similarity. The graphs of both tensor networks are loop-free, allowing us to find Schmidt decompositions for each bond-index. This in turn allows us to truncate the tensor network in a controlled way and to find efficient representations of quantum mechanical states. Therefore, the theory of how to use FTPS is largely based on MPS, discussed in detail in Sec. 4.

In Sec. 5 we showed how to use MPS for impurity models for a single orbital. We emphasized that it is favorable to use the so called star geometry of the bath in which the impurity is coupled to all bath sites in a star-like manner (see Fig, 1). Although such long-range hopping terms seem to be incompatible with MPS, we have shown how to efficiently encode the Hamiltonian as a Matrix Product Operator (MPO) and how to time evolve using swap-gates. Then we set the stage for the FTPS-tensor network by discussing one possible reason of why MPS fail for multi-orbital models: AIMs usually do not couple bath degrees of freedom of different orbitals directly with each other. Instead of combining these separated bath sites into one super-site in the MPS, FTPS keep bath tensors of different spin and orbital degrees of freedom separated. In Sec. 6, we discussed the tensor network thus obtained. Since FTPS are loop-free, we were able to show how to obtain the Schmidt decomposition for each bond of the tensor network. Then, we explained how to to find ground states using DMRG and how to time evolve in star geometry using the results of Sec. 5 as a starting point. This allows us to calculate Green's functions (self energies) on the real frequency axis, enabling us to use FTPS as a real-frequency solver for DMFT.

In Sec. 7 we used this approach for the typical benchmark compound

$SrVO_3$. We described its low energy subspace by a three-orbital model for the t_{2g} bands of the V-3d shell. We found that FTPS agrees very well with Continuous Time Quantum Monte Carlo (CTQMC) on the imaginary frequency axis (where CTQMC is statistically exact), but shows significant differences for real frequencies. The reason for this is the ill-posed analytic continuation required to transform imaginary-time Green's functions to real-energy spectra in CTQMC (see Fig. 28). On the real frequency axis, the FTPS impurity spectral function shows a distinct three-peak structure in the upper Hubbard band. The position of these three peaks depends on whether we use the full Kanamori interaction or neglect the spin-flip and pair-hopping terms. We found that the origin of these peaks are atomic excitations of the local part of the AIM-Hamiltonian H_{loc} (as also discussed in Sec. 2) with effective interaction parameters U and J.

Finally, in Sec. 8 we used the FTPS solver for the compound $SrMnO_3$. It has a half-filled Mn 3d-shell, and therefore tends to become Mott-insulating. This is exactly what we found when using only the t_{2g} bands for the correlated subspace in a three-band model. Since the t_{2g} lower Hubbard band is in close proximity (in energy) to hybridizations of the t_{2g} bands with oxygen p-bands, we found that it is necessary to include these hybridizations, resulting in a so called dp-model. Indeed, including hybridizations, we found that the spectral function changes considerably giving rise to an intermediate regime between Mott- and charge transfer insulator. Not only hybridizations play a crucial role in $SrMnO_3$, but also the e_g bands are important, although they appear to be mostly empty at a first glance. Performing DMFT for the full 3d-shell (t_{2g} - as well as e_g -bands) in a five band model showed that FTPS is a viable impurity solver for real material calculations for at least five bands. We compared the spectrum of this five band calculation (including hybridizations) to XAS and PES experiments and found very good agreement. Notably the XAS measurement shows a three-peak structure of alternating e_g -t_{2g} -e_g character. The spectrum of the FTPS solver has the same three peaks, showing the importance of a real-frequency solver in describing strongly correlated materials (see Fig. 43).

As far as future developments are concerned, I can think of three important directions. First, throughout this work, we used the star geometry representation of the bath. With FTPS the bath sites are already separated in the tensor network and operations on the bath tensors are computationally cheap. Although star geometry seems to be far superior (see Fig. 13), chain geometry might show better convergence in the DMRG [29]. Second, it would be interesting to try to use FTPS for finite temperature calculations, for example employing the purification method [17]. This would only need a local doubling of the Hilbert space which should not be an issue, since it already has the smallest possible value ($d = 2$). Third, so far, FTPS can only treat diagonal hybridizations of the impurity with its bath. Lattice distortions, for example, introduce off-diagonal terms though. It is possible to represent such off-diagonal terms by only coupling bath sites to impurity sites, which should allow FTPS to be a good representation of quantum mechanical states. Although we can find an FTPO for such terms, the time evolution is more challenging. The TDVP or Krylov-space based methods would allow time evolution using only the Hamiltonian and hence might be an interesting future development. If successful, this would allow FTPS to treat the most general case of an AIM describing the full $3d$-shell in the presence of lattice distortions or spin-orbit coupling at zero temperature.

---

[29] The transformation from star- to chain geometry is a unitary transformation only acting on the bath degrees of freedom. Therefore, this can only change the bond dimensions of the bath tensors.

A Swap Gates

In this appendix we prove that swap gates S_{ij} change the ordering of sites in a tensor network. We assume $i < j$ in the fermionic order such that $A \otimes B$ means that operator A acts on site i and operator B acts on site j. To do this it suffices to show that:

$$S^{ij}\left(A_k \otimes B_l\right) S^{ij} = \xi\left(B_l \otimes A_k\right) \tag{A.1}$$

for a complete basis of operators A_k and B_l. $\xi = -1$ if A_k and B_l anti-commute and $\xi = 1$ otherwise. In the present the the case $\xi = -1$ is never needed, since if a term $c_i^\dagger c_j$ appears we apply it before we swap. Eq. A.1 means that swapping first, applying $A_k \otimes B_l$ and swapping back has, up to a sign, the same effect as applying $B_l \otimes A_k$. The operator basis we choose is $\mathbb{1}$, $n = c^\dagger c$, $c^\dagger$ and c. The basis for the vectors is the standard particle number basis for which the swap gate has matrix representation:

$$S^{ij} = \begin{array}{c} \begin{array}{cccc} |0,0\rangle & |0,1\rangle & |1,0\rangle & |1,1\rangle \end{array} \\ \begin{pmatrix} 1 & 0 & 0 & 0 \\ 0 & 0 & 1 & 0 \\ 0 & 1 & 0 & 0 \\ 0 & 0 & 0 & -1 \end{pmatrix} \end{array} \tag{A.2}$$

The minus sign in the last entry is due to the fermionic sign when two fermions swap their places. Calculating all 16 possible combinations is a tedious but straight forward linear algebra exercise that will be left to the reader. Only note that the swap gate takes already care of the fermionic sign. For example: $S_{ij}\left(c \otimes \mathbb{1}\right) S_{ij} = p \otimes c$, with $p = (-1)^n$.

It is also instructive to look at the matrix representation of some operator O

in bra-ket notation:

$$O = \begin{pmatrix} \langle 0,0|O|0,0\rangle & \langle 0,0|O|0,1\rangle & \langle 0,0|O|1,0\rangle & \langle 0,0|O|1,1\rangle \\ \langle 0,1|O|0,0\rangle & \langle 0,1|O|0,1\rangle & \langle 0,1|O|1,0\rangle & \langle 0,1|O|1,1\rangle \\ \langle 1,0|O|0,0\rangle & \langle 1,0|O|0,1\rangle & \langle 1,0|O|1,0\rangle & \langle 1,0|O|1,1\rangle \\ \langle 1,1|O|0,0\rangle & \langle 1,1|O|0,1\rangle & \langle 1,1|O|1,0\rangle & \langle 1,1|O|1,1\rangle \end{pmatrix}. \tag{A.3}$$

Then we find for the transformed operator:

$$S^{ij}OS^{ij} = \begin{pmatrix} \langle 0,0|O|0,0\rangle & \langle 0,0|O|1,0\rangle & \langle 0,0|O|0,1\rangle & -(-1)\langle 0,0|O|1,1\rangle \\ \langle 1,0|O|0,0\rangle & \langle 1,0|O|1,0\rangle & (-1)\langle 1,0|O|0,1\rangle & -\langle 1,0|O|1,1\rangle \\ \langle 0,1|O|0,0\rangle & (-1)\langle 0,1|O|1,0\rangle & \langle 0,1|O|0,1\rangle & -\langle 0,1|O|1,1\rangle \\ -(-1)\langle 1,1|O|0,0\rangle & -\langle 1,1|O|1,0\rangle & -\langle 1,1|O|0,1\rangle & \langle 1,1|O|1,1\rangle \end{pmatrix}.$$

The (-1) are the $\xi = -1$ in Eq. A.1 for the four pairs of $c^\dagger c^\dagger$, $c^\dagger c$, $cc^\dagger$ and cc. We see that in the bra- as well as in the ket vector the entries are swapped and we get a minus sign if 2 particles are moved past each other. This behavior is exactly what we expect from swap gates. To obtain a better understanding of the basis transformation from applying swap gates, let us take a look at a few examples. First, for the operator $c_i^\dagger c_j$ $(i < j)$ with only one non-zero matrix element:

$$\begin{aligned} \langle 10|\, c_i^\dagger c_j \,|01\rangle &= 1 \\ \underbrace{\langle 10|\, S^{ij}}_{\langle 01|}\, \underbrace{S^{ij} c_i^\dagger c_j S^{ij}}_{\xi c_i c_j^\dagger}\, \underbrace{S^{ij}\,|01\rangle}_{|10\rangle} &= 1 \\ \langle 01| - \xi c_j^\dagger c_i \,|10\rangle &= 1 \\ \xi(-1) &= 1 \rightarrow \xi = -1. \end{aligned}$$

In the second line we used $(S^{ij})^2 = 1$. This confirms that we need to use $\xi = -1$ for anti-commuting operators. As a different example let us look at the operator $c_i n_j$, for which we should use $\xi = 1$ according to Eq. A.1:

$$\begin{aligned}
\langle 01| \, c_i n_j \, |11\rangle &= 1 \\
\underbrace{\langle 01| \, S^{ij}}_{\langle 10|} \, \underbrace{S^{ij} c_i n_j S^{ij}}_{n_i c_j} \, \underbrace{S^{ij} \, |11\rangle}_{-|11\rangle} &= 1 \\
-\langle 10| \, n_i c_j \, |11\rangle &= 1 \\
1 &= 1.
\end{aligned}$$

Indeed, for commuting operators the $\xi = 1$ choice is correct. In the last example we show how a hopping term $t c_i^\dagger c_j - t^* c_i c_j^\dagger$ ($i < j$ in the fermionic order) transforms under swap gates.

$$\begin{aligned}
& S^{ij} \left(t c_i^\dagger c_j - t^* c_i c_j^\dagger \right) S^{ij} \\
= \; & t S^{ij} c_i^\dagger c_j S^{ij} - t^* S^{ij} c_i c_j^\dagger S^{ij} \\
= \; & -t c_i c_j^\dagger + t^* c_i^\dagger c_j \\
= \; & t^* c_i^\dagger c_j - t c_i c_j^\dagger.
\end{aligned}$$

This shows that for hopping terms, a swap results in complex conjugation of the amplitude t. Therefore, when using swap gates, one must be very careful with the fermionic sign. In the present thesis, we circumvent this difficulty by applying hopping terms always *before* the application of the swap gate.

B Error Estimates of Suzuki Trotter Decompositions

In this appendix we discuss the error of the second order Suzuki Trotter decompositions of AIMs with respect to the number of bath sites N_b for the star geometry as well as for the chain geometry. Since we use a second order breakup, differences occur in the third order of the series expansion and a single breakup separating operators A and B is given by

$$e^{-i(A+B)\Delta t} = e^{-i\frac{\Delta t}{2}A}e^{-i\Delta t B}e^{-i\frac{\Delta t}{2}A} + \mathcal{O}\Big((\Delta t)^3\big([A,[A,B]] + [B,[A,B]]\big)\Big). \tag{B.1}$$

The influence of the number of bath sites is encoded in the double commutators. Therefore let us analyze them for the two geometries. In the chain geometry (a nearest neighbor tight binding chain), we use a standard even-odd breakup [17], i.e. $A = H_{\text{even}}$ and $B = H_{\text{odd}}$. The commutator $[A, B]$ is of order $\mathcal{O}(N_b)$, since each term in A does not commute with at maximum two terms in B. For the double commutators $[A,[A,B]]$ and $[B,[A,B]]$ this means, both are of order $\mathcal{O}(N_b^{)}$.

For star geometry, the situation is a bit more involved (see Eq. 5.11). To proceed, we first calculate the commutator of two different hopping terms (omitting the amplitudes V in the following):

$$H_{k\to l} = [H_{k\sigma}, H_{l\sigma}] = c_k^\dagger c_l - c_l^\dagger c_k. \tag{B.2}$$

The first step of the breakup in Eq. 5.11 separates $H_{N_b\sigma}$ from the hoppings to all other sites, i.e. $A = H_{N_b\sigma}$, $B = \sum_{k<N_b} H_{k\sigma}$ (from now on omitting the

spin index σ). We find:

$$\begin{aligned}
[A, B] &= \sum_{k<N_b} [H_{N_b}, H_k] = \sum_{k<N_b} H_{N_b \to k} \\
[A, [A, B]] &= \sum_{k<N_b} [H_{N_b}, H_{N_b \to k}] = \mathcal{O}(N_b) \\
[B, [A, B]] &= \sum_{k,k'<N_b} \underbrace{[H_{k'}, H_{N_b \to k}]}_{\sim \delta_{k,k'}} = \mathcal{O}(N_b).
\end{aligned} \tag{B.3}$$

And we see that the error of the first step scales with $\mathcal{O}(N_b)$. In the second step, we separate H_{N_b-1} from all remaining terms with index $k < N_b - 1$. Using the same arguments as before, we find that the error of this step scales as $\mathcal{O}(N_b - 1)$, since the number of sites in the remaining terms decreased by one. Iterating this, we find that the total breakup given in Eq. 5.11 has an error of the order of:

$$\mathcal{O}(N_b) + \mathcal{O}(N_b - 1) + \mathcal{O}(N_b - 2) + \cdots + \mathcal{O}(1) = \mathcal{O}(N_b^2). \tag{B.4}$$

This proves that the error of the breakup we use for the star geometry (Eq. 5.11) has at most a scaling of N_b^2. Although this suggests that chain geometry should be superior for large baths, the results presented in Fig. 13 show that the error in star geometry does not seem to scale with bath size. We leave this very curios finding for future investigations.

C FTPO for Multi-Orbital AIM

In this appendix we construct the FTPO of a multi-orbital AIM with Kanamori interaction (see Eq. 2.10 and Eq. 2.11). The construction is valid for any number of orbitals, since we find repeating matrices. Not included are for example hopping terms First, we need to choose the fermionic order. Every basis state in Fock space is given by:

$$\left(c_1^\dagger\right)^{n_1}\left(c_2^\dagger\right)^{n_2}\cdots\left(c_N^\dagger\right)^{n_N}|0\rangle, \tag{C.1}$$

where Fig. 21 shows the labels $1\cdots N$ for each site. The spin-flip and pair-hopping terms can be written as

$$\begin{aligned} Jc^\dagger_{m\uparrow}c_{m\downarrow}c_{n\uparrow}c^\dagger_{n\downarrow} + Jc_{m\uparrow}c^\dagger_{m\downarrow}c^\dagger_{n\uparrow}c_{n\downarrow} + \\ (-J)c^\dagger_{m\uparrow}c^\dagger_{m\downarrow}c_{n\uparrow}c_{n\downarrow} + (-J)c_{m\uparrow}c_{m\downarrow}c^\dagger_{n\uparrow}c^\dagger_{n\downarrow}, \end{aligned} \tag{C.2}$$

for any pair (m, n). The bath tensors we use are nearly the same that as in Eq. 5.7. The only difference is that all spin-up baths need to carry an additional Fermi-sign operator p to encode the spin-flip and pair-hopping terms. Hence, the bath FTPO tensors are given by:

$$W_1^\uparrow = \begin{pmatrix} \epsilon_1 n_1 \\ I \\ p \\ V_1 c_1 \\ V_1 c_1^\dagger \end{pmatrix}_B \quad , \quad W_1^\downarrow = \begin{pmatrix} \epsilon_1 n_1 \\ I \\ V_1 c_1 \\ V_1 c_1^\dagger \end{pmatrix}_B$$

$$W_k^\uparrow = \begin{pmatrix} I & \epsilon_k n_k & 0 & 0 & 0 \\ 0 & I & 0 & 0 & 0 \\ 0 & 0 & p & 0 & 0 \\ 0 & V_k c_k & 0 & p & 0 \\ 0 & V_k c_k^\dagger & 0 & 0 & p \end{pmatrix}_B \quad , \quad W_k^\downarrow = \begin{pmatrix} I & \epsilon_k n_k & 0 & 0 \\ 0 & I & 0 & 0 \\ 0 & V_k c_k & p & 0 \\ 0 & V_k c_k^\dagger & 0 & p \end{pmatrix}_B . \tag{C.3}$$

Above, we introduced a small subscript B to indicate that the matrix indices correspond to bath-indices. Similarly, we will later use a subscript I to denote for impurity-impurity indices. Multiplying these FTPO tensors, we obtain for each spin-up and spin-down arm:

$$\prod_{k=1}^{N_b} W_k^{\uparrow} = \begin{pmatrix} \sum_k \epsilon_k n_k \\ I \\ p \\ \sum_k V_k c_k \\ \sum_k V_k c_k^{\dagger} \end{pmatrix}_B \quad , \qquad \prod_{k=1}^{N_b} W_k^{\downarrow} = \begin{pmatrix} \sum_k \epsilon_k n_k \\ I \\ \sum_k V_k c_k \\ \sum_k V_k c_k^{\dagger} \end{pmatrix}_B \quad . \tag{C.4}$$

The bath parameters ϵ_k and V_k can be orbital and spin-dependent, but we omit the indices for notational simplicity. The spin-up matrices have an additional entry with a p-operator that will be used exclusively for the spin-flip and pair-hopping terms (note our choice of fermionic order). The vector index of the tensors for bath m above, is the FTPO bond index connecting the impurity to the bath tensor of bath m (for example tensor 6 and 7 in Fig. 21).

Let us continue with the impurity tensors. Since some of the impurity tensors have 3 indices, we introduce a new convention to be able to write them down. For the bond indices connecting impurity tensors we use matrix indices. Additionally, we find that most entries in these matrices need only a single operator from the bath, i.e.:, the identity I or the Fermi-operator p. Therefore, for any local operator O acting on an impurity orbital, we use the notation $O(k)$ to mean that this operator connects to the k-th entry of the bath tensor. For example for the Hubbard terms $Un_{\uparrow}n_{\downarrow}$ we need identity operators from the bath. Therefore, in the FTPO tensors we write $n_{\uparrow}(2)$ to abbreviate:

$$n_{\uparrow}(2) = \begin{pmatrix} 0 \\ n_{\uparrow} \\ 0 \\ 0 \\ 0 \end{pmatrix}_B \quad , \tag{C.5}$$

where the vector index of this tensor corresponds to the bond index connecting the impurity to the bath and $n_\uparrow$ thus multiplies the identity operator in Eq. C.4. The impurity FTPO-tensor then is a matrix of such entries. To connect the non-trivial terms of the bath with the impurity it is convenient to define the following vectors in the sense of Eq. C.5 on the spin-up and spin-down impurities:

$$H_{IB}^{\uparrow} = \begin{pmatrix} I \\ \epsilon_0 n \\ 0 \\ c^\dagger \\ c \end{pmatrix}_B \qquad , \qquad H_{IB}^{\downarrow} = \begin{pmatrix} I \\ \epsilon_0 n \\ c^\dagger \\ c \end{pmatrix}_B \qquad . \tag{C.6}$$

We note that the on-site energy ϵ_0 can be orbital and even spin dependent, but we omit indices for notational simplicity. For the sake of concreteness we will use $A, B \cdots E$ to denote 5 different orbitals, but remember that the following construction is valid for any number of orbitals. With this the first FTPO tensor for orbital A with spin-up is given by:

$$W_{A\uparrow} = \begin{pmatrix} H_{IB}^{\uparrow} \\ I(2) \\ n_{A\uparrow}(2) \\ c_{A\uparrow}^\dagger p(3) \\ c_{A\uparrow} p(3) \end{pmatrix}_I \quad . \tag{C.7}$$

Expressions like $c_{A\uparrow}^\dagger p(3) = (c_{A\uparrow}^\dagger p)(3)$ mean, that the local operator we use is $c_{A\uparrow}^\dagger p$ and that it connects to the third bath index, the string of p-operators in this case (see Eq. C.4). From here on out, all vector/matrix indices of the tensors correspond to impurity-impurity links. Hence, the vector index above corresponds to the bond connecting site 1 and 6 in Fig. 21. Note that the annihilation operator $c_{A\uparrow}$ does not commute with p. Therefore, it is important to let p act before annihilation. Also note that $c_{A\uparrow}^\dagger p = c_{A\uparrow}^\dagger$, but we keep writing it for consistency reasons. For the second impurity tensor we find the 5 × 8 matrix:

$$W_{A\downarrow} = \begin{pmatrix} I(2) & H_{IB}^{\downarrow} & U n_{A\downarrow}(2) & . & . \\ . & I(2) & . & . & . \\ . & . & I(2) & . & . \\ . & n_{A_\downarrow}(2) & . & . & . \\ . & . & . & c_{A\downarrow}(2) & . \\ . & . & . & c_{A\downarrow}^{\dagger}(2) & . \\ . & . & . & . & c_{A\downarrow}^{\dagger}(2) \\ . & . & . & . & c_{A\downarrow}(2) \end{pmatrix}_I . \qquad \text{(C.8)}$$

For orbital $B\uparrow$ the FTPO tensor is given by the 8 × 13 matrix:

$$W_{B\uparrow} = \begin{pmatrix} I(2) & H_{IB}^{\uparrow} & (U' - J)\, n_{B\uparrow}(2) & U' n_{B\uparrow}(2) & . & . & . & . \\ . & I(2) & . & . & . & . & . & . \\ . & . & I(2) & . & . & . & . & . \\ . & . & . & I(2) & . & . & . & . \\ . & n_{B\uparrow}(2) & . & . & . & . & . & . \\ . & . & . & . & I(2) & . & . & . \\ . & . & . & . & . & I(2) & . & . \\ . & . & . & . & . & . & I(2) & . \\ . & . & . & . & . & . & . & I(2) \\ . & c_{B\uparrow}^{\dagger} p(3) & . & . & . & . & . & . \\ . & c_{B\uparrow} p(3) & . & . & . & . & . & . \\ . & . & . & . & c_{B\uparrow} p(3) & . & . & . \\ . & . & . & . & . & c_{B\uparrow} p(3) & . & . \\ . & . & . & . & . & . & c_{B\uparrow}^{\dagger} p(3) & . \\ . & . & . & . & . & . & . & c_{B\uparrow}^{\dagger} p(3) \end{pmatrix}_I . \qquad \text{(C.9)}$$

The tensor for orbital $B\downarrow$ is a 13×8 matrix:

$$W_{B\downarrow} = \begin{pmatrix} I & H_{IB}^{\downarrow} & U' n_{B\downarrow} & (U'-J)\, n_{B\downarrow} & U n_{B\downarrow} & . & . & . & . & . & . & J c_{B\downarrow}^{\dagger} & -J c_{B\downarrow} & J c_{B\downarrow} & -J c_{B\downarrow}^{\dagger} \\ . & I & . & . & . & . & . & . & . & . & . & . & . & . & . \\ . & . & I & . & I & . & . & . & . & . & . & . & . & . & . \\ . & n_{B\downarrow} & . & I & . & . & . & . & . & . & . & . & . & . & . \\ . & . & . & . & . & I & . & . & . & c_{B\downarrow} & . & . & . & . & . \\ . & . & . & . & . & . & I & . & . & c_{B\downarrow}^{\dagger} & . & . & . & . & . \\ . & . & . & . & . & . & . & I & . & . & c_{B\downarrow}^{\dagger} & . & . & . & . \\ . & . & . & . & . & . & . & . & I & . & c_{B\downarrow} & . & . & . & . \end{pmatrix}_I . \tag{C.10}$$

To fit this matrix on one page we omit the bath index of all operators. Except for $H_{IB}^{\downarrow}$, every term is connected to the second entry of the bath tensor i.e.: $J c_{B\downarrow} = J c_{B\downarrow}(2)$.

It turns out that we can repeat the two tensors in Eq. C.9 and Eq. C.10 for all orbitals except the last one, orbital E in our example. Their tensors are very similar to Eq. C.9 and Eq. C.10, but not all entries are needed anymore, so that $W_{E\uparrow}$ is only 8×8-dimensional:

$$W_{E\uparrow} = \begin{pmatrix} I(2) & H_{IB}^{\uparrow} & (U'-J)\,n_{E\uparrow}(2) & U'n_{E\uparrow}(2) & . & . & . & . \\ . & I(2) & . & . & . & . & . & . \\ . & . & I(2) & . & . & . & . & . \\ . & . & . & I(2) & . & . & . & . \\ . & n_{E\uparrow}(2) & . & . & . & . & . & . \\ . & . & . & . & c_{E\uparrow}p(3) & . & . & . \\ . & . & . & . & . & c_{E\uparrow}p(3) & . & . \\ . & . & . & . & . & . & c_{E\uparrow}^{\dagger}p(3) & . \\ . & . & . & . & . & . & . & c_{B\uparrow}^{\dagger}p(3) \end{pmatrix}_I$$

$$W_{E\downarrow} = \begin{pmatrix} I & H_{IB}^{\downarrow} & U'n_{E\downarrow} & (U'-J)\,n_{E\downarrow} & Un_{E\downarrow} & Jc_{E\downarrow}^{\dagger} & -Jc_{E\downarrow} & Jc_{E\downarrow} & -Jc_{E\downarrow}^{\dagger} \end{pmatrix}_I . \tag{C.11}$$

Again, each operator (except $H_{IB}^{\downarrow}$) in $W_{E\downarrow}$ connects to the second bath index i.e.: $Jc_{E\downarrow} = Jc_{E\downarrow}(2)$.

D FTPO for Time Evolution of Spin-Flip and Pair-Hopping Terms

In this appendix we construct the FTPOs to time evolve the spin-flip and pair-hopping terms of the Kanamori Hamiltonian 2.11 used in Sec. 6.3:

$$H^{\mathrm{SF}}_{m,m'} = J\left(c^\dagger_{m\uparrow}c_{m\downarrow}c_{m'\uparrow}c^\dagger_{m'\downarrow} + c_{m\uparrow}c^\dagger_{m\downarrow}c^\dagger_{m'\uparrow}c_{m'\downarrow}\right) \qquad = JA^{\mathrm{SF}}_{m,m'} \tag{D.1}$$

$$H^{\mathrm{PH}}_{m,m'} = -J\left(c^\dagger_{m\uparrow}c^\dagger_{m\downarrow}c_{m'\uparrow}c_{m'\downarrow} + c_{m\uparrow}c_{m\downarrow}c^\dagger_{m'\uparrow}c^\dagger_{m'\downarrow}\right) \qquad = -JA^{\mathrm{PH}}_{m,m'}. \tag{D.2}$$

We note that $[H^{\mathrm{SF}}_{m,m'}, H^{\mathrm{PH}}_{m,m'}] = 0$. According to Eq. 6.9 we need the square of these operators, given by:

$$\left(A^{\mathrm{SF}}_{m,m'}\right)^2 = n_{m\uparrow}(1-n_{m\downarrow})(1-n_{m'\uparrow})n_{m'\downarrow} + (1-n_{m\uparrow})n_{m\downarrow}n_{m'\uparrow}(1-n_{m'\downarrow}) \tag{D.3}$$

$$\left(A^{\mathrm{PH}}_{m,m'}\right)^2 = n_{m\uparrow}n_{m\downarrow}(1-n_{m'\uparrow})(1-n_{m'\downarrow}) + (1-n_{m\uparrow})(1-n_{m\downarrow})n_{m'\uparrow}n_{m'\downarrow}. \tag{D.4}$$

Hence, the time evolution simplifies to (note the sign change of the sine-term due to the negative coupling $-J$ above):

$$e^{-i\Delta t H^{\mathrm{SF}}_{m,m'}} = I + (\cos(\Delta t J) - 1)\left(A^{\mathrm{SF}}_{m,m'}\right)^2 - i\sin(\Delta t J)A^{\mathrm{SF}}_{m,m'} \tag{D.5}$$

$$e^{-i\Delta t H^{\mathrm{PH}}_{m,m'}} = I + (\cos(\Delta t J) - 1)\left(A^{\mathrm{PH}}_{m,m'}\right)^2 + i\sin(\Delta t J)A^{\mathrm{PH}}_{m,m'}. \tag{D.6}$$

To construct the FTPOs we use the same conventions as in App. C. We will only show how to construct the spin-flip term. The pair hopping operator can be obtained by changing $J \to -J$ and swapping the corresponding creation annihilation operators as well as n and $(1-n)$ operators. Most importantly the structure of the FTPO tensors is the same. The FTPO we write down below, time evolves all spin-flip terms between orbital m and $m' > m$ at once. To time evolve one step, we therefore need to apply one such FTPO for each m.

The bath tensors only need to provide Fermi-operators and the identity. Therefore, they are given by:

$$\begin{aligned} W_1^{\uparrow} &= \begin{pmatrix} I \\ p \end{pmatrix}_B \qquad , \qquad W_1^{\downarrow} = \begin{pmatrix} I \end{pmatrix}_B \\ W_k^{\uparrow} &= \begin{pmatrix} I & 0 \\ 0 & p \end{pmatrix}_B \qquad , \qquad W_k^{\downarrow} = \begin{pmatrix} I \end{pmatrix}_B . \end{aligned} \tag{D.7}$$

Since for the down-spin bath the FTPO tensors are trivial we will omit the bath index for the impurity tensors with spin-down. For $m \neq 1$, the impurity tensors before m are trivial:

$$W_{n\sigma} = \Big(I(1) \Big)_I \qquad \text{for} \qquad n < m \tag{D.8}$$

The first two non-trivial tensors are located at orbital m:

$$\begin{aligned} W_{m\uparrow} &= \begin{pmatrix} \cdot \\ I(1) \\ a_1 n_{m\uparrow}(1) \\ a_1(1-n_{m\uparrow})(1) \\ a_2 c^{\dagger}_{m\uparrow} p(2) \\ a_2 c_{m\uparrow} p(2) \end{pmatrix}_I \\ W_{m\downarrow} &= \begin{pmatrix} \cdot & \cdot & \cdot & \cdot & \cdot & \cdot \\ \cdot & I & \cdot & \cdot & \cdot & \\ \cdot & \cdot & (1-n_{m\downarrow}) & \cdot & \cdot & \cdot \\ \cdot & \cdot & \cdot & n_{m\downarrow} & \cdot & \cdot \\ \cdot & \cdot & \cdot & \cdot & c^{\dagger}_{m\downarrow} & \cdot \\ \cdot & \cdot & \cdot & \cdot & \cdot & c_{m\downarrow} \end{pmatrix}_I , \end{aligned} \tag{D.9}$$

with $a_1 = (\cos(\Delta t J) - 1)$ and $a_2 = -i\sin(\Delta t J)$. For the next orbital we find (omitting orbital and spin indices of the operators from now on):

$$
\begin{aligned}
W_{(m+1)\uparrow} &= \begin{pmatrix}
I(1) & . & . & . & . & . \\
. & I(1) & . & . & . & \\
. & . & (1-n)(1) & . & . & . \\
. & . & . & n(1) & . & . \\
. & . & . & . & cp(2) & . \\
. & . & . & . & . & c^{\dagger}p(2) \\
. & . & I(1) & . & . & . \\
. & . & . & I(1) & . & . \\
. & . & . & . & I(1) & . \\
. & . & . & . & . & I(1)
\end{pmatrix}_{I} \\
W_{(m+1)\downarrow} &= \begin{pmatrix}
I & . & n & (1-n) & c^{\dagger} & c & . & . & . & . \\
. & I & . & . & . & . & . & . & . & . \\
. & . & . & . & . & . & I & . & . & . \\
. & . & . & . & . & . & . & I & . & . \\
. & . & . & . & . & . & . & . & I & . \\
. & . & . & . & . & . & . & . & . & I
\end{pmatrix}_{I}
\end{aligned}
\tag{D.10}
$$

We repeat the two tensors in Eq. D.10 for all orbitals $m' \neq N_{\text{orb}}$. Those for the last orbital finally are given by:

$$
\begin{aligned}
W_{N_{\text{orb}}\uparrow} &= \begin{pmatrix}
I(1) & . & . & . & . & . \\
. & I(1) & . & . & . & \\
. & . & (1-n)(1) & . & . & . \\
. & . & . & n(1) & . & . \\
. & . & . & . & cp(2) & . \\
. & . & . & . & . & c^{\dagger}p(2)
\end{pmatrix}_{I} \\
W_{N_{\text{orb}}\downarrow} &= \begin{pmatrix}
I & I & n & (1-n) & c^{\dagger} & c
\end{pmatrix}_{I}.
\end{aligned}
\tag{D.11}
$$

References

[1] D. Bauernfeind, M. Zingl, R. Triebl, M. Aichhorn, and H. G. Evertz. Fork Tensor-Product States: Efficient Multiorbital Real-Time DMFT Solver. *Phys. Rev. X* 7, 031013 (2017) (see pp. 4, 40, 68, 70, 106, 111, 112, 114).

[2] V. Eisler and D. Bauernfeind. Front dynamics and entanglement in the XXZ chain with a gradient. *Phys. Rev. B* 96, 174301 (2017) (see p.).

[3] M. Zingl, M. Nuss, D. Bauernfeind, and M. Aichhorn. A real-frequency solver for the Anderson impurity model based on bath optimization and cluster perturbation theory. *Physica B: Condensed Matter.* (2017) (see pp. 48, 52).

[4] D. Bauernfeind, R. Triebl, M. Zingl, M. Aichhorn, and H. G. Evertz. Dynamical Mean-Field Theory on the Real-Frequency Axis: p-d Hybridizations and Atomic Physics in SrMnO$_3$. *ArXiv e-prints.* Submitted to PRB. arXiv:1712.08055 (2017) (see pp. 4, 103).

[5] *Interaction* `https://dictionary.cambridge.org/dictionary/english/interaction`. Accessed: 2018-01-22 (see p. 2).

[6] J. R. Schrieffer and P. A. Wolff. Relation between the Anderson and Kondo Hamiltonians. *Phys. Rev.* 149, 491 (1966) (see pp. 2, 5).

[7] A. C. Hewson. *The Kondo Problem to Heavy Fermions* (Cambridge University Press, 1993) (see pp. 2, 5, 6, 8).

[8] J. Kondo. Resistance Minimum in Dilute Magnetic Alloys. *Progress of Theoretical Physics* 32, 37 (1964) (see pp. 2, 5, 8).

[9] W. Metzner and D. Vollhardt. Correlated Lattice Fermions in $d = \infty$ Dimensions. *Phys. Rev. Lett.* 62, 324 (1989) (see pp. 2, 16, 71, 108).

[10] A. Georges and G. Kotliar. Hubbard model in infinite dimensions. *Phys. Rev. B* 45, 6479 (1992) (see pp. 2, 16).

[11] A. Georges. Strongly Correlated Electron Materials: Dynamical Mean-Field Theory and Electronic Structure. In: *American Institute of Physics Conference Series* (eds A. Avella and F. Mancini) 715 (2004), 3 (see pp. 2, 16, 17, 19, 83).

[12] V. I. Anisimov, A. I. Poteryaev, M. A. Korotin, A. O. Anokhin, and G. Kotliar. First-principles calculations of the electronic structure and spectra of strongly correlated systems: dynamical mean-field theory. *Journal of Physics: Condensed Matter* 9, 7359 (1997) (see pp. 2, 19, 105).

[13] G. Kotliar, S. Y. Savrasov, K. Haule, V. S. Oudovenko, O. Parcollet, and C. A. Marianetti. Electronic structure calculations with dynamical mean-field theory. *Rev. Mod. Phys.* 78, 865 (2006) (see pp. 2, 16, 19, 83, 105, 108).

[14] E. Gull, A. J. Millis, A. I. Lichtenstein, A. N. Rubtsov, M. Troyer, and P. Werner. Continuous-time Monte Carlo methods for quantum impurity models. *Rev. Mod. Phys.* 83, 349 (2011) (see pp. 3, 14, 71, 105).

[15] P. Werner, A. Comanac, L. de'Medici, M. Troyer, and A. J. Millis. Continuous-Time Solver for Quantum Impurity Models. *Phys. Rev. Lett.* 97, 076405 (2006) (see pp. 3, 14, 71, 105).

[16] S. R. White. Density matrix formulation for quantum renormalization groups. *Phys. Rev. Lett.* 69, 2863 (1992) (see pp. 3, 21, 72, 76, 111).

[17] U. Schollwöck. The density-matrix renormalization group in the age of matrix product states. *Ann. Phys.* 326, 96 (2011) (see pp. 3, 14, 21, 27, 30, 32, 33, 40, 45, 64, 66, 72, 75, 76, 82, 111, 132, 136).

[18] P. W. Anderson. Localized Magnetic States in Metals. *Phys. Rev.* 124, 41 (1961) (see p. 5).

[19] K. G. Wilson. The renormalization group: Critical phenomena and the Kondo problem. *Rev. Mod. Phys.* 47, 773 (1975) (see pp. 7, 8, 13, 71).

[20] R. Bulla, T. A. Costi, and T. Pruschke. Numerical renormalization group method for quantum impurity systems. *Rev. Mod. Phys.* 80, 395 (2008) (see pp. 7, 8, 13, 71, 77, 84).

[21] J. Kanamori. Electron Correlation and Ferromagnetism of Transition Metals. *Progress of Theoretical Physics* 30, 275 (1963) (see pp. 10, 108).

[22] M. W. Haverkort. Spin and orbital degrees of freedom in transition metal oxides and oxide thin films studied by soft x-ray absorption spectroscopy. *arXiv preprint cond-mat/0505214*. PhD Thesis (2005) (see p. 10).

[23] A. Georges, L. de'Medici, and J. Mravlje. Strong Correlations from Hund's Coupling. *Annu. Rev. Condens. Matter Phys.* 4, 137 (2013) (see pp. 10, 74, 95, 114, 117).

[24] M. Ganahl, M. Aichhorn, H. G. Evertz, P. Thunström, K. Held, and F. Verstraete. Efficient DMFT impurity solver using real-time dynamics with matrix product states. *Phys. Rev. B* 92, 155132 (2015) (see pp. 12, 14, 15, 38, 51, 54, 73, 77, 85, 96, 99, 101).

[25] M. Caffarel and W. Krauth. Exact diagonalization approach to correlated fermions in infinite dimensions: Mott transition and superconductivity. *Phys. Rev. Lett.* 72, 1545 (1994) (see pp. 13, 71).

[26] M. Capone, L. de'Medici, and A. Georges. Solving the dynamical mean-field theory at very low temperatures using the Lanczos exact diagonalization. *Phys. Rev. B* 76, 245116 (2007) (see pp. 13, 71).

[27] J. Kolorenč, A. B. Shick, and A. I. Lichtenstein. Electronic structure and core-level spectra of light actinide dioxides in the dynamical mean-field theory. *Phys. Rev. B* 92, 085125 (2015) (see pp. 13, 71).

[28] Y. Lu, M. Höppner, O. Gunnarsson, and M. W. Haverkort. Efficient real-frequency solver for dynamical mean-field theory. *Phys. Rev. B* 90, 085102 (2014) (see pp. 13, 71, 72).

[29] D. Zgid, E. Gull, and G. K. L. Chan. Truncated configuration interaction expansions as solvers for correlated quantum impurity models and dynamical mean-field theory. *Phys. Rev. B* 86, 165128 (2012) (see pp. 13, 71, 72).

[30] C. Mejuto Zaera, N. M. Tubman, and K. B. Whaley. Next Generation Dynamical Mean-Field Theory Simulations with the Adaptive Sampling Configuration Interaction Method. *ArXiv e-prints.* arXiv:1711.04771 (2017) (see p. 13).

[31] A. Go and A. J. Millis. Adaptively truncated Hilbert space based impurity solver for dynamical mean-field theory. *Phys. Rev. B* 96, 085139 (2017) (see p. 13).

[32] K. M. Stadler, Z. P. Yin, J. von Delft, G. Kotliar, and A. Weichselbaum. Dynamical Mean-Field Theory Plus Numerical Renormalization-Group Study of Spin-Orbital Separation in a Three-Band Hund Metal. *Phys. Rev. Lett.* 115, 136401 (2015) (see pp. 14, 72, 74).

[33] A. Horvat, R. Žitko, and J. Mravlje. Low-energy physics of three-orbital impurity model with Kanamori interaction. *Phys. Rev. B* 94, 165140 (2016) (see pp. 14, 72).

[34] K. M. Stadler, A. K. Mitchell, J. von Delft, and A. Weichselbaum. Interleaved numerical renormalization group as an efficient multiband impurity solver. *Phys. Rev. B* 93, 235101 (2016) (see pp. 14, 72).

[35] S.-S. B. Lee, J. von Delft, and A. Weichselbaum. Filling-driven Mott transition in SU(N) Hubbard models. *ArXiv e-prints.* arXiv:1710.04057 (2017) (see pp. 14, 54).

[36] A. Weichselbaum, F. Verstraete, U. Schollwöck, J. I. Cirac, and J. von Delft. Variational matrix-product-state approach to quantum impurity models. *Phys. Rev. B* 80, 165117 (2009) (see p. 14).

[37] J. E. Hirsch and R. M. Fye. Monte Carlo Method for Magnetic Impurities in Metals. *Phys. Rev. Lett.* 56, 2521 (1986) (see p. 14).

[38] X. Deng, K. Haule, and G. Kotliar. Plutonium Hexaboride is a Correlated Topological Insulator. *Phys. Rev. Lett.* 111, 176404 (2013) (see p. 14).

[39] C. A. Marianetti, K. Haule, G. Kotliar, and M. J. Fluss. Electronic Coherence in δ-Pu: A Dynamical Mean-Field Theory Study. *Phys. Rev. Lett.* 101, 056403 (2008) (see p. 14).

[40] Q. Dong, I. Krivenko, J. Kleinhenz, A. E. Antipov, G. Cohen, and E. Gull. Quantum Monte Carlo solution of the dynamical mean field equations in real time. *ArXiv e-prints.* arXiv:1706.02975 (2017) (see p. 14).

[41] D. J. García, K. Hallberg, and M. J. Rozenberg. Dynamical Mean Field Theory with the Density Matrix Renormalization Group. *Phys. Rev. Lett.* 93, 246403 (2004) (see pp. 14, 72).

[42] S. Nishimoto and E. Jeckelmann. Density-matrix renormalization group approach to quantum impurity problems. *Journal of Physics: Condensed Matter* 16, 613 (2004) (see pp. 14, 72).

[43] R. Peters. Spectral functions for single- and multi-impurity models using density matrix renormalization group. *Phys. Rev. B* 84, 075139 (2011) (see pp. 14, 72).

[44] M. Karski, C. Raas, and G. S. Uhrig. Single-particle dynamics in the vicinity of the Mott-Hubbard metal-to-insulator transition. *Phys. Rev. B* 77, 075116 (2008) (see pp. 14, 72).

[45] M. Karski, C. Raas, and G. S. Uhrig. Electron spectra close to a metal-to-insulator transition. *Phys. Rev. B* 72, 113110 (2005) (see pp. 14, 72).

[46] M. Ganahl, P. Thunström, F. Verstraete, K. Held, and H. G. Evertz. Chebyshev expansion for impurity models using matrix product states. *Phys. Rev. B* 90, 045144 (2014) (see pp. 14, 72, 77, 99).

[47] F. A. Wolf, A. Go, I. P. McCulloch, A. J. Millis, and U. Schollwöck. Imaginary-Time Matrix Product State Impurity Solver for Dynamical Mean-Field Theory. *Phys. Rev. X* 5, 041032 (2015) (see pp. 14, 15, 54, 73).

[48] F. A. Wolf, I. P. McCulloch, O. Parcollet, and U. Schollwöck. Chebyshev matrix product state impurity solver for dynamical mean-field theory. *Phys. Rev. B* 90, 115124 (2014) (see pp. 14, 72, 77).

[49] F. A. Wolf, I. P. McCulloch, and U. Schollwöck. Solving nonequilibrium dynamical mean-field theory using matrix product states. *Phys. Rev. B* 90, 235131 (2014) (see pp. 14, 39, 40, 44, 79, 84).

[50] A. Holzner, A. Weichselbaum, and J. von Delft. Matrix product state approach for a two-lead multilevel Anderson impurity model. *Phys. Rev. B* 81, 125126 (2010) (see pp. 14, 57, 73, 80).

[51] W. Zhu, D. N. Sheng, and J.-X. Zhu. Magnetic field dependent dynamics and field-driven metal-to-insulator transition of the half-filled Hubbard model: A DMFT+DMRG study. *Phys. Rev. B* 96, 085118 (2017) (see p. 14).

[52] T. Shirakawa and S. Yunoki. Density matrix renormalization group study in energy space for a single-impurity Anderson model and an impurity quantum phase transition. *Phys. Rev. B* 93, 205124 (2016) (see p. 14).

[53] K. Hallberg and Y. N. Fernández. An efficient impurity-solver for the dynamical mean field theory algorithm. *Papers in Physics* 9. (2017) (see p. 14).

[54] T. Shirakawa and S. Yunoki. Block Lanczos density-matrix renormalization group method for general Anderson impurity models: Application to magnetic impurity problems in graphene. *Phys. Rev. B* 90, 195109 (2014) (see p. 14).

[55] D. J. García, E. Miranda, K. Hallberg, and M. J. Rozenberg. Mott transition in the Hubbard model away from particle-hole symmetry. *Phys. Rev. B* 75, 121102 (2007) (see p. 14).

[56] P. E. Dargel, A. Honecker, R. Peters, R. M. Noack, and T. Pruschke. Adaptive Lanczos-vector method for dynamic properties within the density matrix renormalization group. *Phys. Rev. B* 83, 161104 (2011) (see p. 14).

[57] S. Nishimoto, F. Gebhard, and E. Jeckelmann. Dynamical density-matrix renormalization group for the Mott–Hubbard insulator in high dimensions. *Journal of Physics: Condensed Matter* 16, 7063 (2004) (see p. 14).

[58] C. Raas, G. S. Uhrig, and F. B. Anders. High-energy dynamics of the single-impurity Anderson model. *Phys. Rev. B* 69, 041102 (2004) (see p. 14).

[59] S. Nishimoto, T. Pruschke, and R. M. Noack. Spectral density of the two-impurity Anderson model. *Journal of Physics: Condensed Matter* 18, 981 (2006) (see p. 14).

[60] C. Guo, A. Weichselbaum, S. Kehrein, T. Xiang, and J. von Delft. Density matrix renormalization group study of a quantum impurity model with Landau-Zener time-dependent Hamiltonian. *Phys. Rev. B* 79, 115137 (2009) (see p. 14).

[61] A. Weichselbaum, F. Verstraete, U. Schollwöck, J. I. Cirac, and J. von Delft. Variational matrix-product-state approach to quantum impurity models. *Phys. Rev. B* 80, 165117 (2009) (see p. 14).

[62] S.-S. B. Lee, J. von Delft, and A. Weichselbaum. Doublon-Holon Origin of the Subpeaks at the Hubbard Band Edges. *Phys. Rev. Lett.* 119, 236402 (2017) (see p. 15).

[63] A. Georges, G. Kotliar, W. Krauth, and M. J. Rozenberg. Dynamical mean-field theory of strongly correlated fermion systems and the limit of infinite dimensions. *Rev. Mod. Phys.* 68, 13 (1996) (see pp. 16, 71, 83, 108).

[64] W. Kohn. Nobel Lecture: Electronic structure of matter-wave functions and density functionals. *Rev. Mod. Phys.* 71, 1253 (1999) (see p. 19).

[65] R. O. Jones and O. Gunnarsson. The density functional formalism, its applications and prospects. *Rev. Mod. Phys.* 61, 689 (1989) (see p. 19).

[66] W. Kohn and L. J. Sham. Self-Consistent Equations Including Exchange and Correlation Effects. *Phys. Rev.* 140, A1133 (1965) (see p. 19).

[67] V. I. Anisimov, D. E. Kondakov, A. V. Kozhevnikov, I. A. Nekrasov, Z. V. Pchelkina, J. W. Allen, S.-K. Mo, H.-D. Kim, P. Metcalf, S. Suga, A. Sekiyama, G. Keller, I. Leonov, X. Ren, and D. Vollhardt. Full orbital calculation scheme for materials with strongly correlated electrons. *Phys. Rev. B* 71, 125119 (2005) (see pp. 19, 105, 107).

[68] M. Aichhorn, L. Pourovskii, V. Vildosola, M. Ferrero, O. Parcollet, T. Miyake, A. Georges, and S. Biermann. Dynamical mean-field theory within an augmented plane-wave framework: Assessing electronic correlations in the iron pnictide LaFeAsO. *Phys. Rev. B* 80, 085101 (2009) (see pp. 19, 86, 105, 107, 111).

[69] F. Aryasetiawan, M. Imada, A. Georges, G. Kotliar, S. Biermann, and A. I. Lichtenstein. Frequency-dependent local interactions and low-energy effective models from electronic structure calculations. *Phys. Rev. B* 70, 195104 (2004) (see p. 19).

[70] B.-C. Shih, Y. Zhang, W. Zhang, and P. Zhang. Screened Coulomb interaction of localized electrons in solids from first principles. *Phys. Rev. B* 85, 045132 (2012) (see p. 19).

[71] R. Sakuma and F. Aryasetiawan. First-principles calculations of dynamical screened interactions for the transition metal oxides MO (M=Mn, Fe, Co, Ni). *Phys. Rev. B* 87, 165118 (2013) (see p. 19).

[72] B. Amadon, T. Applencourt, and F. Bruneval. Screened Coulomb interaction calculations: cRPA implementation and applications to dynamical screening and self-consistency in uranium dioxide and cerium. *Phys. Rev. B* 89, 125110 (2014) (see p. 19).

[73] O. Gunnarsson, O. K. Andersen, O. Jepsen, and J. Zaanen. Density-functional calculation of the parameters in the Anderson model: Application to Mn in CdTe. *Phys. Rev. B* 39, 1708 (1989) (see p. 19).

[74] K. Haule. Exact Double Counting in Combining the Dynamical Mean Field Theory and the Density Functional Theory. *Phys. Rev. Lett.* 115, 196403 (2015) (see pp. 20, 110, 123).

[75] H. Park, A. J. Millis, and C. A. Marianetti. Total energy calculations using DFT+DMFT: Computing the pressure phase diagram of the rare earth nickelates. *Phys. Rev. B* 89, 245133 (2014) (see pp. 20, 110, 123).

[76] M. Karolak, G. Ulm, T. Wehling, V. Mazurenko, A. Poteryaev, and A. Lichtenstein. Double counting in LDA+DMFT—The example of NiO. *Journal of Electron Spectroscopy and Related Phenomena* 181, 11 (2010) (see pp. 20, 110, 111).

[77] K. Haule, C.-H. Yee, and K. Kim. Dynamical mean-field theory within the full-potential methods: Electronic structure of $\mathrm{CeIrIn_5}$, $\mathrm{CeCoIn_5}$, and $\mathrm{CeRhIn_5}$. *Phys. Rev. B* 81, 195107 (2010) (see pp. 20, 110).

[78] K. Held. Electronic structure calculations using dynamical mean field theory. *Adv. Phys.* 56, 829 (2007) (see pp. 20, 110).

[79] S. Östlund and S. Rommer. Thermodynamic Limit of Density Matrix Renormalization. *Phys. Rev. Lett.* 75, 3537 (1995) (see p. 21).

[80] J. Dukelsky, M. A. Martin-Delgado, T. Nishino, and G. Sierra. Equivalence of the variational matrix product method and the density matrix renormalization group applied to spin chains. *EPL (Europhysics Letters)* 43, 457 (1998) (see p. 21).

[81] F. Verstraete, V. Murg, and J. Cirac. Matrix product states, projected entangled pair states, and variational renormalization group methods for quantum spin systems. *Advances in Physics* 57, 143 (2008) (see p. 21).

[82] C. Eckart and G. Young. The approximation of one matrix by another of lower rank. *Psychometrika* 1, 211 (1936) (see p. 22).

[83] J. Haegeman, C. Lubich, I. Oseledets, B. Vandereycken, and F. Verstraete. Unifying time evolution and optimization with matrix product states. *Phys. Rev. B* 94, 165116 (2016) (see pp. 24, 80).

[84] J. Eisert, M. Cramer, and M. B. Plenio. Colloquium. *Rev. Mod. Phys.* 82, 277 (2010) (see p. 28).

[85] G. M. Crosswhite and D. Bacon. Finite automata for caching in matrix product algorithms. *Phys. Rev. A* 78, 012356 (2008) (see pp. 30, 41).

[86] M. P. Zaletel, R. S. K. Mong, C. Karrasch, J. E. Moore, and F. Pollmann. Time-evolving a matrix product state with long-ranged interactions. *Phys. Rev. B* 91, 165112 (2015) (see pp. 30, 80).

[87] A. Dorda, M. Nuss, W. von der Linden, and E. Arrigoni. Auxiliary master equation approach to nonequilibrium correlated impurities. *Phys. Rev. B* 89, 165105 (2014) (see p. 33).

[88] A. Dorda, M. Ganahl, H. G. Evertz, W. von der Linden, and E. Arrigoni. Auxiliary master equation approach within matrix product states: Spectral properties of the nonequilibrium Anderson impurity model. *Phys. Rev. B* 92, 125145 (2015) (see p. 33).

[89] S. R. White and A. E. Feiguin. Real-Time Evolution Using the Density Matrix Renormalization Group. *Phys. Rev. Lett.* 93, 076401 (2004) (see pp. 33, 72).

[90] E. M. Stoudenmire and S. R. White. Minimally entangled typical thermal state algorithms. *New J. Phys.* 12, 055026 (2010) (see pp. 34, 45, 82, 85).

[91] M. Suzuki. Fractal decomposition of exponential operators with applications to many-body theories and Monte Carlo simulations. *Physics Letters A* 146, 319 (1990) (see pp. 34, 80).

[92] D. Kennes and C. Karrasch. Extending the range of real time density matrix renormalization group simulations. *Computer Physics Communications* 200, 37 (2016) (see p. 37).

[93] I. P. McCulloch. From density-matrix renormalization group to matrix product states. *Journal of Statistical Mechanics: Theory and Experiment* 2007, P10014 (2007) (see p. 40).

[94] S. Paeckel, T. Köhler, and S. R. Manmana. Automated construction of $U(1)$-invariant matrix-product operators from graph representations. *SciPost Phys.* 3, 035 (2017) (see p. 41).

[95] P. Jordan and E. Wigner. Über das Paulische Äquivalenzverbot. *Zeitschrift für Physik* 47, 631 (1928) (see p. 42).

[96] R. Orús. Advances on tensor network theory: symmetries, fermions, entanglement, and holography. *The European Physical Journal B* 87, 280 (2014) (see p. 45).

[97] F. Verstraete, J. I. Cirac, and J. I. Latorre. Quantum circuits for strongly correlated quantum systems. *Phys. Rev. A* 79, 032316 (2009) (see p. 45).

[98] S. R. White and I. Affleck. Spectral function for the S=1 Heisenberg antiferromagetic chain. *Phys. Rev. B* 77, 134437 (2008) (see pp. 52, 72, 85, 101, 111, 112).

[99] E. Stoudenmire and S. R. White. Studying Two-Dimensional Systems with the Density Matrix Renormalization Group. *Annual Review of Condensed Matter Physics* 3, 111 (2012) (see p. 51).

[100] A. Weichselbaum. Non-abelian symmetries in tensor networks: A quantum symmetry space approach. *Annals of Physics* 327, 2972 (2012) (see p. 54).

[101] H. Guo and S. R. White. Density matrix renormalization group algorithms for Y-junctions. *Phys. Rev. B* 74, 060401 (2006) (see pp. 57, 80).

[102] Y. Y. Shi, L. M. Duan, and G. Vidal. Classical simulation of quantum many-body systems with a tree tensor network. *Phys. Rev. A* 74, 022320 (2006) (see pp. 57, 80).

[103] L. Tagliacozzo, G. Evenbly, and G. Vidal. Simulation of two-dimensional quantum systems using a tree tensor network that exploits the entropic area law. *Phys. Rev. B* 80, 235127 (2009) (see pp. 57, 80).

[104] V. Murg, F. Verstraete, Ö. Legeza, and R. M. Noack. Simulating strongly correlated quantum systems with tree tensor networks. *Phys. Rev. B* 82, 205105 (2010) (see pp. 57, 77, 80).

[105] I. Pižorn, F. Verstraete, and R. M. Konik. Tree tensor networks and entanglement spectra. *Phys. Rev. B* 88, 195102 (2013) (see pp. 57, 80).

[106] O. Parcollet, M. Ferrero, T. Ayral, H. Hafermann, I. Krivenko, L. Messio, and P. Seth. TRIQS: A toolbox for research on interacting quantum systems. *Comput. Phys. Commun.* 196, 398 (2015) (see pp. 70, 86, 103, 111).

[107] P. W. Anderson. More Is Different. *Science* 177, 393 (1972) (see p. 71).

[108] K. A. Hallberg. Density-matrix algorithm for the calculation of dynamical properties of low-dimensional systems. *Phys. Rev. B* 52, R9827 (1995) (see p. 72).

[109] T. D. Kühner and S. R. White. Dynamical correlation functions using the density matrix renormalization group. *Phys. Rev. B* 60, 335 (1999) (see p. 72).

[110] E. Jeckelmann. Dynamical density-matrix renormalization-group method. *Phys. Rev. B* 66, 045114 (2002) (see p. 72).

[111] A. Weiße, G. Wellein, A. Alvermann, and H. Fehske. The kernel polynomial method. *Rev. Mod. Phys.* 78, 275 (2006) (see p. 72).

[112] A. Holzner, A. Weichselbaum, I. P. McCulloch, U. Schollwöck, and J. von Delft. Chebyshev matrix product state approach for spectral functions. *Phys. Rev. B* 83, 195115 (2011) (see p. 72).

[113] G. Vidal. Efficient Classical Simulation of Slightly Entangled Quantum Computations. *Phys. Rev. Lett.* 91, 147902 (2003) (see p. 72).

[114] G. Vidal. Efficient Simulation of One-Dimensional Quantum Many-Body Systems. *Phys. Rev. Lett.* 93, 040502 (2004) (see p. 72).

[115] A. J. Daley, C. Kollath, U. Schollwöck, and G. Vidal. Time-dependent density-matrix renormalization-group using adaptive effective Hilbert spaces. *Journal of Statistical Mechanics: Theory and Experiment* 2004, P04005 (2004) (see p. 72).

[116] P. Werner, E. Gull, M. Troyer, and A. J. Millis. Spin Freezing Transition and Non-Fermi-Liquid Self-Energy in a Three-Orbital Model. *Phys. Rev. Lett.* 101, 166405 (2008) (see p. 74).

[117] L. de'Medici, J. Mravlje, and A. Georges. Janus-Faced Influence of Hund's Rule Coupling in Strongly Correlated Materials. *Phys. Rev. Lett.* 107, 256401 (2011) (see p. 74).

[118] A. J. Kim, H. O. Jeschke, P. Werner, and R. Valentí. **J**-Freezing and Hund's Rules in Spin-Orbit-Coupled Multiorbital Hubbard Models. *Phys. Rev. Lett.* 118, 086401 (2017) (see p. 74).

[119] F. Verstraete and J. I. Cirac. Matrix product states represent ground states faithfully. *Phys. Rev. B* 73, 094423 (2006) (see p. 75).

[120] P. Schmitteckert. Nonequilibrium electron transport using the density matrix renormalization group method. *Phys. Rev. B* 70, 121302 (2004) (see p. 80).

[121] J. Haegeman, J. I. Cirac, T. J. Osborne, I. Pižorn, H. Verschelde, and F. Verstraete. Time-Dependent Variational Principle for Quantum Lattices. *Phys. Rev. Lett.* 107, 070601 (2011) (see p. 80).

[122] F. Lechermann, A. Georges, A. Poteryaev, S. Biermann, M. Posternak, A. Yamasaki, and O. K. Andersen. Dynamical mean-field theory using Wannier functions: A flexible route to electronic structure calculations of strongly correlated materials. *Phys. Rev. B* 74, 125120 (2006) (see pp. 83, 105, 108).

[123] E. Koch, G. Sangiovanni, and O. Gunnarsson. Sum rules and bath parametrization for quantum cluster theories. *Phys. Rev. B* 78, 115102 (2008) (see p. 84).

[124] I. de Vega, U. Schollwöck, and F. A. Wolf. How to discretize a quantum bath for real-time evolution. *Phys. Rev. B* 92, 155126 (2015) (see p. 84).

[125] J. G. Liu, D. Wang, and Q. H. Wang. Quantum impurities in channel mixing baths. *Phys. Rev. B* 93, 035102 (2016) (see p. 84).

[126] T. Barthel. Precise evaluation of thermal response functions by optimized density matrix renormalization group schemes. *New J. Phys.* 15, 073010 (2013) (see p. 85).

[127] P. Blaha, K. Schwarz, G. Madsen, D. Kvasnicka, and J. Luitz. *WIEN2k, An augmented Plane Wave + Local Orbitals Program for Calculating Crystal Properties* (Techn. Universität Wien, Austria, 2001) (see pp. 86, 107).

[128] M. Aichhorn, L. Pourovskii, P. Seth, V. Vildosola, M. Zingl, O. E. Peil, X. Deng, J. Mravlje, G. J. Kraberger, C. Martins, M. Ferrero, and O. Parcollet. TRIQS/DFTTools: A {TRIQS} application for ab initio calculations of correlated materials. *Comput. Phys. Commun.* 204, 200 (2016) (see pp. 86, 111).

[129] M. Aichhorn, L. Pourovskii, and A. Georges. Importance of electronic correlations for structural and magnetic properties of the iron pnictide superconductor LaFeAsO. *Phys. Rev. B* 84, 054529 (2011) (see pp. 86, 111).

[130] A. Liebsch. Surface versus Bulk Coulomb Correlations in Photoemission Spectra of $SrVO_3$ and $CaVO_3$. *Phys. Rev. Lett.* 90, 096401 (2003) (see p. 86).

[131] A. Sekiyama, H. Fujiwara, S. Imada, S. Suga, H. Eisaki, S. I. Uchida, K. Takegahara, H. Harima, Y. Saitoh, I. A. Nekrasov, G. Keller, D. E. Kondakov, A. V. Kozhevnikov, T. Pruschke, K. Held, D. Vollhardt, and V. I. Anisimov. Mutual Experimental and Theoretical Validation of Bulk Photoemission Spectra of $Sr_{1-x}Ca_xVO_3$. *Phys. Rev. Lett.* 93, 156402 (2004) (see p. 86).

[132] G. Sangiovanni, A. Toschi, E. Koch, K. Held, M. Capone, C. Castellani, O. Gunnarsson, S.-K. Mo, J. W. Allen, H.-D. Kim, A. Sekiyama, A. Yamasaki, S. Suga, and P. Metcalf. Static versus dynamical mean-field theory of Mott antiferromagnets. *Phys. Rev. B* 73, 205121 (2006) (see p. 88).

[133] E. Gull, D. R. Reichman, and A. J. Millis. Bold-line diagrammatic Monte Carlo method: General formulation and application to expansion around the noncrossing approximation. *Phys. Rev. B* 82, 075109 (2010) (see p. 88).

[134] P. Seth, I. Krivenko, M. Ferrero, and O. Parcollet. TRIQS/CTHYB: A continuous-time quantum Monte Carlo hybridisation expansion solver for quantum impurity problems. *Comput. Phys. Commun.* 200, 274 (2016) (see pp. 89, 111).

[135] P. Werner and A. J. Millis. Hybridization expansion impurity solver: General formulation and application to Kondo lattice and two-orbital models. *Phys. Rev. B* 74, 155107 (2006) (see pp. 89, 105, 111).

[136] D. Bergeron and A.-M. S. Tremblay. Algorithms for optimized maximum entropy and diagnostic tools for analytic continuation. *Phys. Rev. E* 94, 023303 (2016) (see pp. 89, 111).

[137] L. Vaugier, H. Jiang, and S. Biermann. Hubbard U and Hund exchange J in transition metal oxides: Screening versus localization

trends from constrained random phase approximation. *Phys. Rev. B* 86, 165105 (2012) (see p. 94).

[138] K. Lee and E. Iguchi. Electronic Properties of SrMnO3-x. *J. Solid State Chem* 114, 242 (1995) (see p. 105).

[139] M. Abbate, F. M. F. de Groot, J. C. Fuggle, A. Fujimori, O. Strebel, F. Lopez, M. Domke, G. Kaindl, G. A. Sawatzky, M. Takano, Y. Takeda, H. Eisaki, and S. Uchida. Controlled-valence properties of $La_{1-x}Sr_xFeO_3$ and $La_{1-x}Sr_xMnO_3$ studied by soft-x-ray absorption spectroscopy. *Phys. Rev. B* 46, 4511 (1992) (see pp. 105, 119, 127).

[140] A. Chainani, M. Mathew, and D. D. Sarma. Electron spectroscopic investigation of the semiconductor-metal transition in $La_{1-x}Sr_xMnO_3$. *Phys. Rev. B* 47, 15397 (1993) (see pp. 105, 119, 127).

[141] J.-S. Kang, H. J. Lee, G. Kim, D. H. Kim, B. Dabrowski, S. Kolesnik, H. Lee, J.-Y. Kim, and B. I. Min. Electronic structure of the cubic perovskite $SrMn_{1-x}Fe_xO_3$ investigated by x-ray spectroscopies. *Phys. Rev. B* 78, 054434 (2008) (see pp. 105, 127).

[142] T. Saitoh, A. E. Bocquet, T. Mizokawa, H. Namatame, A. Fujimori, M. Abbate, Y. Takeda, and M. Takano. Electronic structure of $La_{1-x}Sr_xMnO_3$ studied by photoemission and x-ray-absorption spectroscopy. *Phys. Rev. B* 51, 13942 (1995) (see pp. 105, 119, 127).

[143] D. H. Kim, H. J. Lee, B. Dabrowski, S. Kolesnik, J. Lee, B. Kim, B. I. Min, and J.-S. Kang. Photoemission spectroscopy study of metal-insulator transition in $SrMn_{1-x}Fe_xO_3$. *Phys. Rev. B* 81, 073101 (2010) (see pp. 105, 106, 126, 127).

[144] H. T. Dang, X. Ai, A. J. Millis, and C. A. Marianetti. Density functional plus dynamical mean-field theory of the metal-insulator transition in early transition-metal oxides. *Phys. Rev. B* 90, 125114 (2014) (see pp. 105, 108, 119, 123, 127, 128).

[145] H. Chen, H. Park, A. J. Millis, and C. A. Marianetti. Charge transfer across transition-metal oxide interfaces: Emergent conductance and electronic structure. *Phys. Rev. B* 90, 245138 (2014) (see pp. 105, 108, 128).

[146] R. Søndenå, P. Ravindran, S. Stølen, T. Grande, and M. Hanfland. Electronic structure and magnetic properties of cubic and hexagonal $SrMnO_3$. *Phys. Rev. B* 74, 144102 (2006) (see p. 105).

[147] J. Mravlje, M. Aichhorn, and A. Georges. Origin of the High Néel Temperature in $SrTcO_3$. *Phys. Rev. Lett.* 108, 197202 (2012) (see pp. 105, 108).

[148] J. Zaanen, G. A. Sawatzky, and J. W. Allen. Band gaps and electronic structure of transition-metal compounds. *Phys. Rev. Lett.* 55, 418 (1985) (see p. 115).

[149] J. Kang. private communication. (4, 2017) (see p. 127).

[150] *ITensor library* `http://itensor.org/` (see p. 129).